The Astrophysical Journal, 736:59 (30pp), 2011 July 20

doi:10.1088/0004-637X/736/1/59

© 2011. The American Astronomical Society. All rights reserved. Printed in the U.S.A.

GALAXY CLUSTERING IN THE COMPLETED SDSS REDSHIFT SURVEY: THE DEPENDENCE ON COLOR AND LUMINOSITY

Idit Zehavi[1], Zheng Zheng[2], David H. Weinberg[3], Michael R. Blanton[4], Neta A. Bahcall[5], Andreas A. Berlind[6], Jon Brinkmann[7], Joshua A. Frieman[8,9], James E. Gunn[5], Robert H. Lupton[5], Robert C. Nichol[10], Will J. Percival[10], Donald P. Schneider[11], Ramin A. Skibba[12], Michael A. Strauss[5], Max Tegmark[13], and Donald G. York[9,14]

[1] Department of Astronomy and CERCA, Case Western Reserve University, 10900 Euclid Avenue, Cleveland, OH 44106, USA
[2] Yale Center for Astronomy and Astrophysics, Yale University, New Haven, CT 06520, USA
[3] Department of Astronomy and CCAPP, Ohio State University, Columbus, OH 43210, USA
[4] Center for Cosmology and Particle Physics, Department of Physics, New York University, New York, NY 10003, USA
[5] Department of Astrophysical Sciences, Princeton University, Peyton Hall, Princeton, NJ 08540, USA
[6] Department of Physics and Astronomy, Vanderbilt University, Nashville, TN 37235, USA
[7] Apache Point Observatory, P.O. Box 59, Sunspot, NM 88349, USA
[8] Fermi National Accelerator Laboratory, P.O. Box 500, Batavia, IL 60510, USA
[9] Department of Astronomy and Astrophysics, The University of Chicago, 5640 S. Ellis Avenue, Chicago, IL 60615, USA
[10] Institute of Cosmology and Gravitation, University of Portsmouth, Portsmouth P01 2EG, UK
[11] Department of Astronomy and Astrophysics, The Pennsylvania State University, University Park, PA 16802, USA
[12] Steward Observatory, University of Arizona, 933 N. Cherry Avenue, Tucson, AZ 85121, USA
[13] Department of Physics, Massachusetts Institute of Technology, Cambridge, MA 02139, USA
[14] Enrico Fermi Institute, The University of Chicago, 5640 S. Ellis Avenue, Chicago, IL 60615, USA
Received 2010 May 11; accepted 2011 April 15; published 2011 July 6

ABSTRACT

We measure the luminosity and color dependence of galaxy clustering in the largest-ever galaxy redshift survey, the main galaxy sample of the Sloan Digital Sky Survey Seventh Data Release. We focus on the projected correlation function $w_p(r_p)$ of volume-limited samples, extracted from the parent sample of $\sim$700,000 galaxies over 8000 deg^2, extending up to redshift of 0.25. We interpret our measurements using halo occupation distribution (HOD) modeling assuming a ΛCDM cosmology (inflationary cold dark matter with a cosmological constant). The amplitude of $w_p(r_p)$ grows slowly with luminosity for $L < L_*$ and increases sharply at higher luminosities, with a large-scale bias factor $b(>L) \times (\sigma_8/0.8) = 1.06 + 0.21(L/L_*)^{1.12}$, where L is the sample luminosity threshold. At fixed luminosity, redder galaxies exhibit a higher amplitude and steeper correlation function, a steady trend that runs through the "blue cloud" and "green valley" and continues across the "red sequence." The cross-correlation of red and blue galaxies is close to the geometric mean of their autocorrelations, dropping slightly below at $r_p < 1\,h^{-1}$ Mpc. The luminosity trends for the red and blue galaxy populations separately are strikingly different. Blue galaxies show a slow but steady increase of clustering strength with luminosity, with nearly constant shape of $w_p(r_p)$. The large-scale clustering of red galaxies shows little luminosity dependence until a sharp increase at $L > 4\,L_*$, but the lowest luminosity red galaxies (0.04–0.25 L_*) show very strong clustering on small scales ($r_p < 2\,h^{-1}$ Mpc). Most of the observed trends can be naturally understood within the ΛCDM+HOD framework. The growth of $w_p(r_p)$ for higher luminosity galaxies reflects an overall shift in the mass scale of their host dark matter halos, in particular an increase in the minimum host halo mass $M_{\min}$. The mass at which a halo has, on average, one satellite galaxy brighter than L is $M_1 \approx 17\,M_{\min}(L)$ over most of the luminosity range, with a smaller ratio above L_*. The growth and steepening of $w_p(r_p)$ for redder galaxies reflects the increasing fraction of galaxies that are satellite systems in high-mass halos instead of central systems in low-mass halos, a trend that is especially marked at low luminosities. Our extensive measurements, provided in tabular form, will allow detailed tests of theoretical models of galaxy formation, a firm grounding of semiempirical models of the galaxy population, and new constraints on cosmological parameters from combining real-space galaxy clustering with mass-sensitive statistics such as redshift-space distortions, cluster mass-to-light ratios, and galaxy–galaxy lensing.

Key words: cosmology: observations – cosmology: theory – galaxies: distances and redshifts – galaxies: halos – galaxies: statistics – large-scale structure of universe

Online-only material: color figures

1. INTRODUCTION

Three-dimensional maps of the large-scale distribution of galaxies reveal a rich network of filaments and sheets, punctuated by dense clusters and interleaved with low-density tunnels and bubbles (Gregory & Thompson 1978; Kirshner et al. 1981; Davis et al. 1982; Giovanelli et al. 1986; Geller & Huchra 1989; Shectman et al. 1996; Colless et al. 2001). Different classes of galaxies trace this structure differently, with early-type galaxies residing preferentially in rich groups and clusters and late-type galaxies residing preferentially in the filaments and walls; this segregation of clustering was already evident in two-dimensional studies as early as those of Hubble (1936, p. 79). Galaxy surveys map the distribution of visible baryons, but a combination of observational and theoretical arguments, beginning with Zwicky (1933, 1937), show that the galaxies trace an underlying network of invisible, gravitationally dominant dark matter. In this paper, we measure the clustering of galaxies as a function of luminosity and color in the largest galaxy redshift survey to date, the main galaxy sample (Strauss et al. 2002) of the

Seventh Data Release (DR7; Abazajian et al. 2009) of the Sloan Digital Sky Survey (SDSS; York et al. 2000). Our primary tool is the two-point correlation function $\xi(r)$, which provides a simple, robust, and informative measure of galaxy clustering (e.g., Peebles 1980). More specifically, we focus on the projected correlation function $w_p(r_p)$, which integrates out redshift-space distortions caused by galaxy peculiar velocities (Davis & Peebles 1983). By modeling our measurements in the context of the ΛCDM cosmological framework (inflationary cold dark matter with a cosmological constant), we infer the relation between different classes of galaxies and the underlying distribution of dark matter, providing fundamental tests for theories of galaxy formation.

Over the last few decades, a variety of "local" clustering studies have established an increasingly refined and quantitative characterization of the dependence of galaxy clustering on luminosity, morphology, color, and spectral type (e.g., Davis & Geller 1976; Davis et al. 1988; Hamilton 1988; Alimi et al. 1988; Valls-Gabaud et al. 1989; Loveday et al. 1995; Benoist et al. 1996; Guzzo et al. 1997; Willmer et al. 1998; Brown et al. 2000; Norberg et al. 2001, 2002; Zehavi et al. 2002, 2005b; Budavari et al. 2003; Madgwick et al. 2003; Li et al. 2006; Swanson et al. 2008; Loh et al. 2010). Luminous galaxies generally cluster more strongly than faint galaxies, reflecting their tendency to reside in denser environments. Galaxies with bulge-dominated morphologies, red colors, or spectral types indicating old stellar populations also exhibit stronger clustering and a preference for dense environments. Significant progress has also been made in recent years in measuring galaxy clustering at intermediate and high redshifts (e.g., Brown et al. 2003; Daddi et al. 2003; Adelberger et al. 2005; Ouchi et al. 2005; Lee et al. 2006; Phleps et al. 2006; Coil et al. 2006, 2008; Meneux et al. 2008, 2009; Abbas et al. 2010).

Cosmological inferences from galaxy clustering measurements are complicated by the existence of galaxy bias, the difference between the distribution of galaxies and that of the underlying dark matter. While the gravitational clustering of dark matter from specified initial conditions can be computed reliably with cosmological N-body simulations, the detailed physics of galaxy formation—gas cooling, star formation, and the feedback effects of star formation and black hole accretion—is only partly understood, so galaxy bias cannot be predicted robustly from first principles. Cosmological parameter studies must adopt a mathematical description of galaxy bias and marginalize over its uncertain parameters. This procedure is most straightforward at large scales, where the effects of bias are expected to be simple, i.e., a scale-independent amplification of the matter $\xi(r)$ (Kaiser 1984; Bardeen et al. 1986; Coles 1993; Fry & Gaztañaga 1993; Mann et al. 1998; Scherrer & Weinberg 1998; Narayanan et al. 2000). Conversely, for a specified cosmological model, one can constrain detailed descriptions of galaxy bias and thus gain insights into galaxy formation physics.

In the cold dark matter scenario (Peebles 1982; Blumenthal et al. 1984), which is now supported by a wide range of observational evidence (e.g., Dunkley et al. 2009; Reid et al. 2010), galaxies form and reside in extended dark matter halos. The existence of such halos is well established by studies of spiral galaxy rotation curves (e.g., Rubin et al. 1978; Persic et al. 1996; Verheijen 2001) and the stellar dynamics (e.g., Gerhard et al. 2001) and gravitational lensing (e.g., Bolton et al. 2008) of elliptical galaxies. Studies of weak lensing and satellite galaxies show that the halos of luminous galaxies extend to hundreds of kpc, where they join smoothly onto the larger scale distribution

of dark matter (e.g., Zaritsky & White 1994; Fischer et al. 2000; Prada et al. 2003; Mandelbaum et al. 2006). The formation of dark matter halos is dominated by gravity and can be well predicted for a given cosmology from high-resolution numerical simulations and analytic models. Dark matter halos thus become the natural bridge for connecting the galaxy distribution and the matter distribution.

In recent years, the theoretical understanding of galaxy clustering has been enhanced through development of the halo occupation distribution (HOD) framework (e.g., Jing et al. 1998; Ma & Fry 2000; Peacock & Smith 2000; Seljak 2000; Scoccimarro et al. 2001; Berlind & Weinberg 2002; Cooray & Sheth 2002; Yang et al. 2003; Kravtsov et al. 2004; Zheng et al. 2005). The HOD formalism describes the "bias" relation between galaxies and mass at the level of individual dark matter halos, in terms of the probability distribution that a halo of virial mass M_h contains N galaxies of a given type, together with prescriptions for the relative spatial and velocity bias of galaxies and dark matter within virialized halos. The combination of a cosmological model and a fully specified HOD can predict any galaxy clustering statistic on any scale, allowing integrated constraints from many observations. For an assumed cosmological model and a parameterized form of the HOD motivated by contemporary theories of galaxy formation (e.g., Kauffmann et al. 1997, 1999; Benson et al. 2000; Berlind et al. 2003; Kravtsov et al. 2004; Zheng et al. 2005; Conroy et al. 2006), measurements of $w_p(r_p)$ are already highly constraining, and HOD modeling transforms data on galaxy pair counts into a physical relation between galaxies and dark matter halos. HOD modeling has been applied to interpret clustering data from a number of surveys at low and high redshifts (e.g., Jing & Börner 1998; Jing et al. 2002; Bullock et al. 2002; Moustakas & Somerville 2002; van den Bosch et al. 2003b; Magliocchetti & Porciani 2003; Yan et al. 2003; Zheng 2004; Yang et al. 2005a; Zehavi et al. 2005b; Cooray 2006; Hamana et al. 2006; Lee et al. 2006, 2008; Zheng et al. 2007, 2009; White et al. 2007; Blake et al. 2008; Brown et al. 2008; Quadri et al. 2008; Wake et al. 2008; Kim et al. 2009; Ross et al. 2010).

In principle, a complete model of galaxy bias might need to allow for the possibility that the average galaxy content of halos depends on large-scale environment as well as halo mass, since halo concentrations and assembly histories show some environmental correlations (Sheth & Tormen 2004; Gao et al. 2005; Harker et al. 2006; Wechsler et al. 2006; Zhu et al. 2006; Croton et al. 2007; Jing et al. 2007; Wetzel et al. 2007; Dalal et al. 2008; Zu et al. 2008). However, studies assuming an environment-independent HOD have proven successful at explaining galaxy clustering in different density regimes (Abbas & Sheth 2006, 2007; Tinker et al. 2008; Skibba et al. 2009; see also Blanton et al. 2006; Blanton & Berlind 2007), and theoretical models predict only a small impact of such "halo assembly bias" on galaxy clustering statistics for mass- or luminosity-thresholded samples (Yoo et al. 2006; Croton et al. 2007; Zu et al. 2008).

The present paper builds upon our investigation of galaxy correlations in early SDSS redshift data (Zehavi et al. 2002), our use of HOD modeling to interpret deviations from a power law in the galaxy two-point correlation function (Zehavi et al. 2004), and, especially, our earlier investigation of luminosity and color dependence of the galaxy correlation function in a sample of about 200,000 SDSS galaxies (Zehavi et al. 2005b, hereafter Z05). Here, we take advantage of the final SDSS galaxy sample—roughly three times more galaxies once

appropriate cuts are applied—and advances in HOD modeling methods to obtain higher precision measurements and tighter, more informative constraints on galaxy–halo relations. This study complements correlation function measurements and HOD models of the SDSS luminous red galaxy (LRG) sample (Eisenstein et al. 2001, 2005; Zehavi et al. 2005a; Zheng et al. 2009; Kazin et al. 2010; Watson et al. 2010), which probes the most luminous galaxies out to redshift $z \approx 0.45$ (Eisenstein et al. 2001). We focus our analysis on volume-limited samples of well-defined galaxy classes, which allows us to construct HOD models with a small number of free parameters to interpret the measurements for each class. This approach complements other analyses of the SDSS main galaxy sample that measure luminosity or stellar mass-weighted correlation functions (Li & White 2009, 2010) or use marked correlation functions to quantify luminosity and color dependence (Skibba et al. 2006; Skibba & Sheth 2009). These analyses typically yield smaller error bars because they use more sample galaxies for the measurement, but they require a more complete global description of the galaxy population to model the results. There are many parallels between our program and the one pursued by van den Bosch, Mo, Yang, and their collaborators (e.g., papers cited above and van den Bosch et al. 2003a, 2007; Weinmann et al. 2006; Yang et al. 2008; More et al. 2009), though they have largely focused on analysis of group catalogs (Yang et al. 2005b, 2007) rather than detailed fitting of the correlation function. The two approaches yield qualitatively similar results (e.g., Z05; Yang et al. 2005a, 2008; Zheng et al. 2007).

Our correlation function measurements provide basic empirical characterizations of large-scale structure at low redshift ($z < 0.25$), and the luminosity and color dependence of these correlation functions can test predictions from hydrodynamic cosmological simulations (e.g., Pearce et al. 2001; Weinberg et al. 2004) or semianalytic models (e.g., Kang et al. 2005; Croton et al. 2006; Bower et al. 2006). The derived HOD constraints provide informative tests of galaxy formation models, a low-redshift baseline for evolutionary studies (e.g., Zheng et al. 2007; Brown et al. 2008), and a description that can be used to create realistic mock catalogs from simulations (Scoccimarro & Sheth 2002; Wechsler 2004; Eisenstein et al. 2005; Skibba & Sheth 2009; C. K. McBride et al. 2011, in preparation). As discussed extensively by Zheng & Weinberg (2007), the HOD formalism can also be used in cosmological parameter determinations, allowing marginalization over the parameters of a bias prescription that applies to a wide range of clustering statistics from the linear to the highly nonlinear regime. Combinations of spatial clustering statistics and dynamically sensitive measures (such as galaxy–galaxy lensing, redshift-space distortions, or group and cluster mass-to-light ratios) can break the main degeneracies between cosmological parameters and galaxy bias. A number of papers have implemented variants of this approach to constrain the matter density parameter Ω_m and the amplitude of matter clustering σ_8 (van den Bosch et al. 2003a, 2007; Abazajian et al. 2005; Tinker et al. 2005; Cacciato et al. 2009; Rozo et al. 2010). These analyses argued for a significant downward revision of the *WMAP1* values of Ω_m and/or σ_8, anticipating the parameter changes that occurred with *WMAP3* (see also Vale & Ostriker 2006, who reached a similar conclusion by a related method). Our correlation function measurements are providing essential constraints for such analyses using the SDSS DR7 data set.

The paper is organized as follows. Section 2 describes the SDSS data and the methods we use to measure galaxy clustering and to interpret it via HOD modeling. In Section 3, we present

results on the luminosity dependence of $w_p(r_p)$ and its implications for HOD models. In Section 4, we examine the dependence of clustering on galaxy color, including cross-correlations between red and blue galaxy samples, and investigate the luminosity dependence for red and blue galaxies separately. Section 5 summarizes our results. Appendix A discusses some technical issues relating to predictions of the galaxy cross-correlation function. Appendix B illustrates the robustness of our measurements to different systematics. Appendix C presents in tabular form the $w_p(r_p)$ measurements for most of the samples discussed in the paper.

2. OBSERVATIONS AND METHODS

2.1. Data

The SDSS (York et al. 2000; Stoughton et al. 2002) was an ambitious project to map most of the high-latitude sky in the northern Galactic cap, using a dedicated 2.5 m telescope (Gunn et al. 2006). The survey started regular operations in 2000 April and completed observations (for SDSS-II) in 2008 July. A drift-scanning mosaic CCD camera (Gunn et al. 1998) imaged the sky in five photometric bandpasses (Fukugita et al. 1996; Smith et al. 2002) to a limiting magnitude of $r \sim 22.5$. The imaging data were processed through a series of pipelines that perform astrometric calibration (Pier et al. 2003), photometric reduction (Lupton et al. 1999, 2001), and photometric calibration (Hogg et al. 2001; Ivezić et al. 2004; Tucker et al. 2006; Padmanabhan et al. 2008). Objects were selected for spectroscopic follow-up using specific algorithms for the main galaxy sample (Strauss et al. 2002), luminous red galaxies (Eisenstein et al. 2001), and quasars (Richards et al. 2002). Targets were assigned to spectroscopic plates using an adaptive tiling algorithm (Blanton et al. 2003a) and observed with a pair of fiber-fed spectrographs. Spectroscopic data reduction and redshift determination were performed by automated pipelines. Galaxy redshifts were measured with a success rate greater than 99% and typical accuracy of 30 km s^{-1}. To a good approximation, the main galaxy sample consists of all galaxies with Petrosian magnitude $r < 17.77$, with a median redshift of $\sim$0.1. The LRG redshift sample uses color–magnitude cuts to select galaxies with $r < 19.5$ that are likely to be luminous early-type galaxies, extending up to redshift $\sim$0.5.

Galaxy samples suitable for large-scale structure studies have been carefully constructed from the SDSS redshift data (Blanton et al. 2005b). All magnitudes are K-corrected (Blanton et al. 2003b) and evolved to rest-frame magnitudes at $z = 0.1$ (which is near the median redshift of the sample and thus minimizes corrections) using an updated version of the evolving luminosity function model of Blanton et al. (2003c).[15] The radial selection function is derived from the sample selection criteria. When creating volume-limited samples below, we include a galaxy if its evolved, redshifted spectral energy distribution places it within the main galaxy sample's apparent magnitude and surface brightness limits at the limiting redshift of the sample. The angular completeness is characterized carefully for each sector (a unique region of overlapping spectroscopic plates) on the sky.

Due to the placement of fibers to obtain spectra, no two targets on the same plate can be closer than 55″. This results in $\sim$7% of targeted galaxies not having a measured redshift. We assign these galaxies the redshift of their nearest neighboring galaxy;

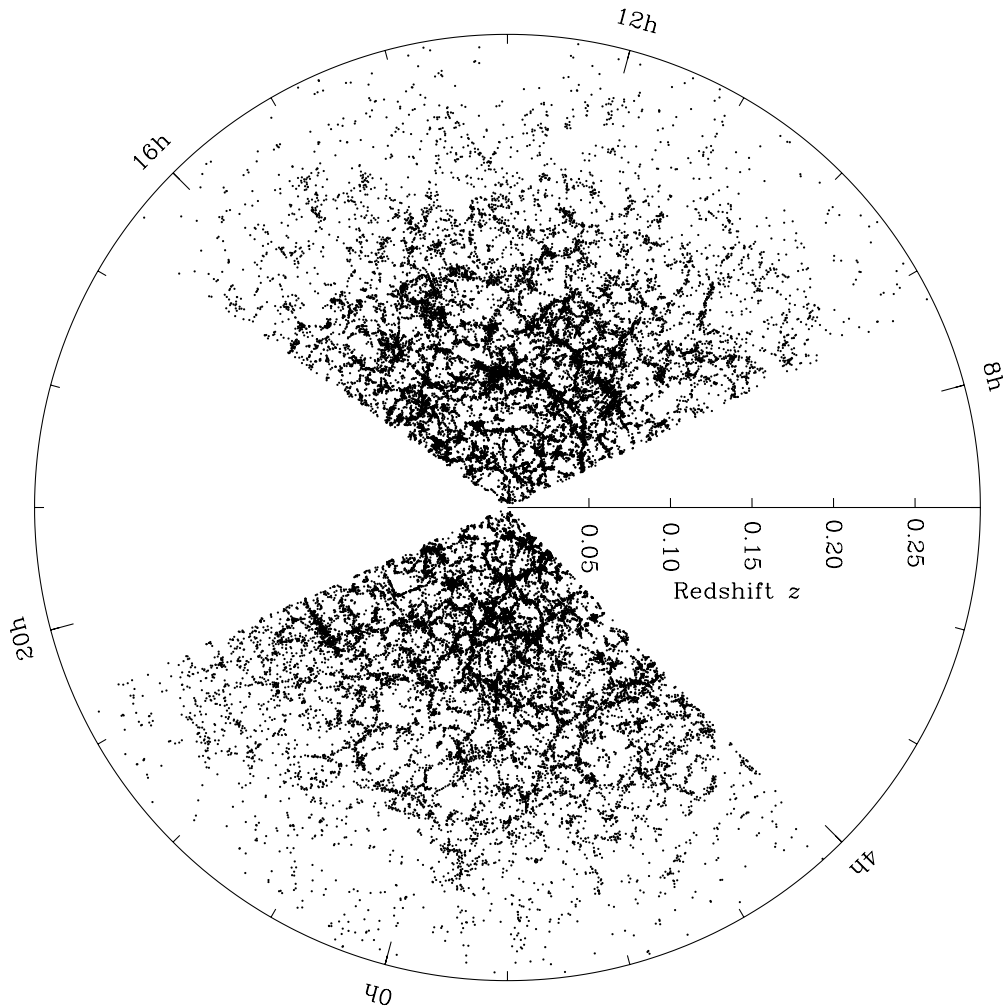---

[15] http://sdss.physics.nyu.edu/vagc/lss.html

Figure 1. Distribution of galaxies in the SDSS main galaxy sample. Only galaxies within ±1.25 deg of the celestial equator are shown.

roughly speaking, this method double-weights the galaxy that *was* observed, but it retains the additional information present in the angular position of the "collided" galaxy. As shown in Z05, this treatment works remarkably well for projected statistics such as $w_p(r_p)$, above the physical scale corresponding to $55''$ ($r_p \approx 0.13\,h^{-1}$ Mpc at the outer edge of our sample). We thus limit the measurements in this paper to scales larger than that. The median deviation of $w_p(r_p)$ for the range of separations we utilize is 0.2%, much less than the statistical errors on the measurements (Figure 3 in Z05). It is, in fact, possible to correct for fiber collisions down to scales as small as $0.01\,h^{-1}$ Mpc using the ratio of small-angle pairs in the spectroscopic and photometric catalogs (Masjedi et al. 2006; Li et al. 2006; Li & White 2009), but we have not implemented this technique here.

The clustering measurements in this paper are based on SDSS DR7 (Abazajian et al. 2009), which marks the completion of the original goals of the SDSS and the end of the phase known as SDSS-II. The associated NYU Value-Added Galaxy Catalog (NYU-VAGC)[15] includes approximately 700,000 main sample galaxies over about 8000 deg² on the sky. This data set can be compared to the much smaller sky coverage of the samples in previous correlation function analyses of the SDSS main galaxy sample: Zehavi et al. (2002) used an early sample of ~700 deg², and Z05 analyzed a sample of about 2500 deg². The contiguous northern footprint of DR7 offers further advantage over earlier data sets by reducing boundary effects. Figures 1–3 show the

distribution of the main sample galaxies in right ascension and redshift for slices near the celestial equator. These plots nicely illustrate the large-scale structure we aim to study using the two-point correlation function as well as the potential dependencies on galaxy properties. Diagrams that show contiguity of structure over multiple SDSS slices appear in Choi et al. (2010), who analyze the topology of large-scale structure in the DR7 main galaxy sample.

Throughout this paper, we refer to distances in comoving units, and for all distance calculations and absolute magnitude definitions we adopt a flat ΛCDM model with $\Omega_m = 0.3$. We quote distances in h^{-1} Mpc (where $h \equiv H_0/100\,\mathrm{km\ s^{-1}\ Mpc^{-1}}$) and absolute magnitudes for $h = 1$. Our correlation function measurements are strictly independent of H_0, except that the absolute magnitudes we list as M_r are really values of $M_r + 5\log h$. Changing the assumed Ω_m or Ω_Λ would have a small impact on our measurements by changing the distance–redshift relation and thus shifting galaxies among luminosity bins and galaxy pairs among radial separation bins. However, even at our outer redshift limit of $z = 0.25$, the effect of lowering Ω_m from 0.3 to 0.25 is only 1% in distance, so our measurements are effectively independent of cosmological parameters within their observational uncertainties.

In order to work with well-defined classes of galaxies, we study volume-limited samples constructed for varying luminosity bins and luminosity thresholds. While volume-limited
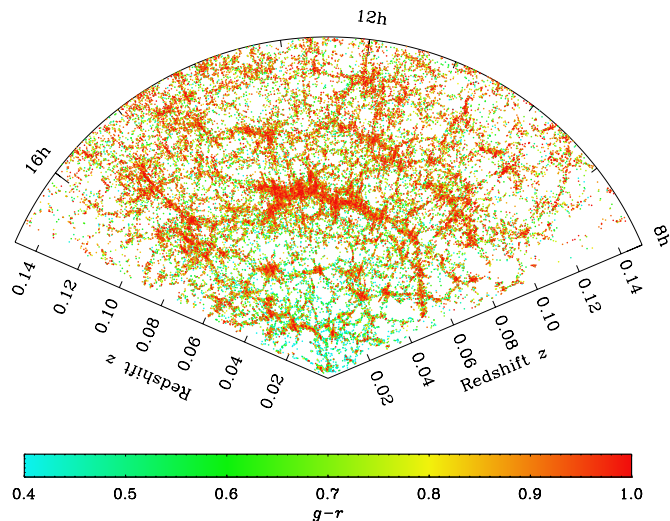
Figure 2. Slice through the SDSS main galaxy sample, with galaxies color-coded based on rest-frame $g - r$ color. The slice shows galaxies within ± 4 deg of the celestial equator, in the north Galactic cap. The redshift limit is smaller than in Figure 1 to better reveal details of structure. The large structure cutting across the center of the map is the "Sloan Great Wall" (Gott et al. 2005) discussed in Section 3.2.

Figure 3. Same as Figure 2, but with galaxies color-coded by absolute magnitude. The size of the dots is also proportional to galaxy luminosity. As expected for a flux-limited survey, more luminous galaxies dominate at larger redshifts.

subsamples include fewer galaxies than the full flux-limited sample, they are much easier to interpret. For a given luminosity bin, we discard the galaxies that are too faint to be included at the far redshift limit or too bright to be included at the near limit. We include galaxies with $14.5 < r < 17.6$, with the conservative bright limit imposed to avoid small incompletenesses associated with galaxy deblending (the NYU-VAGC `safe` samples). We further cut these samples by color, using the K-corrected $g - r$ color as a separator into different populations. We also study a set of luminosity-threshold samples, namely, volume-limited samples of all galaxies brighter than a given threshold, as these yield higher precision measurements than luminosity-bin samples and are somewhat more straightforward for HOD modeling. For these samples we relax the bright flux limit to $r > 10.0$, in order to be able to define a viable volume-limited redshift range (the NYU-VAGC `bright` samples). The distribution in magnitude and redshift and the cuts used to define the samples are shown in Figure 4. Details of the samples are given in Tables 1 and 2. For luminosity-threshold samples, one could improve statistics by using the flux-limited galaxy catalog and weighting galaxy pairs by the inverse volume over which they can be observed, as done by Li & White (2009, 2010) for samples weighted by stellar mass and luminosity. This procedure would extend the outer redshift limit for the more luminous galaxies above the threshold, thus reducing sample variance, but it has the arguable disadvantage of using different measurement volumes for different subsets of galaxies within the sample, and we have not implemented it here.

The full spectroscopic survey of the SDSS DR7 Legacy survey contains 900,000 unique, survey-quality galaxy spectra over 8000 deg^2. Of these objects, the main galaxy sample target criteria selected 700,000. SDSS targeted the remainder as LRG candidates (around 100,000) or in other categories (e.g., as quasar candidates or in special programs on the Equator). We use a reduced footprint of 7700 deg^2, which excludes areas of suspect photometric calibration (Padmanabhan et al. 2008) and incomplete regions near bright stars. This reduction leaves 670,000 main sample galaxies. Because we are using an updated photometric reduction, a substantial fraction of targets are
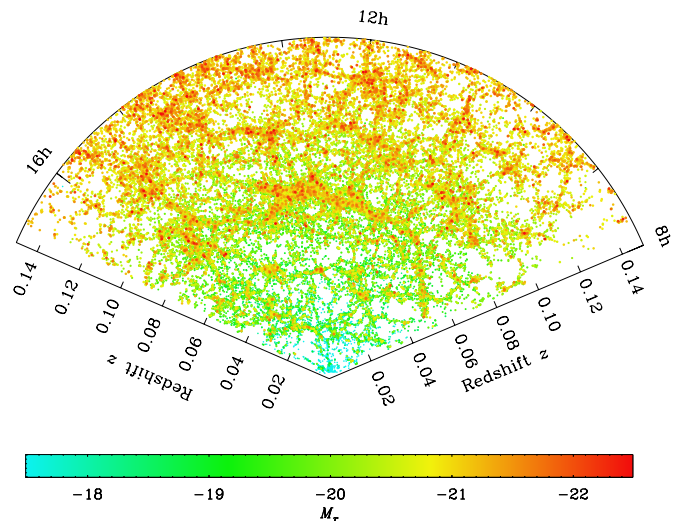
assigned fluxes fainter than the original flux limit, which further reduces the sample to about 640,000 galaxies. For uniformity we have imposed an even stricter faint limit of $r = 17.6$ in this paper, which yields 540,000 galaxies. About 30,000 of the original targets at that flux limit were not assigned fibers because of fiber collisions; we assign these objects the redshift of their nearest neighbor as discussed above. The resulting sample of 570,000 galaxies constitutes the parent sample for all of the volume-limited samples in this paper. When we apply a bright magnitude cut of $r = 14.5$, it eliminates about 6000 galaxies. Further details and the samples themselves are available as part of the public NYU-VAGC data sets.

2.2. Clustering Measures

The autocorrelation function is a powerful way to characterize galaxy clustering, measuring the excess probability over random of finding pairs of galaxies as a function of separation (e.g., Peebles 1980). To separate effects of redshift distortions from spatial correlations, it is customary to estimate the galaxy correlation function on a two-dimensional grid of pair separations parallel (π) and perpendicular (r_p) to the line of sight. Following the notation of Fisher et al. (1994), for a pair of galaxies with redshift positions $\mathbf{v}_1$ and $\mathbf{v}_2$, we define the redshift separation vector $\mathbf{s} \equiv \mathbf{v}_1 - \mathbf{v}_2$ and the line-of-sight vector $\mathbf{l} \equiv \frac{1}{2}(\mathbf{v}_1 + \mathbf{v}_2)$. The parallel and perpendicular separations are then

$$\pi \equiv |\mathbf{s} \cdot \mathbf{l}|/|\mathbf{l}|, \qquad r_p{}^2 \equiv \mathbf{s} \cdot \mathbf{s} - \pi^2. \qquad (1)$$

To estimate the pair counts expected for unclustered objects while accounting for the complex survey geometry, we generate volume-limited random catalogs with the detailed angular selection function of the samples. For the different galaxy samples, we use random catalogs with 25–300 times as many galaxies, depending on the varying number density and size of the samples. We have verified that increasing the number of random galaxies or replacing the random catalog with another one makes a negligible difference to the measurements. We estimate $\xi(r_p, \pi)$ using the Landy & Szalay (1993) estimator

$$\xi(r_p, \pi) = \frac{\text{DD} - 2\text{DR} + \text{RR}}{\text{RR}}, \qquad (2)$$
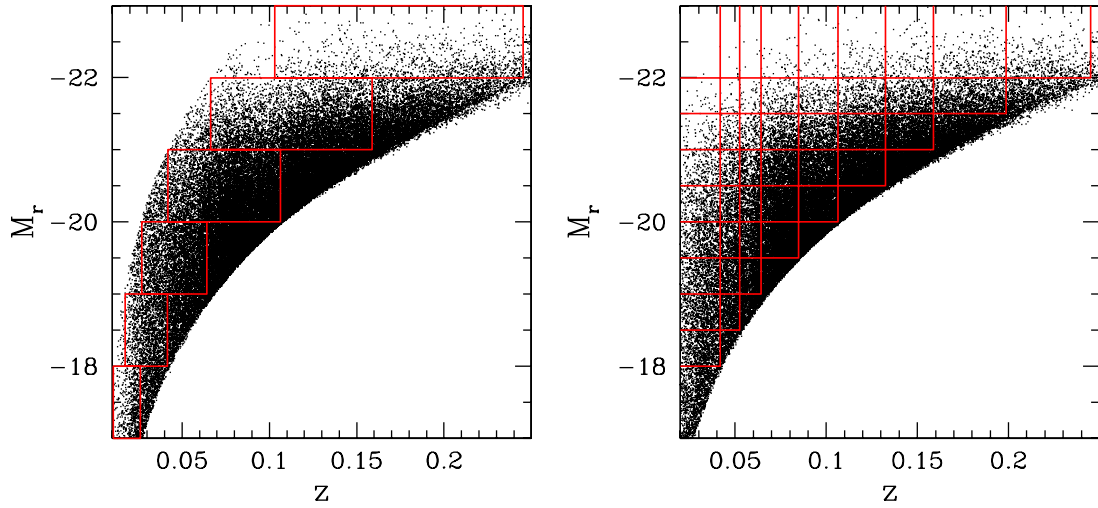
Figure 4. Distribution in redshift and *r*-band absolute magnitude for the SDSS sample with the imposed flux limits. We plot a random subset of the SDSS galaxies, sparsely sampled by a factor of 10. The lines show the magnitude and redshift ranges of the different volume-limited samples used in this paper. Luminosity-bin samples are shown on the left and luminosity-threshold samples on the right. All luminosity-threshold samples have $z_{min} = 0.02$, so a sample consists of the set of galaxies above the horizontal line marking the M_r threshold and left of the corresponding vertical line marking z_{max}. As discussed in Section 2.1, we *K*-correct all galaxy magnitudes to redshift $z = 0.1$, and we quote absolute magnitudes for $h = 1$.

(A color version of this figure is available in the online journal.)

Table 1
Volume-limited Correlation Function Samples Corresponding to Luminosity Bins

M_r	cz_{min}	cz_{max}	N_{gal}	N_{blue}	N_{red}	r_0	γ	$\frac{\chi^2}{dof}$	$r_0{}^d$	γ^d	$\bar{n}$	$\langle M_r \rangle$	π_{max}
−23 to −22	30,900	73,500	10,251	1,797	8,452	10.47 ± 0.25	1.92 ± 0.03	2.4	10.40 ± 0.18	1.94 ± 0.02	0.004	−22.22	60
−22 to −21	19,900	47,650	73,746	27,496	46,249	5.98 ± 0.11	1.92 ± 0.02	5.0	6.30 ± 0.06	1.88 ± 0.01	0.111	−21.32	60
−21 to −20	12,600	31,900	108,629	50,879	57,749	5.46 ± 0.15	1.77 ± 0.02	3.8	5.80 ± 0.09	1.75 ± 0.01	0.530	−20.42	60
−21 to −20	12,600	19,250*	17,853	8,103	9,749	4.82 ± 0.23	1.87 ± 0.03	2.5	5.33 ± 0.13	1.81 ± 0.03	0.530	−20.42	40
−20 to −19	8,050	19,250	44,348	25,455	18,892	4.89 ± 0.26	1.78 ± 0.02	3.8	5.19 ± 0.13	1.80 ± 0.02	1.004	−19.47	60
−19 to −18	5,200	12,500	18,200	13,035	5,165	4.14 ± 0.30	1.81 ± 0.03	2.3	4.59 ± 0.18	1.93 ± 0.04	1.300	−18.48	40
−18 to −17	3,200	7,850	5,965	4,970	995	2.09 ± 0.38	1.99 ± 0.14	2.0	4.37 ± 0.37	1.91 ± 0.08	1.972	−17.46	40

Notes. All samples use $14.5 < m_r < 17.6$. r_0 and γ are obtained from fitting a power law to $w_p(r_p)$ using the full error covariance matrices, while $r_0{}^d$ and γ^d are obtained when using just the diagonal elements. For all samples, the number of degrees of freedom (dof) is 9 (11 measured w_p values minus the 2 fitted parameters). $\bar{n}$ is measured in units of $10^{-2} h^3$ Mpc^{-3}. A handful of galaxies do not have well-measured colors, so N_{blue} and N_{red} do not sum to N_{gal}. The smaller $-21 < M_r < -20$ sample, indicated with an asterisk, is limited to a smaller redshift range to avoid the effects of the Sloan Great Wall (see the text).

Table 2
Volume-limited Correlation Function Samples Corresponding to Luminosity Thresholds

M_r^{max}	cz_{max}	N_{gal}	N_{blue}	N_{red}	r_0	γ	$\frac{\chi^2}{dof}$	$r_0{}^d$	γ^d	$\bar{n}$	π_{max}
−22.0	73,500	11,385	2,145	9,237	10.71 ± 0.24	1.91 ± 0.03	3.2	10.56 ± 0.17	1.92 ± 0.02	0.005	60
−21.5	59,600	39,456	10,576	28,876	7.27 ± 0.14	2.00 ± 0.01	8.8	7.68 ± 0.08	1.94 ± 0.01	0.028	60
−21.0	47,650	83,238	30,159	53,075	5.98 ± 0.12	1.96 ± 0.02	6.1	6.46 ± 0.06	1.90 ± 0.01	0.116	60
−20.5	39,700	132,225	54,827	77,395	5.60 ± 0.12	1.90 ± 0.01	3.2	6.01 ± 0.06	1.85 ± 0.01	0.318	60
−20.0	31,900	141,733	62,862	78,868	5.54 ± 0.14	1.83 ± 0.01	3.8	6.00 ± 0.09	1.79 ± 0.01	0.656	60
−20.0	19,250*	30,245	12,733	17,510	5.24 ± 0.28	1.87 ± 0.03	1.2	5.53 ± 0.13	1.85 ± 0.02	0.656	60
−19.5	25,450	132,664	62,892	69,770	5.11 ± 0.17	1.81 ± 0.02	1.8	5.37 ± 0.08	1.81 ± 0.01	1.120	60
−19.5	19,250*	51,498	24,005	27,491	5.17 ± 0.27	1.84 ± 0.03	2.3	5.36 ± 0.13	1.85 ± 0.02	1.120	60
−19.0	19,250	77,142	39,554	37,585	4.86 ± 0.27	1.85 ± 0.03	3.2	5.23 ± 0.12	1.85 ± 0.02	1.676	60
−18.5	15,750	58,909	32,554	26,355	4.48 ± 0.33	1.86 ± 0.04	2.1	5.33 ± 0.18	1.83 ± 0.03	2.311	40
−18.0	12,500	39,027	23,159	15,868	4.10 ± 0.34	1.85 ± 0.04	1.8	4.75 ± 0.17	1.91 ± 0.04	3.030	40

Notes. All samples use $10.0 < m_r < 17.6$. z_{min} for the samples is 0.02. r_0 and γ are obtained from fitting a power law to $w_p(r_p)$ using the full error covariance matrices, while $r_0{}^d$ and γ^d are obtained when using just the diagonal elements. For all samples, the number of degrees of freedom (dof) is 9 (11 measured w_p values minus the two fitted parameters). $\bar{n}$ is measured in units of $10^{-2} h^3$ Mpc^{-3}. The samples indicated with an asterisk are limited to a smaller redshift range to avoid the effects of the large supercluster (see the text).

where DD, DR, and RR are the suitably normalized numbers of weighted data–data, data–random, and random–random pairs in each separation bin. We weight the galaxies (real and random) according to the angular selection function; because we are using volume-limited samples, we do not weight by a radial selection function. We also tested the alternative ξ estimators of Hamilton (1993) and Davis & Peebles (1983) and found only small differences in the measurements. See Appendix B for these and other tests of our standard analysis procedures.

To examine the real-space correlation function, we follow standard practice and compute the projected correlation function

$$w_p(r_p) = 2 \int_0^\infty d\pi \, \xi(r_p, \pi). \qquad (3)$$

In practice, for most samples we integrate up to $\pi_{\max} = 60 \, h^{-1}$ Mpc, which is large enough to include most correlated pairs and gives a stable result by suppressing noise from distant, uncorrelated pairs. For samples with low outer redshift limits we use $\pi_{\max} = 40 \, h^{-1}$ Mpc (see Tables 1 and 2). We use these $\pi_{\max}$ values consistently when performing HOD modeling of the clustering results (not including the small residual effects of redshift-space distortions). We use linearly spaced bins in π with widths of $2 \, h^{-1}$ Mpc. Our bins in separation r_p are logarithmically spaced with widths of 0.2 dex. We checked the robustness to binning in r_p and π and found our results to be insensitive to either. The measurements are quoted at the pair-weighted average separation in the bin. We estimate that this separation varies by at most 1% from the r_p for which $w_p(r_p)$ equals the pair-weighted average of w_p in the bin. This corresponds to a change of the same magnitude in w_p, significantly smaller than the statistical errors on the measurements, and an up to 0.5% shift in the best-fit correlation length.

The projected correlation function can be related to the real-space correlation function, $\xi(r)$, by

$$w_p(r_p) = 2 \int_{r_p}^\infty r \, dr \, \xi(r) \left(r^2 - r_p{}^2\right)^{-1/2} \qquad (4)$$

(Davis & Peebles 1983). In particular, for a power law $\xi(r) = (r/r_0)^{-\gamma}$, one obtains

$$w_p(r_p) = r_p \left(\frac{r_p}{r_0}\right)^{-\gamma} \Gamma\left(\frac{1}{2}\right) \Gamma\left(\frac{\gamma-1}{2}\right) \Big/ \Gamma\left(\frac{\gamma}{2}\right), \qquad (5)$$

allowing one to infer the best-fit power law for $\xi(r)$ from w_p. Alternatively, one can invert w_p to get $\xi(r)$ independent of the power-law assumption. Here, however, we focus on w_p itself, as this is the statistic measured directly from the data that is determined by the real-space correlation function. We note that Equation (5) strictly holds only in the limit of integrating to infinity to obtain w_p. For most of our measurements used in the fits, however, $r_p \lesssim \pi_{\max}/4$, and this has a minimal effect. In this paper, we focus on HOD modeling of the measurements (using the finite $\pi_{\max}$ values consistently) and provide power-law fits only as qualitative guidelines, but see Coil et al. (2008) for a possible way to modify the power-law fitting.

We estimate statistical errors on our different measurements using jackknife resampling, as in Z05. We define 144 spatially contiguous subsamples of the full data set, each covering approximately 55 deg^2 on the sky. Our jackknife samples are then created by omitting each of these subsamples in turn. The error covariance matrix is estimated from the total dispersion among the jackknife samples,

$$\text{Covar}(\xi_i, \xi_j) = \frac{N-1}{N} \sum_{l=1}^N \left(\xi_i{}^l - \bar{\xi}_i\right)\left(\xi_j{}^l - \bar{\xi}_j\right), \qquad (6)$$

where $N = 144$ in our case and $\bar{\xi}_i$ is the mean value of the statistic ξ measured in radial bin i in all the samples (ξ denotes here the statistic at hand, whether it is ξ or w_p). In Z05 we used

$N = 104$ for the smaller sample. The larger value here is chosen to enable better estimation of the full covariance matrix, while still allowing each excluded subvolume to be sufficiently large.

Norberg et al. (2009) have recently studied a variety of error estimators for dark matter correlation functions in N-body simulations, comparing internal methods such as jackknife and bootstrap to external estimates derived from multiple independent catalogs, each comparable in size to our L_* galaxy samples. They find good agreement between jackknife and external estimates for the variance in $w_p(r_p)$ on large scales, with jackknife errors somewhat overestimating the externally derived errors on small scales ($r_p \lesssim 2 \, h^{-1}$ Mpc). Our own tests of the jackknife method on PTHalos mock catalogs (Scoccimarro & Sheth 2002), described by Zehavi et al. (2002, 2004) and Z05, show that it yields error and covariance estimates similar to those derived from multiple independent catalogs (see Figure 2 in Z05). In principle, covariance matrices derived from large numbers of realistic mock catalogs are preferable because they use larger total volumes and include cosmic variance on scales of the full survey (while jackknife or bootstrap estimates only include cosmic variance on the scale of individual subsamples). However, the tests mentioned above suggest that jackknife estimates are sufficient for our purposes, and they are a far more practical tool when working with many subsamples of different clustering properties, as the mock catalog approach would require a new set of realizations mimicking the clustering signal of each one. The Norberg et al. (2009) tests suggest that parameter uncertainties derived using the jackknife errors should, if anything, be conservative. Because of potential noise or systematics in jackknife estimates of the full covariance matrix, we also present some model fits below that use only diagonal elements.

2.3. HOD Modeling

We interpret the clustering measurements in the HOD framework, which describes the bias between galaxies and mass in terms of the probability distribution $P(N|M_h)$ that a halo of virial mass M_h contains N galaxies of a given type. Our modeling effectively translates galaxy clustering measurements for each class of galaxies into halo occupation functions $\langle N(M_h) \rangle$, the mean number of galaxies as a function of halo mass. Other aspects of the HOD—the form of $P(N|\langle N \rangle)$ and the galaxy distribution within halos—are specified by theoretical expectations.

We adopt a spatially flat "concordance" ΛCDM cosmological model with matter density parameter $\Omega_m = 0.25$, and baryon density parameter $\Omega_b = 0.045$, consistent with recent determinations from the cosmic microwave background (CMB; *WMAP5*; Hinshaw et al. 2009; Dunkley et al. 2009; Komatsu et al. 2009), supernova Ia (Kowalski et al. 2008; Kessler et al. 2009), and baryon acoustic oscillations (Percival et al. 2010). Accordingly, we assume a primordial density power spectrum with fluctuations at $8 \, h^{-1}$ Mpc scale of $\sigma_8 = 0.8$. The Hubble constant we use is $H_0 = 70 \, \text{km s}^{-1} \, \text{Mpc}^{-1}$, and we assume an inflationary spectral index $n_s = 0.95$. Lowering Ω_m to 0.25 has only a small effect on our clustering measurements (see Appendix B).

Hydrodynamic simulations show that the most massive galaxy in a halo typically resides at or near the halo center (e.g., Berlind et al. 2003; Simha et al. 2009), in accord with the expectations of semianalytic models (e.g., White & Frenk 1991; Kauffmann et al. 1993; Cole et al. 1994). For HOD parameterization, it is useful to separate the contributions of these central

galaxies from those of the additional, satellite galaxies in each halo (Kravtsov et al. 2004; Zheng et al. 2005). For samples of galaxies brighter than a given luminosity, the mean occupation function can be well characterized by a smoothed step function for the central galaxy and a power-law number of satellites increasing with halo mass. We model it in this work using the following form:

$$\langle N(M_h) \rangle = \frac{1}{2} \left[1 + \mathrm{erf} \left(\frac{\log M_h - \log M_{\min}}{\sigma_{\log M}} \right) \right]$$
$$\times \left[1 + \left(\frac{M_h - M_0}{M_1'} \right)^\alpha \right], \qquad (7)$$

where erf is the error function $\mathrm{erf}(x) = \frac{2}{\sqrt{\pi}} \int_0^x e^{-t^2} dt$. The mean occupation function of the central galaxies (the left square brackets times the $1/2$ factor) is a step-like function with a cutoff profile softened to account for the scatter between galaxy luminosity and halo mass (see also More et al. 2009). The mean occupation of the satellite galaxies (the second term in the right square brackets multiplied by the left square brackets times the $1/2$ factor) is a power law modified by a similar cutoff profile. The five free parameters are the mass scale $M_{\min}$ and width $\sigma_{\log M}$ of the central galaxy mean occupation, and the cutoff mass scale M_0, normalization M_1', and high-mass slope α of the satellite galaxy mean occupation function.

This specific form is motivated by the theoretical study presented in Zheng et al. (2005) and is identical to the five-parameter model adopted in Zheng et al. (2007; see also Appendix B of Zheng et al. 2009). It is more flexible than the three-parameter model used in Z05, which has the same basic shape. The five-parameter model introduces two additional parameters to characterize the cutoff profiles of central and satellite galaxies, allowing excellent descriptions of the $\langle N(M_h) \rangle$ functions predicted by hydrodynamic simulations and semianalytic models (Zheng et al. 2005).

Two characteristic halo masses come into play in the modeling, which set the mass scales of halos that host central galaxies and satellites. $M_{\min}$ characterizes the minimum mass of a halo hosting a central galaxy above the luminosity threshold. The exact definition of $M_{\min}$ can vary between different HOD parameterizations; in the form we adopt (Equation (7)), it is the mass for which half of such halos host galaxies above the luminosity threshold, i.e., $\langle N_{\mathrm{cen}}(M_{\min}) \rangle = 0.5$. It can also be interpreted as the mass of halos in which the median luminosity of central galaxies is equal to the luminosity threshold (see Zheng et al. 2007 for details, except that it was incorrectly labeled as *mean* rather than *median* luminosity there). The second characteristic mass scale is M_1, the mass of halos that on average have one additional satellite galaxy above the luminosity threshold, defined by $\langle N_{\mathrm{sat}}(M_1) \rangle = 1$. Note that M_1 is different from M_1' in Equation (7), though it is obviously related to the values of M_1' and M_0.

As is common practice, the distributions of the occupation number of central galaxies and satellite galaxies are assumed to follow the nearest-integer and Poisson distributions, respectively, consistent with theoretical predictions (Kravtsov et al. 2004; Zheng et al. 2005). Boylan-Kolchin et al. (2010) have recently argued that the distributions of subhalo counts in high-mass halos become super-Poisson at high $\langle N_{\mathrm{sat}} \rangle$, but we expect such a distribution to have minimal quantitative impact on our clustering predictions. The spatial distribution of satellite galaxies within halos is assumed to be the same as that of the dark matter, which follows to a good approximation an

Navarro–Frenk–White profile (Navarro et al. 1996). For the halo concentration parameter $c(M_h)$, we adopt the relation given by Bullock et al. (2001), modified to be consistent with our halo definition that the mean density of halos is 200 times the background density: $c(M_h) = c_0(M_h/M_{\mathrm{nl}})^\beta(1+z)^{-1}$, where $c_0 = 11$, $\beta = -0.13$, and $M_{\mathrm{nl}} = 2.26 \times 10^{12} h^{-1} M_\odot$ is the nonlinear mass scale at $z = 0$.

The two-point correlation function of galaxies in our model is calculated using the method described by Tinker et al. (2005), specifically their "$\bar{n}_g'$–matched" method, which improves the algorithm in Zheng (2004) by incorporating a more accurate treatment of the halo exclusion effect. The method, calibrated and tested using mock catalogs, is accurate to 10% or better. We use the measured values of $w_p(r_p)$ with the full error covariance matrices. We also incorporate the observed number density of galaxies in each subsample as an additional constraint on the HOD model, with an assumed 5% uncertainty. That is, we form the χ^2 as

$$\chi^2 = (\mathbf{w_p} - \mathbf{w_p^*})^\mathbf{T} \mathbf{C}^{-1} (\mathbf{w_p} - \mathbf{w_p^*}) + (n_g - n_g^*)^2 / \sigma_{n_g}^2, \qquad (8)$$

where $\mathbf{w_p}$ and n_g are the vectors of the two-point correlation function and the number density of the sample, and $\mathbf{C}$ is the full covariance matrix. The measured values are denoted with a superscript "$*$".

We implement a Markov Chain Monte Carlo (MCMC) code to explore the HOD parameter space. At each point of the chain, a random walk is taken in the parameter space to generate a new set of HOD parameters. The step-size of the random walk for each parameter is drawn from a Gaussian distribution. The probability to accept the new set of HOD parameters is taken to be 1 if $\chi_{\mathrm{new}}^2 \leqslant \chi_{\mathrm{old}}^2$ and $\exp[-(\chi_{\mathrm{new}}^2 - \chi_{\mathrm{old}}^2)/2]$ if $\chi_{\mathrm{new}}^2 > \chi_{\mathrm{old}}^2$, where χ_{old}^2 and χ_{new}^2 are the values of χ^2 for the old and new models. Flat priors in logarithmic space are adopted for the three parameters related to mass scales, and flat priors in linear space are used for the other two HOD parameters. The length of the chain for each galaxy sample is typically 10,000 and we find convergence by comparing multiple realizations of chains.

Before turning to our observational results, it is worth noting the similarities and differences between HOD modeling and two closely related methods, conditional luminosity functions (CLFs) and subhalo abundance matching (SHAM). Each well-defined class of galaxies, e.g., a luminosity-bin or luminosity-threshold sample, has its own HOD. A CLF (Yang et al. 2003) provides a global model of the full galaxy population, specifying the luminosity function at each halo mass. An HOD can be calculated from a CLF by integrating the latter over luminosity, and a CLF can be calculated from a series of HODs by smoothed differentiation. The virtue of the CLF is its completeness, but when fitting data it typically requires stronger prior assumptions, such as a functional form for the luminosity function itself and functional forms for the dependence of luminosity function parameters on halo mass. By contrast, the five-parameter HOD model used here is already flexible enough to provide a near-perfect description of theoretical model predictions for luminosity-threshold samples (Zheng et al. 2005). The SHAM method (Conroy et al. 2006; Vale & Ostriker 2006) assumes a monotonic relation between the luminosity or stellar mass of a galaxy and the mass or circular velocity of its parent halo or subhalo; the method can be generalized to allow scatter in this relation. While an HOD model takes the space density and clustering of a galaxy population as input for parameter fits, a SHAM model takes only the space density as input and predicts the clustering, effectively using
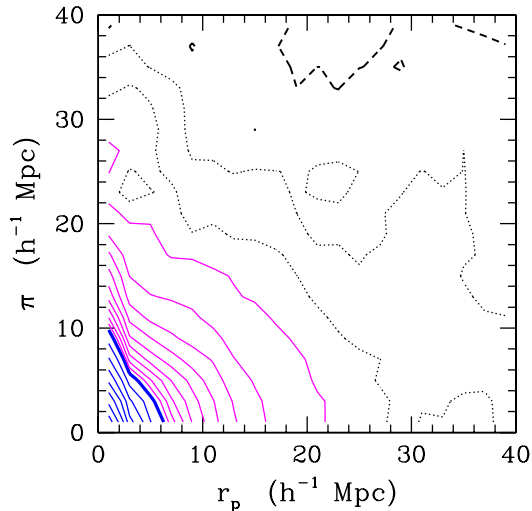
Figure 5. Contours of the galaxy correlation function as a function of tangential separation r_p and line-of-sight separation π, evaluated for the $-20 < M_r < -19$ sample in $2\,h^{-1}$ Mpc bins. The heavy (blue) contour marks $\xi(r_p, \pi) = 1$; inner $\xi > 1$ (blue) contours are spaced by 0.1 in $\log \xi$, and outer $\xi < 1$ (magenta) contours by 0.1 in ξ. The dotted contours denote values of 0.067 and 0.033, while the thick dashed contour marks $\xi(r_p, \pi) = 0$. In the absence of redshift-space distortions, contours would be isotropic. The measured contours show the compression at large scales caused by coherent peculiar velocities and the elongation at small r_p caused by "finger-of-God" distortions in collapsed structures.

(A color version of this figure is available in the online journal.)

a theoretical prior to specify the satellite occupation function. SHAM models are remarkably successful at matching the Z05 correlation functions of luminosity-threshold samples (Conroy et al. 2006).

The correlation functions of sub-L_* galaxies at low redshift are typically well described by power laws on scales $r_p \lesssim 10\,h^{-1}$ Mpc (Totsuji & Kihara 1969; Peebles 1974; Gott & Turner 1979), but deviations from a power law become progressively stronger for brighter galaxies (Zehavi et al. 2004; Z05; this paper) and at higher redshifts (Conroy et al. 2006 and references therein). In the context of HOD models, Watson et al. (2011) discuss the physical processes that lead both to an approximate power-law correlation function and to deviations from a power law (see also Benson et al. 2000; Berlind & Weinberg 2002; and Appendix A of Zheng et al. 2009).

3. DEPENDENCE ON LUMINOSITY

3.1. Clustering Results

We study the clustering dependence on luminosity using sets of volume-limited samples constructed from the full SDSS sample, corresponding to different luminosity bins and thresholds. Details of the individual samples are given in Tables 1 and 2 and illustrated in Figure 4.

As a representative case, we show in Figure 5 the two-dimensional correlation function, $\xi(r_p, \pi)$, as a function of separations perpendicular, r_p, and parallel, π, to the line of sight, calculated for the $-20 < M_r < -19$ sample. In the absence of redshift-space distortions the contours would have been isotropic, a function only of total separation ($\sqrt{r_p{}^2 + \pi^2}$). Redshift-space distortions enter in the line-of-sight direction and are clearly evident in the plot. For small projected separations, the contours are elongated along the line-of-sight direction, reflecting the "fingers-of-God" effect of small-scale virial motions

in collapsed objects. On larger scales, we see the compression caused by coherent large-scale streaming into overdense regions and out of underdense regions (Sargent & Turner 1977; Kaiser 1987).

We isolate real-space correlations by calculating the projected correlation function, $w_p(r_p)$, according to Equation (3). Figure 6 shows the projected correlation functions obtained for the volume-limited samples defined by luminosity bins and by luminosity thresholds. For the luminosity bins, we find a pronounced dependence of clustering on luminosity for the bright samples, with the more luminous galaxies exhibiting higher clustering amplitudes. The dependence on luminosity is more subtle for the fainter luminosity-bin samples, with little change for scales $r_p < 2\,h^{-1}$ Mpc. Behavior for the luminosity thresholds is similar, with nearly identical correlation functions for the $M_r < -18.5$ and < -19.5 samples, a slow but significant increase in clustering strength moving to $M_r < -20.5$ and $M_r < -21.0$, then a rapid increase going to $M_r < -21.5$ and $M_r < -22.0$. Measurements for the luminosity-threshold samples are less noisy, and one can see that the shapes of $w_p(r_p)$ are similar for all samples at $r_p \gtrsim 3\,h^{-1}$ Mpc, while the brighter samples exhibit a stronger inflection in $w_p(r_p)$ at $r_p \approx 2\,h^{-1}$ Mpc and a steeper correlation function at smaller scales. The error covariance matrices exhibit significant correlation between the measurements on different scales, particularly for the relatively faint, smaller volume, galaxy samples. Similar behavior is found by McBride et al. (2011). Power-law fits for these clustering measurements, using the measured data points for $r_p < 20\,h^{-1}$ Mpc, are presented in Tables 1 and 2. We include fits computed both with and without the off-diagonal terms in the covariance matrix (i.e., setting the off-diagonal terms to zero). We caution that when the power-law fit is an inadequate description of the data, as indicated by large $\chi^2/$dof values, the r_0 and γ uncertainties have limited meaning—fitting over different ranges of the data could produce different values of the fit parameters. Tests in Appendix B on the $M_r < -21$ sample show that changes to our analysis procedures cause r_0 and γ changes that are smaller than (or at most comparable to) the statistical error bars.

At large scales, we expect the real-space galaxy correlation function to be a scale-independent multiple of the dark matter correlation function $\xi_{gg}(r) = b_g^2 \xi_{mm}(r)$, where the bias factor b_g will differ from one class of galaxies to another. For each sample, we calculate the best-fitting bias factor of the measured $w_p(r_p)$ with respect to the $z = 0.1$ dark matter $w_p(r_p)$ over the separation range $4\,h^{-1}$ Mpc $< r_p < 30\,h^{-1}$ Mpc, using the full error covariance matrix of the measurements. (The average of r_p weighted by the inverse of the uncertainty in w_p corresponds to a separation of $\sim 8\,h^{-1}$ Mpc, which can be regarded as a rough estimate of the effective radius for this fit.) The $w_p(r_p)$ predicted for the nonlinear *matter* distribution of our ΛCDM cosmological model is computed from the nonlinear power spectrum with the method of Smith et al. 2003. Filled circles in Figure 7 show these bias factors $b_g(L)$ and $b_g(>L)$ for our luminosity-bin and luminosity-threshold samples. We refer to these below as "DM-ratio" bias factors. In Z05, we defined bias factors via the value of $w_p(r_p)$ at one representative separation, $r_p = 2.67\,h^{-1}$ Mpc. Open triangles in Figure 7 show this measurement of "single-r_p" bias factors for comparison. For the $-21 < M_r < -20$ bin and the $M_r < -20$ and $M_r < -19.5$ thresholds, we use the samples with $cz_{\max} = 19{,}250\,{\rm km\,s}^{-1}$ (see Tables 1 and 2), for the reasons discussed in Section 3.2 below. Because $b_g(L)$ changes so rapidly between $M_r = -21$ and
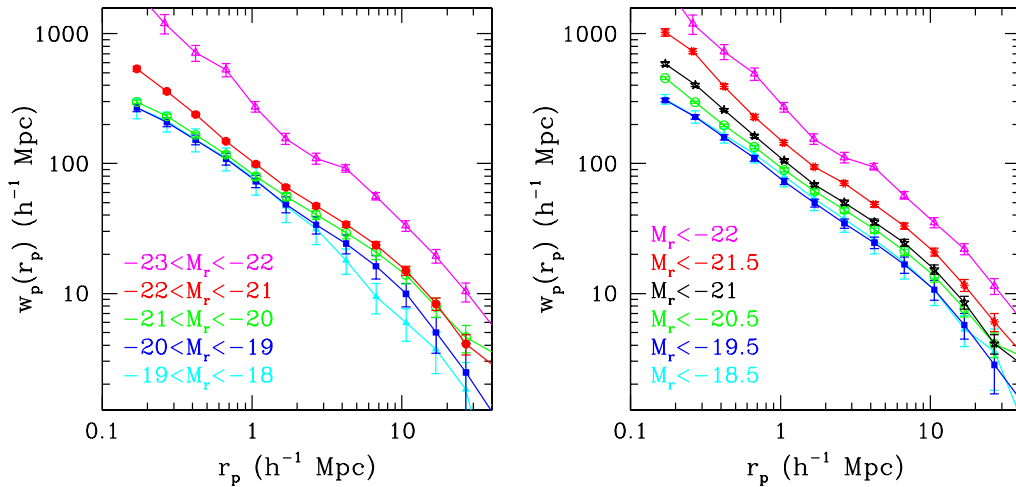
Figure 6. Projected correlation functions for volume-limited samples corresponding to different luminosity-bin samples (left) and luminosity-threshold samples (right), as labeled. Error covariance matrices are computed from jackknife resampling as described in the text. The error bars shown are the square root of the diagonal elements of these matrices. For visual clarity, only a subset of the threshold samples is plotted.
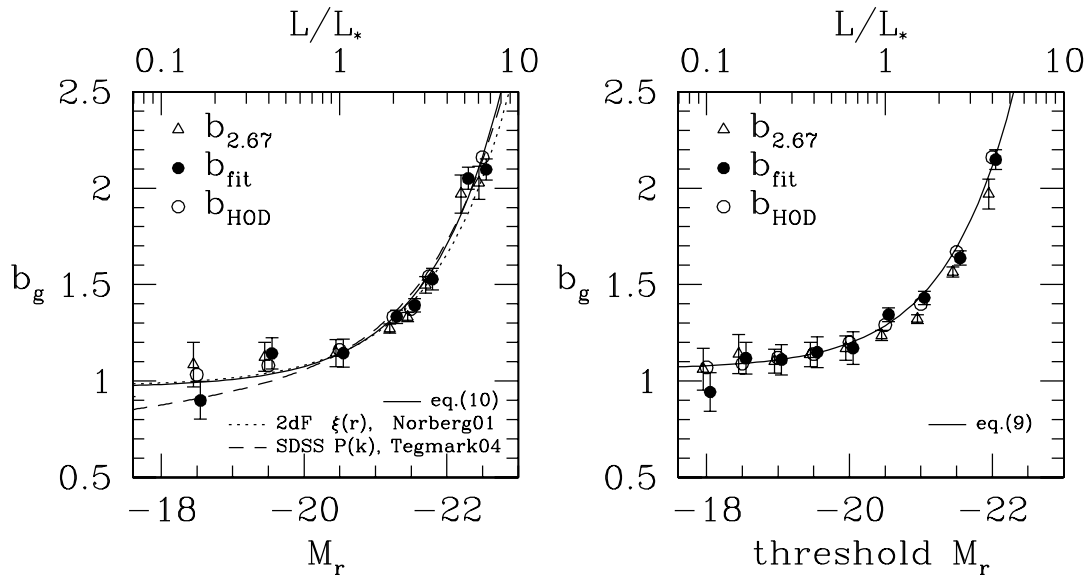
(A color version of this figure is available in the online journal.)

Figure 7. Bias factors for the luminosity-bin samples (left) and the luminosity-threshold samples (right). Filled circles show bias factors defined by the ratio of the measured $w_p(r_p)$ to the dark matter $w_p(r_p)$ predicted for our fiducial cosmological model over the range $4 \, h^{-1}$ Mpc $\leqslant r_p \leqslant 30 \, h^{-1}$ Mpc. Open triangles show the bias factors defined by this ratio for the single radial bin centered at $r_p = 2.67 \, h^{-1}$ Mpc, as done previously by Z05. In addition to the luminosity-bin samples shown in Figure 6, the left panel includes $b_g(L)$ points for the half-magnitude bins $-21.5 < M_r < -21.0$ and $-22.0 < M_r < -21.5$. Open circles show the bias factors inferred from HOD modeling as described in Section 3.3; the statistical errors on these estimates are smaller than the points, and we omit them for visual clarity. In the left panel, the dotted curve is a fit to projected correlation functions in the 2dFGRS, $b_g/b_* = 0.85 + 0.15 L/L_*$ (Norberg et al. 2001), where we take $b_* \equiv b_g(L_*) = 1.14$ to be the bias factor inferred from the dark-matter-ratio estimate in the $-21 < M_r < -20$ luminosity bin ($L \approx L_*$, defined to correspond to $M_r = -20.5$ here), and the dashed curve is a modified fit to SDSS power spectrum measurements, $b_g/b_* = 0.85 + 0.15 L/L_* - 0.04(M - M_*)$ (Tegmark et al. 2004). The solid curve is the fit in Equation (10). In the right panel, the solid curve is the fit to the HOD model bias factors, Equation (9). The points locations on the magnitude axis correspond to the bin center (left) and threshold magnitude (right). Small horizontal offsets have been added to points for clarity.

$M_r = -22$, we have also divided the $-22 < M_r < -21$ bin into two half-magnitude bins and computed bias factors separately for each. The open circles, discussed further in Section 3.3, show large-scale bias factors derived from HOD model fits to the full projected correlation functions ("HOD bias factors"; computed at the mean redshift of each sample).

In agreement with previous studies (Norberg et al. 2001; Tegmark et al. 2004; Z05), $b_g(L)$ is nearly flat for luminosities $L \leqslant L_*$, then rises sharply at brighter luminosities.[16]

Dotted and dashed curves in the left panel show the empirical fits to $b_g(L)/b_g(L_*)$ proposed by Norberg et al. (2001) and Tegmark et al. (2004), respectively, where we take as $b_g(L_*)$ the "DM-ratio" bias factor estimated for the $-21 < M_r < -20$ luminosity bin using the large-scale $w_p(r_p)$ ratio. The Norberg et al. (2001) form appears to fit our measurements better, but the differences between the curves only become large for the $-18.0 < M_r < -19.0$ sample, where the single-r_p and DM-ratio bias factors differ noticeably, and where the tests discussed in Section 3.2 below suggest that cosmic variance fluctuations are still significant. The HOD bias factors are in good agreement with the "DM-ratio" ones.
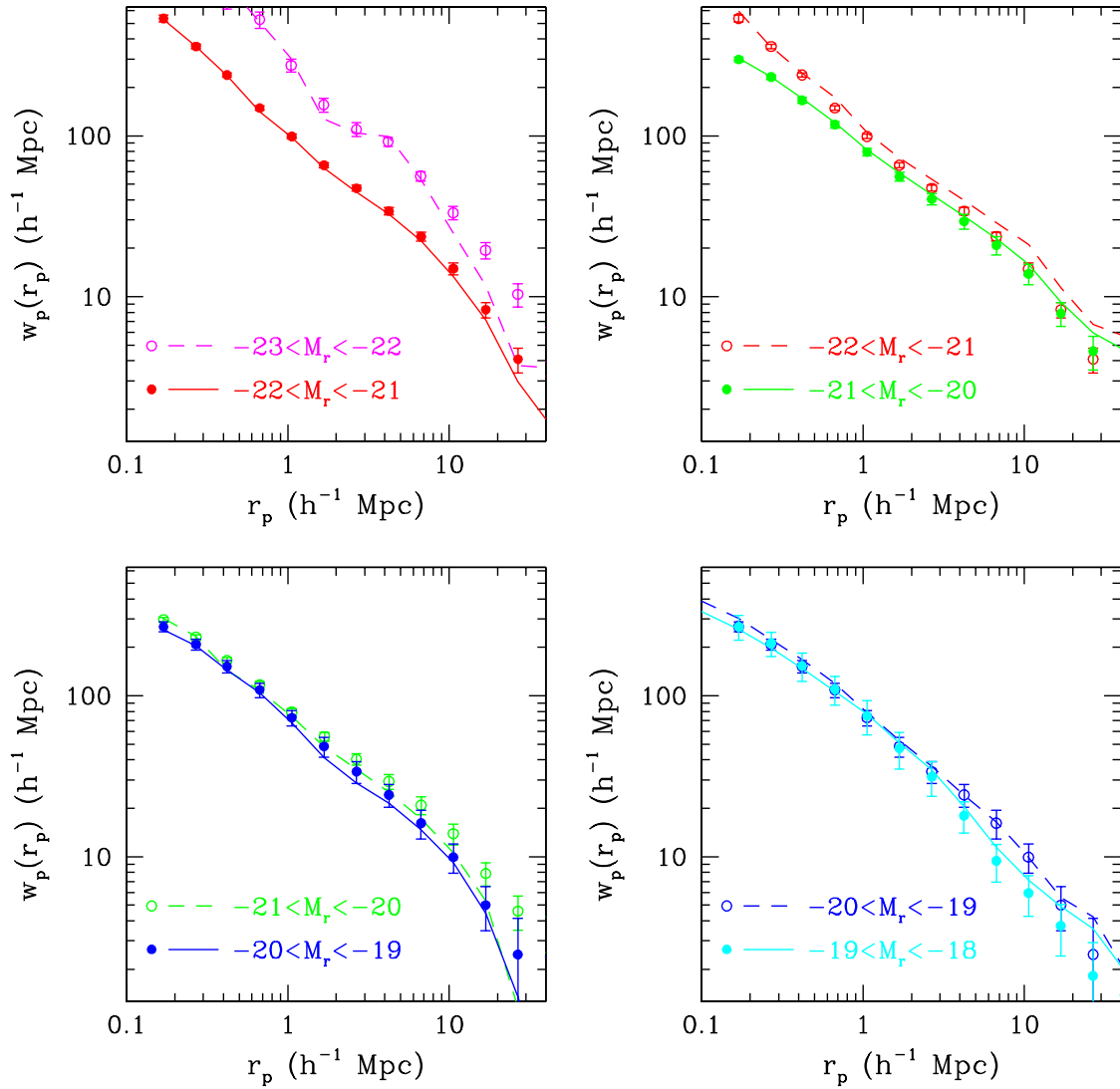
---

[16] For the Blanton et al. (2003c) luminosity function, the characteristic luminosity L_* of the Schechter (1976) luminosity function fit corresponds to $M_r = -20.44$.

Figure 8. Check of finite-volume effects ("cosmic variance") in the measured luminosity dependence of the correlation function. Each panel shows projected correlation functions of two adjacent luminosity bins in their full volume-limited range (symbols with error bars) and in their common overlap regions (lines). The solid line and filled symbols correspond to the fainter luminosity bin in each panel, while the dashed line and open symbols correspond to the brighter sample. Comparison of the dashed and solid lines in each panel tests for luminosity segregation between the two adjacent bins measured in a common volume.

(A color version of this figure is available in the online journal.)

The luminosity-threshold samples allow more precise bias measurements, and they avoid binning effects that can influence the estimates of $b(L)$ when it changes rapidly across a bin. The HOD and DM-ratio values of $b_g(>L)$ agree well for all luminosity-threshold samples except $M_r < -18.0$, where the HOD fit overpredicts the large-scale $w_p(r_p)$ measurements (see Figure 10 below). The HOD bias points are fit to 3% or better by the functional form

$$b_g(>L) \times (\sigma_8/0.8) = 1.06 + 0.21(L/L_*)^{1.12}, \qquad (9)$$

where L is the r-band luminosity corrected to $z = 0.1$ and L_* corresponds to $M_r = -20.44$ (Blanton et al. 2003c). Except for the $M_r < -18$ point, this formula also accurately describes the DM-ratio bias factors. The HOD and DM-ratio bias factors scale as σ_8^{-1} to a near-perfect approximation, since at large scales $\xi_{gg} = b_g^2 \xi_{mm} \propto b_g^2 \sigma_8^2$. We consider Equation (9) to be our most robust estimate of the dependence of large-scale bias on galaxy luminosity, applicable over the range $0.16 L_* < L < 6.3 L_*$ ($-22.5 < M_r < -18.5$). Fitting the DM-ratio bias values for

the luminosity-bin samples yields

$$b_g(L) \times (\sigma_8/0.8) = 0.97 + 0.17(L/L_*)^{1.04}, \qquad (10)$$

which is close to the formula derived by Norberg et al. (2001) for b_J-selected galaxies, but has a slightly steeper rise at high luminosities.

3.2. Tests of Cosmic Variance

Our volume-limited, luminosity-bin samples span different ranges in redshift (specified in Table 1), with intrinsically brighter galaxies observed over larger volumes. It is thus important to test for the robustness of the detected luminosity dependence to "cosmic variance" of the structure in these different volumes. (We follow common practice in referring to these finite-volume effects as cosmic variance, though a more precise term would be "sample variance"; Scott et al. 1994.) Figure 8 compares projected correlation functions of adjacent luminosity bins when using their respective full volume-limited redshift range (points with error bars) and when restricting both

to their common overlap range (lines). The overlap volume is similar to the full volume of the fainter sample (differing only because of the $r > 14.5$ bright limit), so the filled points and solid lines are usually in close agreement.

The most significant cosmic variance effect on the measurements appears to be due to the Sloan Great Wall (SGW), a huge supercluster at $z \sim 0.08$, which is the largest coherent structure detected in the SDSS (Figure 2; see also Gott et al. 2005). Its distance places it right at the edge of the $-21 < M_r < -20$ sample (see Table 1). Its exclusion from this sample when limiting to the overlap range with the $-20 < M_r < -19$ sample causes the decrease in clustering amplitude on large scales seen in the bottom left panel. Hence, this structure also causes the flattening in the projected correlation function of this sample at large separations seen in Figure 6. Conversely, restricting the brighter $-22 < M_r < -21$ sample to the smaller overlap range accentuates the supercluster's dominance and gives rise to the increased clustering seen in the top right panel (dashed line). Taken together, these results strongly suggest that the most reliable estimate of $w_p(r_p)$ for the $-21 < M_r < -20$ luminosity bin comes from the SGW-excluded sample rather than the full sample. Brighter, larger volume samples are much less affected by the SGW, while fainter samples do not extend as far and are thus not affected. These results are very similar to those of an identical test performed with the smaller samples of Z05.

We have performed similar tests with the luminosity-threshold samples, and we find an analogous effect of the SGW, mostly for the $M_r < -20$ sample and, to a lesser degree, for the $M_r < -19.5$ sample. We have also done tests where we have excluded specifically the SGW region with angular and redshift cuts, confirming its significant impact on the large-scale clustering measurement for these samples. It is striking that even with the full SDSS sample, the effect of the SGW is still significant, and one should use caution in interpreting clustering measurements for relatively large separations ($r_p > 5\,h^{-1}$ Mpc) for the few specific samples whose redshift range extends just up to (and including) this structure. For this reason, in Tables 1 and 2, we also provide power-law fits of these samples when restricted to a redshift limit that excludes the SGW ($cz_{max} = 19,250$ km s^{-1}, the same limiting redshift as for the $-20 < M_r < -19$ and the $M_r < -19$ samples). The HOD parameters derived for these samples are relatively insensitive to the choice of sample volume, and the correlation functions corresponding to these HOD models differ much less than the power-law fits (see, e.g., Figure 15 in Z05). This insensitivity reflects the constrained nature of HOD fits for a specified cosmological model: there is little freedom within these fits to adjust the large-scale correlation amplitude relative to the more robust measurements at $r_p < 2\,h^{-1}$ Mpc, so the HOD modeling just accepts the χ^2 penalty of missing the large-scale data points.

Other large structures in the survey volume may affect the clustering measurements in more subtle ways. McBride et al. (2011) investigated the impact of such structures on the three-point correlation function by analyzing the residuals of individual jackknife samples. The two-point correlation function is much less sensitive to such effects, with individual deviations at the few percent level at most scales (C. K. McBride 2011, private communication). Of course, it is the cumulative impact of these residuals that determines the jackknife error bars, so the fact that they exist does not in itself imply that errors are larger than our estimates. The tests of Z05 and Norberg et al. (2009) suggest that jackknife error estimates for $w_p(r_p)$ are typically accurate or conservative (see
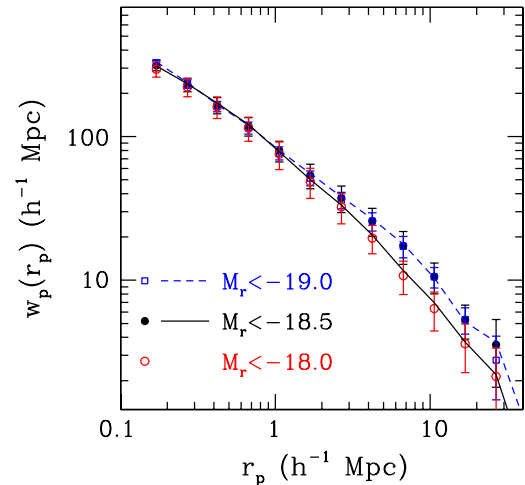

Figure 9. Check of finite-volume effects in the nearby low-luminosity-threshold samples. The plot shows the projected correlation functions of the three faintest threshold samples in their full volume-limited range (symbols with error bars) and limited to the smaller overlap region of the adjacent fainter sample (lines). When limiting the $M_r < -18.5$ sample (or brighter ones) to the volume of the $M_r < -18$ sample (solid black line), the correlation function changes significantly and agrees with the latter measurement, while no such effect is detected when limiting the $M_r < -19$ (or brighter samples) measurements to the volume of the $M_r < -18.5$ sample (dashed blue line).

(A color version of this figure is available in the online journal.)

Section 2.2). An investigation of the individual residuals also suggests that the jackknife errors follow a Gaussian distribution to a fair approximation, but with some noticeable skewness (C. K. McBride 2011, private communication; see also Norberg et al. 2011). However, we find only a small difference between measuring $w_p(r_p)$ from the full data sample and taking the median of the jackknife $w_p(r_p)$ values in each separation bin, which suggests that any non-Gaussianity will have minimal impact on our clustering results.

Additional cosmic variance concerns have to do with the relatively small volumes associated with the lowest luminosity samples we consider. Figure 8 can shed some light on this issue as well. Specifically, the bottom-right panel checks the sensitivity to the volume probed in the correlation functions measured for the $-19 < M_r < -18$ and $-20 < M_r < -19$ luminosity bins. The general agreement of the curves (calculated in the overlap volume) to the respective sets of points (calculated for the full volume-limited sample), within the measured uncertainties, is reassuring. We perform similar tests with the magnitude-threshold samples, looking at the robustness of the clustering measurements of different samples when limiting to the inner small volumes associated with the fainter thresholds. Here, we find substantial volume effects when considering the volume of the faintest threshold sample $M_r < -18$, but very weakened effects for the $M_r < -18.5$ and brighter thresholds (see Figure 9). We are unsure why the effects for the $M_r < -18.0$ sample appear larger than those for the $-19.0 < M_r < -18.0$ luminosity-bin sample, as they have the same outer redshift limit; however, the galaxy populations are different in the two cases, with the luminosity-threshold sample including also brighter galaxies. We find these finite-volume effects to be smaller than those found in the earlier samples of Z05, due to the larger sky coverage of SDSS DR7.

The comparisons of solid and dashed curves in Figure 8 provide the fairest test of luminosity dependence between the samples, as the effects of cosmic variance are essentially
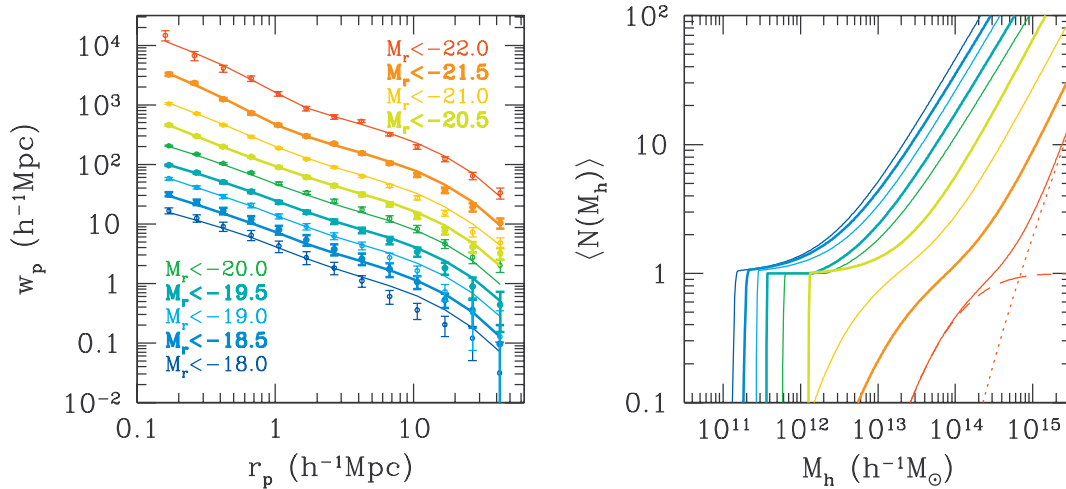
Figure 10. Luminosity dependence of galaxy clustering and the HOD. The left panel shows the measured $w_p(r_p)$ and the best-fit HOD models for all luminosity-threshold samples. The samples are each staggered by 0.25 dex, starting from the $M_r < -20.5$ sample, for clarity. The right panel shows the corresponding halo occupation functions, $\langle N(M_h) \rangle$, color-coded in the same way. The occupation functions shift to the right, toward more massive halos, as the luminosity threshold increases. The separation of central and satellite galaxies is shown for the rightmost occupation function, corresponding to the brightest sample, as the dashed and dotted curves, respectively. For the six fainter samples, we have chosen models with sharp central galaxy cutoffs ($\sigma_{\log M} \approx 0$) that have $\Delta\chi^2 < 1$ relative to the best-fit model listed in Table 3 (see the text). The three brightest samples *require* smooth cutoff profiles to fit the number density and clustering data.

(A color version of this figure is available in the online journal.)

Table 3
HOD and Derived Parameters for Luminosity-threshold Samples

M_r^{max}	$\log M_{min}$	$\sigma_{\log M}$	$\log M_0$	$\log M_1'$	α	$\log M_1$	f_{sat}	b_g	$\frac{\chi^2}{dof}$
−22.0	14.06 ± 0.06	0.71 ± 0.07	13.72 ± 0.53	14.80 ± 0.08	1.35 ± 0.49	14.85 ± 0.04	0.04 ± 0.01	2.16 ± 0.05	1.8
−21.5	13.38 ± 0.07	0.69 ± 0.08	13.35 ± 0.21	14.20 ± 0.07	1.09 ± 0.17	14.29 ± 0.04	0.09 ± 0.01	1.67 ± 0.03	2.3
−21.0	12.78 ± 0.10	0.68 ± 0.15	12.71 ± 0.26	13.76 ± 0.05	1.15 ± 0.06	13.80 ± 0.03	0.15 ± 0.01	1.40 ± 0.03	3.1
−20.5	12.14 ± 0.03	0.17 ± 0.15	11.62 ± 0.72	13.43 ± 0.04	1.15 ± 0.03	13.44 ± 0.03	0.20 ± 0.01	1.29 ± 0.01	2.7
−20.0	11.83 ± 0.03	0.25 ± 0.11	12.35 ± 0.24	12.98 ± 0.07	1.00 ± 0.05	13.08 ± 0.03	0.22 ± 0.01	1.20 ± 0.01	2.1
−19.5	11.57 ± 0.04	0.17 ± 0.13	12.23 ± 0.17	12.75 ± 0.07	0.99 ± 0.04	12.87 ± 0.03	0.23 ± 0.01	1.14 ± 0.01	1.0
−19.0	11.45 ± 0.04	0.19 ± 0.13	9.77 ± 1.41	12.63 ± 0.04	1.02 ± 0.02	12.64 ± 0.04	0.33 ± 0.01	1.12 ± 0.01	1.8
−18.5	11.33 ± 0.07	0.26 ± 0.21	8.99 ± 1.33	12.50 ± 0.04	1.02 ± 0.03	12.51 ± 0.04	0.34 ± 0.02	1.09 ± 0.01	0.9
−18.0	11.18 ± 0.04	0.19 ± 0.17	9.81 ± 0.62	12.42 ± 0.05	1.04 ± 0.04	12.43 ± 0.05	0.32 ± 0.02	1.07 ± 0.01	1.4

Notes. See Equation (7) for the HOD parameterization. Halo mass is in units of $h^{-1} M_\odot$. Error bars on the HOD parameters correspond to 1σ, derived from the marginalized distributions. M_1, f_{sat}, and b_g are derived parameters from the fits. M_1 is the mass scale of a halo that can on average host one satellite galaxy above the luminosity threshold and f_{sat} is the fraction of satellite galaxies in the sample. b_g is the large-scale galaxy bias factor and is degenerate with the amplitude of matter clustering σ_8, so that this is in fact $b_g \times (\sigma_8/0.8)$. A 2% systematic shift in the w_p values would correspond to a 1% change in b_g, effectively doubling the tiny error bars on it. For all samples, the number of degrees of freedom (dof) is 9 (13 measured w_p values plus the number density minus the five fitted parameters). The parameters of the sharp-cutoff models plotted in Figure 10 for the six fainter samples (see the text) are specified hereby as (M_r^{max}, $\log M_{min}$, $\sigma_{\log M}$, $\log M_0$, $\log M_1'$, α): (−18.0, 11.14, 0.02, 9.84, 12.40, 1.04); (−18.5, 11.29, 0.03, 9.64, 12.48, 1.01); (−19.0, 11.44, 0.01, 10.31, 12.64, 1.03); (−19.5, 11.56, 0.003, 12.15, 12.79, 1.01); (−20.0, 11.78, 0.02, 12.32, 12.98, 1.01); (−20.5, 12.11, 0.01, 11.86, 13.41, 1.13).

removed by matching volumes. For the fainter samples shown in the lower panels, the evidence for luminosity dependence is marginal relative to the error bars. The detection is stronger in the upper right panel and overwhelming for the brightest galaxies in the upper left. The difference between the dashed line and the open points in this panel is plausibly explained by the small sample ($\sim$2600 galaxies) of $-23 < M_r < -22$ galaxies in the overlap volume: the larger volume of the full sample is required to give a robust measurement of large-scale clustering for these rare galaxies. These conclusions—evidence for increased clustering at $M_r \approx -21.5$ and dramatically increased clustering at $M_r \approx -22.5$—are consistent with the $b(L)$ data points in Figure 7.

3.3. Modeling the Luminosity Dependence

To investigate further the implications of the luminosity-dependent clustering, we turn to HOD modeling. We find the best-fit HOD models for our set of volume-limited luminosity-threshold samples, using the five-parameter model described in Section 2.3. Figure 10 shows the HOD best fits to the projected correlation functions (staggered by 0.25 dex for clarity). Here, we use the full volume-limited samples, with no attempt to remove the SGW. The values of the fitted parameters, inferred using the full error covariance matrix, are given in Table 3. We also list f_{sat}, the fraction of sample galaxies that are satellites from the HOD modeling results. We see that the HOD models provide reasonable fits to the projected correlation functions, with deviations from a power law more apparent for the brighter samples. The characteristic inflections in $w_p(r_p)$ at $r_p = 1$–$2\,h^{-1}$ Mpc arise at the transition from the small-scale, one-halo regime, where most correlated pairs come from galaxies in the same halo, to the large-scale, two-halo regime, where the shape of $\xi(r)$ approximately traces the shape of the matter correlation function (Berlind & Weinberg 2002; Zehavi
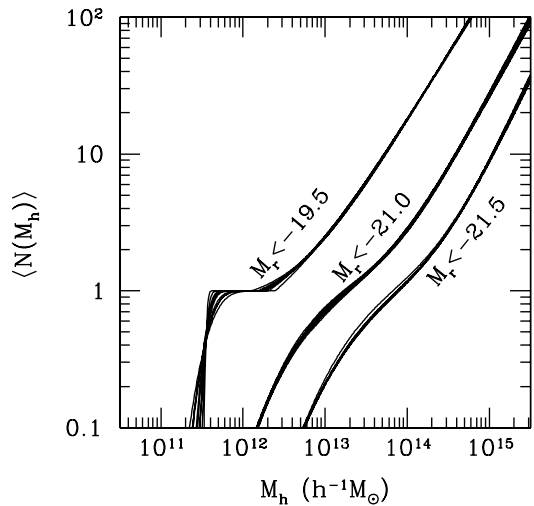
Figure 11. Uncertainties in the HOD fits for the $M_r < -19.5$, -21.0, and -21.5 luminosity-threshold samples (left to right). For each model, the figure shows $\langle N(M_h) \rangle$ for 10 randomly selected models that have $\Delta\chi^2 < 1$ relative to the best-fit model.

et al. 2004). The χ^2 values for these fits are also specified in the table and can be compared to the corresponding values for the power-law fits (Table 2). In all cases the HOD model has a better goodness of fit than the best-fit power-law model. We note, however, that the χ^2 values still tend to be somewhat large, particularly for the bright samples. These might reflect uncertainties in the jackknife error covariance estimate, residual systematics or a limitation of the restricted HOD model. For the $M_r < -18.0$ sample, the HOD model overpredicts the amplitude of $w_p(r_p)$ at large scales, but the tests in Figure 9 suggest that the large-scale clustering of this sample is significantly affected by the small sample volume.

The high-mass slope α of the satellite mean occupation function is around unity for most samples. For the brightest sample ($M_r < -22.0$), α is noticeably higher than unity, but with large error bars. The right panel of Figure 10 presents the halo occupation functions themselves. When going toward brighter samples, the main effect is a shift of the halo occupation function toward higher halo masses, a shift that affects both

the central galaxy cutoff and the satellite occupation. More luminous galaxies occupy more massive halos, which leads to their stronger clustering. For the six fainter samples, there are models with sharp central galaxy cutoffs ($\sigma_{\log M} = 0$) that have $\Delta\chi^2 < 1$ compared to the best-fit model; we have chosen to plot these sharp-cutoff $\langle N(M_h) \rangle$ curves in Figure 10. For the $M_r < -21.0$, $M_r < -21.5$, and $M_r < -22.0$ samples, however, a non-zero value of $\sigma_{\log M}$, indicating scatter between halo mass and central galaxy luminosity, is required to simultaneously fit the galaxy number density and projected correlation function. A sharper cutoff would predict an excessive clustering amplitude for the measured number density because of the rising $b(M_h)$ relation. Figure 11 illustrates the level of statistical uncertainty in the HOD fits, plotting $\langle N(M_h) \rangle$ for ten models randomly chosen from the MCMC chain that have $\Delta\chi^2 < 1$ relative to the best-fit model for each of three luminosity thresholds. The cutoff profile is generally better constrained for brighter samples because of the steeper form of $b(M_h)$ at high M_h. The satellite occupations are tightly constrained in all cases (other than a relatively large scatter in M_0 for the $M_r < -20.5$ sample).

Figure 12(a) shows the two characteristic halo mass parameters $M_{\min}$ and M_1 (see Section 2.3) as a function of the threshold luminosity. Both halo mass scales increase with the sample's threshold luminosity, with a steeper dependence for brighter galaxies. Because central galaxies dominate the total number density for any luminosity threshold (Zheng et al. 2005), the approximate form of the $M_{\min}$ curve follows simply from matching the space densities of galaxies and halos (e.g., Conroy et al. 2006; Vale & Ostriker 2006). In our HOD parameterization, $M_{\min}$ can be interpreted as the mass of halos in which the median luminosity of central galaxies is equal to the threshold luminosity. We propose the following form for the relation between median central galaxy luminosity L_{cen} and halo mass M_h (see also Kim et al. 2008),

$$L_{cen}/L_* = A\left(\frac{M_h}{M_t}\right)^{\alpha_M} \exp\left(-\frac{M_t}{M_h} + 1\right), \qquad (11)$$

where A, M_t, and α_M are three free parameters. That is, the median central galaxy luminosity has a power-law dependence
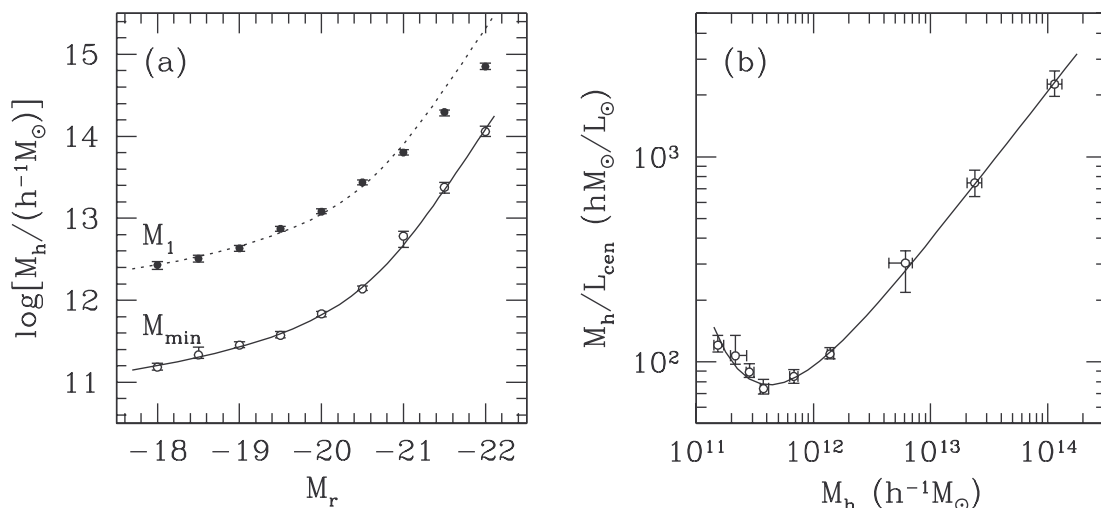

Figure 12. Panel (a): characteristic mass scales of halos hosting central galaxies and satellites as a function of the sample threshold luminosity. Open symbols show the $M_{\min}$ values, while filled symbols are the M_1 values. The solid curve is a simple parameterized fit to $M_{\min}$ as a function of threshold luminosity (Equation (11)). The dotted curve denotes the solid curve scaled up by a factor of 17, representing the $M_1 \approx 17M_{\min}$ scaling relation. Panel (b): ratio of halo mass to median central galaxy luminosity as a function of halo mass. The solid curve is derived from the fit in panel (a) (see Equation (12)).

on halo mass at the high-mass end (with a power-law index of α_M) and drops exponentially at the low-mass end. The transition halo mass is characterized by M_t, and the normalization factor A is the median luminosity of central galaxies (in units of $L_* = 1.20 \times 10^{10} h^{-2} L_\odot$ in the r band; Blanton et al. 2003c) in halos of transition mass. The fit (solid curve) shown in Figure 12(a) has $A = 0.32$, $M_t = 3.08 \times 10^{11} h^{-1} M_\odot$, and $\alpha_M = 0.264$. Figure 12(b) shows the $M_h/L_{\rm cen}$ ratio as a function of halo mass. The solid curve is derived from the fit in Figure 12(a):

$$\frac{M_h}{L_{\rm cen}} = \left(\frac{M_h}{L_{\rm cen}}\right)_{M_t} \left(\frac{M_h}{M_t}\right)^{1-\alpha_M} \exp\left(\frac{M_t}{M_h} - 1\right), \qquad (12)$$

where $(M_h/L_{\rm cen})_{M_t} = 80 h\, M_\odot/L_\odot$ is the mass-to-light ratio in halos of transition mass. The transition mass (times $1/(1 - \alpha_M)$, to be exact) also marks the scale at which $M_h/L_{\rm cen}$ reaches a minimum. Halos of $M_h \approx 4.2 \times 10^{11}\, h^{-1}\, M_\odot$ are maximally efficient at converting their available baryons into r-band light of their central galaxy. Other authors have reached a similar conclusion using HOD, CLF, or SHAM methods (e.g., Yang et al. 2003; Tinker et al. 2005; Vale & Ostriker 2006; Zheng et al. 2007; Kim et al. 2008; Guo et al. 2010; Moster et al. 2010).

In Figure 12(a), the sharp upturn in M_h ($M_{\rm min}$) arises because the galaxy luminosity function drops exponentially in a regime where the halo mass function remains close to a power law. The sharp rise in $b(L)$ (Figure 7) is driven both by this upturn in M_h ($M_{\rm min}$) and by the steepening of the $b(M_h)$ relation itself (Mo & White 1996; Jing 1998; Sheth et al. 2001; Tinker et al. 2010). As discussed by Zheng et al. (2009, Appendix A), the greater departures from a power law $w_p(r_p)$ evident for brighter galaxies arise mainly because $M_{\rm min}$ and M_1 are larger than the characteristic halo mass M_h^* where the halo mass function begins to drop exponentially; this change in the halo mass function shape leads to a sharper transition between the one-halo and two-halo regimes of the correlation function.

There is a considerable gap between the values of $M_{\rm min}$ and M_1 at all luminosities. As in earlier works, we find an approximate scaling relation of $M_1 \approx 17 M_{\rm min}$, implying that a halo hosting two galaxies (one central galaxy and one satellite) above the luminosity threshold has to be about 17 times more massive on average than a halo hosting only one (central) galaxy above the luminosity threshold. Halos in this "hosting gap" mass range tend to host more luminous (higher mass) central galaxies rather than multiple galaxies, consistent with the predictions of Berlind et al. (2003) based on hydrodynamic simulations and semianalytic models. As can be seen in Figure 12(a), this scaling factor is somewhat smaller at the high-luminosity end, corresponding to massive halos that host rich groups or clusters. This latter trend likely reflects the relatively late formation of these massive halos, which leaves less time for satellites to merge onto central galaxies and thus lowers the satellite threshold M_1. Physical effects that shape the $M_1/M_{\rm min}$ relation are discussed by Zentner et al. (2005) using analytic descriptions of halo and galaxy merger rates.

Our results are consistent with previous measurements of these trends (Z05; Zheng et al. 2007). Z05 found a slightly larger scale factor of ≈ 23, likely because of slight differences in the HOD parameterizations and the corresponding definitions of the halo mass scales. Zheng et al. (2007) found, for that same early SDSS sample but using the current HOD model, $M_1 \approx 18 M_{\rm min}$, in excellent agreement with our results for the

final SDSS sample. These results are also in agreement with predictions of galaxy formation models. In particular, the scale factor in the $M_{\rm min} - M_1$ scaling relation is in good agreement with the predictions presented by Zheng et al. (2005).

Returning to Figure 7, open circles in the right-hand panel show the values of $b_g(>L)$ corresponding to our best-fit HOD models, i.e., the asymptotic bias on large scales where the bias factor is scale independent. These bias estimates necessarily depend on the assumptions associated with our HOD modeling, principally that $\langle N(M_h)\rangle$ has the form defined by Equation (7) and that $\langle N(M_h)\rangle$ is independent of a halo's large-scale environment (no "assembly bias"). These assumptions allow us to use constraints from smaller scale clustering and the galaxy number density, greatly reducing the error bars on $b_g(>L)$ and reducing the sensitivity to cosmic variance in the large-scale clustering. Given the significant finite-volume variations that remain even in SDSS DR7 (Section 3.2), we consider these HOD-based $b_g(>L)$ values to be our most robust estimates of the luminosity dependence of galaxy bias, despite their dependence on an assumed model.

To obtain HOD-based bias factors for luminosity-bin samples, we have taken the central and satellite occupation functions for each bin to be simply the difference of the occupation functions for the bracketing threshold samples, yielding the open circles in the left panel of Figure 7. The right panel of Figure 13 shows the resulting mean occupation functions, and the left panel compares the $w_p(r_p)$ predicted by these threshold-difference HODs to the observed $w_p(r_p)$ from Figure 6. After fitting the luminosity-threshold correlation functions, there are no parameter adjustments made to fit the luminosity-bin data. The agreement is generally good. For the faintest luminosity bin $-19 < M_r < -18$ on large scales, the model slightly overpredicts the observed $w_p(r_p)$ (with $\chi^2 = 20$ for 13 data points). This tension could indicate that our HOD model does not allow a good description of galaxies in this luminosity range, or it could be that our jackknife method underestimates the cosmic variance uncertainties for this small-volume sample. We have already noted that the HOD model of the bracketing $M_r < -18.0$ sample overpredicts its observed large-scale clustering (Figure 10), and that this sample appears to have significant finite-volume effects (Figure 9). We revisit this overprediction in Section 4.5 below, where we separately examine the clustering of red and blue galaxies in this luminosity bin.

4. DEPENDENCE ON COLOR

4.1. Autocorrelation of Blue and Red Galaxies

The clustering of galaxies is known to depend on other galaxy properties in addition to luminosity, such as color, surface brightness, and profile shapes. These latter quantities are correlated with each other and produce similar trends in $w_p(r_p)$ (e.g., Zehavi et al. 2002). Moreover, galaxy luminosity and color have been shown to be the two properties most predictive of galaxy environment (Blanton et al. 2005a), such that any residual dependence on morphology or surface brightness at fixed luminosity and color is weak. We focus in this section on the color dependence of galaxy clustering using our luminosity-bin samples. Figure 2 qualitatively illustrated the clustering differences between blue and red galaxies. To study this difference quantitatively, we divide our sample into "blue" and "red" galaxies according to the well-known color bimodality in the color–magnitude plane (e.g., Strateva et al. 2001; Baldry et al. 2004). Following Z05, we use a magnitude-dependent color cut
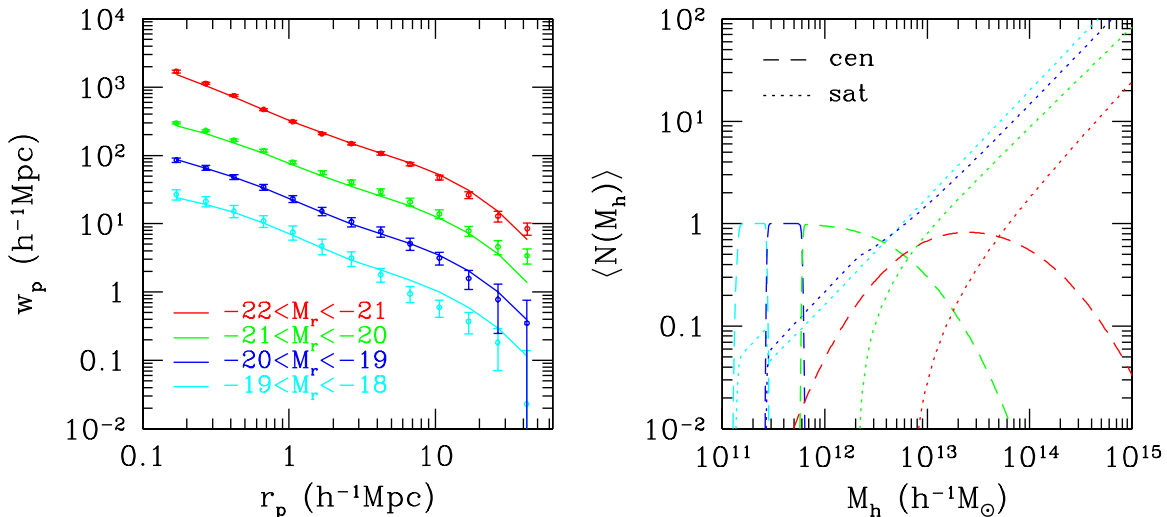
Figure 13. HOD models and predictions for the projected correlation function of luminosity-bin samples. The HOD for each bin is set to the difference of the HODs for the bracketing luminosity thresholds (see Figure 10), with no further adjustments to fit the luminosity-bin data. The right panel shows $\langle N(M_h) \rangle$ separately for the central (dashed lines) and satellite (dotted lines) galaxies. The left panel shows the corresponding model predictions together with the $w_p(r_p)$ data from Figure 6. The samples are each staggered by 0.5 dex, starting from the $-21 < M_r < -20$ sample, for clarity.
(A color version of this figure is available in the online journal.)
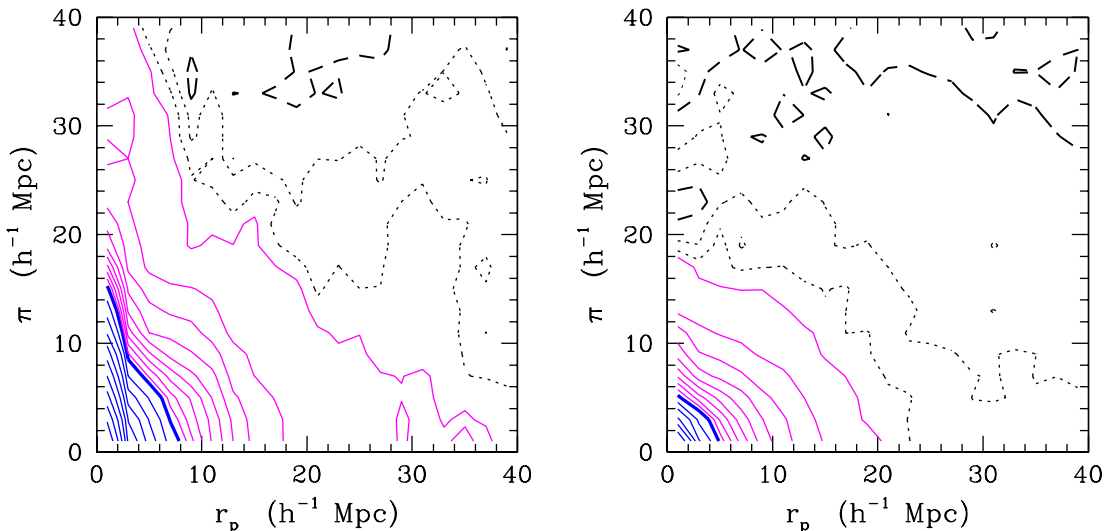
Figure 14. Contours of the galaxy correlation function as a function of tangential separation r_p and line-of-sight separation π for the $-20 < M_r < -19$ sample, evaluated separately for red galaxies (left) and blue galaxies (right). Contours are the same as in Figure 5.
(A color version of this figure is available in the online journal.)

defined by

$$(g - r)_{\text{cut}} = 0.21 - 0.03 M_r. \qquad (13)$$

This tilted cut, shown below in Figure 18, appropriately separates the red E/S0 ridgeline from the blue cloud, following the division into two populations as a function of luminosity. An identical color cut is used by Swanson et al. (2008) and McBride et al. (2011), while other works (e.g., Blanton & Berlind 2007; Skibba & Sheth 2009) use a very slightly modified division. Our results are not sensitive to the exact choice of the cut.

   While color most directly measures star formation history, it can also be viewed as a proxy of morphology, where blue galaxies are mostly spirals and red galaxies tend to be spheroid dominated. (The two classification schemes are certainly not identical, however; see, e.g., Choi et al. 2007; Bamford et al. 2009; Blanton & Moustakas 2009; Skibba et al. 2009.) Figure 14 shows $\xi(r_p, \pi)$ separately for blue and red galaxies, for a representative case of the $-20 < M_r <$

-19 volume-limited sample. The difference between the two populations is striking. The red galaxies exhibit a substantially higher clustering amplitude and much stronger finger-of-God distortions on small scales, as seen in the elongation along the π direction for small r_p separations. These differences reflect the expected color–density relation, with red galaxies residing in more massive halos that have a stronger bias and higher velocity dispersions. The large-scale coherent distortion is more apparent in the blue sample. In linear theory, the coherent distortion depends on the parameter $\beta \approx \Omega_m^{0.6}/b$ (Kaiser 1987; Hamilton 1998), as a lower bias implies a larger gravitational perturbation for a given galaxy overdensity. The blue galaxies are better tracers of the "field" and are less biased and thus exhibit a stronger large-scale compression and only a weak finger-of-God distortion. The $\xi(r_p, \pi)$ diagram of the full $-20 < M_r < -19$ sample (Figure 5) is, of course, intermediate between these two. These results are in qualitative agreement with previous SDSS
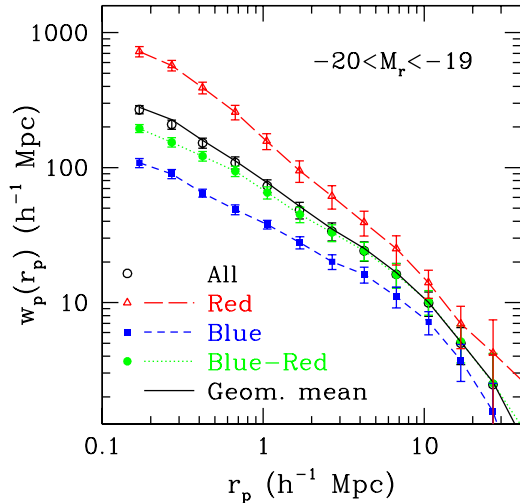
16

Figure 15. Projected correlation functions of red and blue galaxies in the $-20 < M_r < -19$ luminosity bin. Red triangles and blue squares show the autocorrelation functions of the red and blue subsamples, respectively, while open black circles show the autocorrelation of the full sample. Filled green circles show the projected cross-correlation function of the red and blue galaxies. The black solid line shows the geometric mean of the red and blue autocorrelations for comparison.

(A color version of this figure is available in the online journal.)

Table 4
Color Subsets of the Volume-limited $-20 < M_r < -19$ Sample

Sample	$N_{\rm gal}$	$\bar{n}$	r_0	γ	$\frac{\chi^2}{\rm dof}$
All	44,348	1.004	4.89 ± 0.26	1.78 ± 0.02	3.79
Red	18,892	0.428	6.63 ± 0.41	1.94 ± 0.03	5.07
Blue	25,455	0.576	3.62 ± 0.15	1.66 ± 0.03	1.66
Reddest	10,278	0.233	7.62 ± 0.42	2.07 ± 0.03	1.87
Redseq	7,542	0.171	7.23 ± 0.28	1.95 ± 0.03	1.06
Redder	8,614	0.195	5.48 ± 0.43	1.91 ± 0.04	1.84
Green	5,543	0.126	5.06 ± 0.42	1.79 ± 0.05	1.35
Bluer	11,156	0.253	4.14 ± 0.21	1.69 ± 0.04	0.89
Bluest	14,299	0.324	3.15 ± 0.15	1.71 ± 0.05	1.10

Notes. All samples use $14.5 < m_r < 17.6$. $cz_{\rm min} = 8050\,{\rm km\ s^{-1}}$ and $cz_{\rm max} = 19{,}250\,{\rm km\ s^{-1}}$. $\bar{n}$ is measured in units of $10^{-2}\,h^3\,{\rm Mpc^{-3}}$. The number of degrees of freedom (dof) is 9 (11 measured w_p values minus the two fitted parameters). The subsamples are defined using tilted color cuts as described in the text.

measurements (Z05) and with DEEP2 measurements at $z \sim 1$ (Coil et al. 2008).

Figure 15 shows the corresponding projected correlation functions, $w_p(r_p)$. The correlation function for the red sample has a higher amplitude and steeper slope than the blue sample. Fitting power laws results in a correlation length of $r_0 = 6.63 \pm 0.41\,h^{-1}$ Mpc and slope $\gamma = 1.94 \pm 0.03$ for the red galaxies versus $r_0 = 3.62 \pm 0.15\,h^{-1}$ Mpc and $\gamma = 1.66 \pm 0.03$ for the blue (see Table 4). These trends are similar for all the luminosity samples, but the differences in clustering are weaker with increasing luminosity, as is shown in Section 4.3.

4.2. Cross-correlation of Blue and Red Galaxies

The autocorrelation functions of red and blue galaxies separately do not include blue–red galaxy pairs. Another useful measurement is then the cross-correlation between blue and red galaxies. In the large-scale, linear bias approximation, where $\delta_{\rm red} = b_{\rm red}\delta_m$ and $\delta_{\rm blue} = b_{\rm blue}\delta_m$, the cross-correlation must be the geometric mean of the autocorrelations. To the extent that halos have correlation coefficient $r \equiv \xi_{hm}/\sqrt{\xi_{mm}\xi_{hh}} = 1$ with the matter distribution, the geometric mean result should hold throughout the two-halo regime, even if the halo bias is scale dependent and the matter field is nonlinear. On small scales, in the one-halo regime, the cross-correlation encodes information on the mixing of galaxy populations within the halos. Any tendency of red or blue galaxies to segregate from one another will be reflected as a deviation of the cross-correlation function from the geometric mean. For example, if some halos contained only red galaxies while other halos contained only blue galaxies, this would depress the number of one-halo pairs and push the cross-correlation function below the geometric mean. However, the prediction of the cross-correlation function has a number of subtleties; we discuss these issues and provide some simplified estimates in Appendix A. We also show in this appendix that the cross-correlation function of two galaxy populations is mathematically determined if one knows the autocorrelation of the individual populations and of the combined population;

nonetheless, the cross-correlation presents this implicit information in a more intuitive form.

We measure the cross-correlation function of the blue and red galaxy samples in an analogous way to the autocorrelations, using the Landy–Szalay estimator. Specifically, we use Equation (2) with D_1D_2 replacing DD, R_1R_2 replacing RR, and $D_1R_2 + D_2R_1$ replacing 2DR, with the subscripts denoting the two cross-correlated subsamples. Error bars are obtained similarly via jackknife resampling. Filled green circles in Figure 15 show the resulting cross-correlation function for the $-20 < M_r < -19$ sample. On large scales, as expected, we find that the cross-correlation result follows the geometric mean of the blue and red autocorrelations. On small scales (for $r_p \lesssim 2\,h^{-1}$ Mpc) we find that the cross-correlation falls below the geometric mean, possibly indicating a slight segregation of blue and red galaxies within the halos. This deviation is significant given the small error bars on these scales. Note, however, that this is very far from suggesting a full segregation into "red halos" and "blue halos." That extreme case would lead to no one-halo contribution at all, making the projected cross-correlation approximately flat for $r_p < 2\,h^{-1}$ Mpc.

We find similar behavior for the cross-correlation of red and blue galaxies in all of our luminosity subsamples. However, the depression of the cross-correlation below the geometric mean is stronger for the relatively faint samples and smaller for brighter galaxies (consistent with Z05, who showed the cross-correlation function for an $M_r < -21$ galaxy sample). Our results are also in agreement with Wang et al. (2007), who investigated in detail the cross-correlation between galaxies of different luminosities and color using an earlier SDSS sample, and with Ross & Brunner (2009), who measured angular clustering of an SDSS photometric sample. A similar depression of the cross-correlation below the geometric mean is observed by Coil et al. (2008).

Using an SDSS group catalog, Weinmann et al. (2006) find that the colors of satellite galaxies are correlated with those of their central galaxy. However, this trend, which they termed "galactic conformity," is found to have roughly the same strength independent of luminosity, so its connection to our findings is unclear. It is known that the fraction of red galaxies that are satellites becomes larger with decreasing luminosity (e.g., Z05; see also related discussions in the following subsections). Thus, the luminosity-dependent suppression of the cross-correlation function in the one-halo regime may be simply related to the
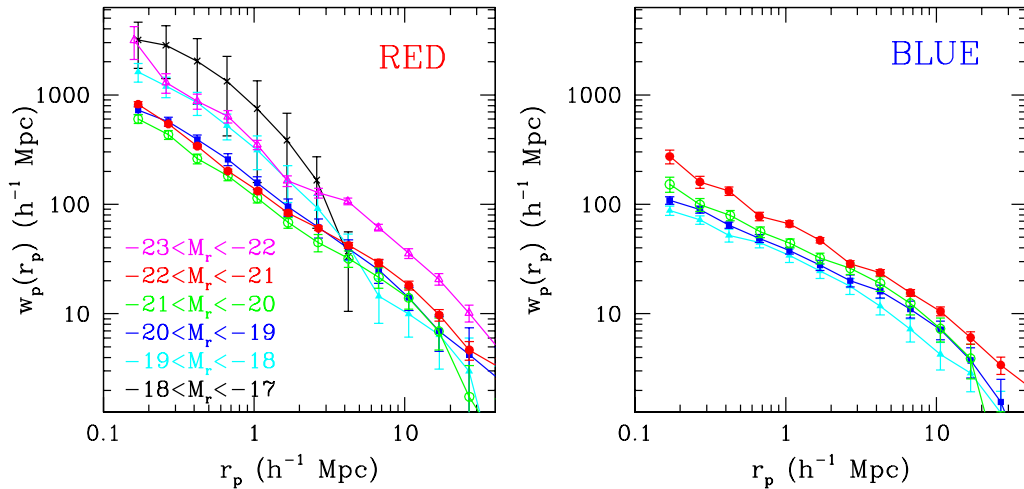
Figure 16. Projected correlation functions for different luminosity-bin samples, shown separately for red galaxies (left) and blue galaxies (right). For clarity, the brightest and faintest blue samples have been omitted from the plot, as their correlation functions are noisy.

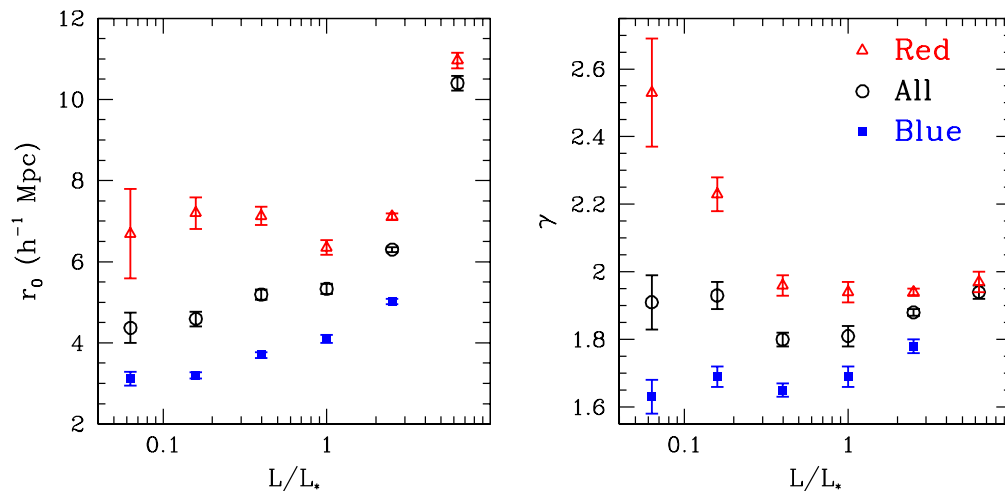(A color version of this figure is available in the online journal.)

Figure 17. Luminosity and color dependence of the galaxy correlation function. The plots show the correlation lengths (left) and slopes (right) corresponding to the real-space correlation function obtained from power-law fits to projected correlation functions using the diagonal errors. These are shown for the blue, red, and full populations of the luminosity-bin samples. Points are plotted at the luminosity of the bin center, divided by L_*, which is taken to be $M_r = -20.5$.

(A color version of this figure is available in the online journal.)

relative paucity of blue galaxies compared to red ones within large halos (see also van den Bosch et al. 2008b; Hansen et al. 2009). In future work, we will model the cross-correlation results with HOD in detail, and study the implication of these measurements for the distribution of red and blue galaxies within dark matter halos.

4.3. Joint Dependence on Color and Luminosity

We now turn to the luminosity dependence of clustering within the red and blue galaxy populations individually, using the luminosity-dependent color division of Equation (13). Figure 16 shows projected correlation functions for the volume-limited luminosity-bin samples, separately for the red (left panel) and blue (right panel) galaxies. Figure 17 shows the correlation length r_0 and slope γ of power-law fits to these samples. Because some of the samples are quite small, making jackknife estimates of the covariance matrix noisy, we fit using the diagonal error bars only, which is enough to capture the trends visible in the $w_p(r_p)$ plots. Figure 17 also shows r_0 and γ from diagonal fits to the full luminosity-bin samples. The

differences between the different color samples are particularly distinct for the fainter samples, and they decrease with increasing luminosity.

These plots display the same general trends seen in previous sections: the large-scale clustering amplitude increases with luminosity for both red and blue populations, and red galaxies generically have higher clustering amplitude and a steeper correlation function. Within the individual populations, however, the luminosity trends are remarkably different. The projected correlation functions of the blue galaxies are all roughly parallel, with slopes $1.6 \leqslant \gamma \leqslant 1.8$, and the amplitude (or correlation length) increases steadily with luminosity. For the red galaxies, on the other hand, the shape of $w_p(r_p)$ is radically different for the two faintest samples, $-18 < M_r < -17$ and $-19 < M_r < -18$, with a strong inflection at $r_p \approx 3\,h^{-1}$ Mpc indicating a high-amplitude one-halo term. These two samples have the *strongest* small-scale clustering, matched only by the ultraluminous, $-23 < M_r < -22$ galaxies. The large-scale clustering (at $r_p \approx 5$–$10\,h^{-1}$ Mpc) shows no clear luminosity dependence until the sharp jump at the $-23 < M_r < -22$
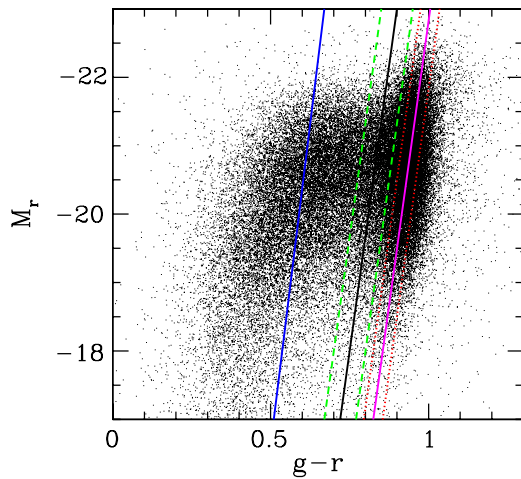
Figure 18. Color–magnitude diagram for the SDSS galaxies, showing *r*-band absolute magnitudes vs. $g - r$ colors. A random subset of the galaxies is plotted, sparsely sampled by a factor of 10. The tilted lines denote the different color samples used. The solid lines denote the division into "bluest," "bluer," "redder," and "reddest" subsamples, respectively, with increasing color. The dashed lines mark the boundary of the "green" population along the main red–blue dividing line (Equation (13)). The dotted lines indicate the "redseq" galaxy population along the locus of the red sequence. The latter two populations are *not* independent of the previous ones: the "green" galaxies include some of the "bluer" and "redder" galaxies. Similarly, the red sequence "redseq" population is comprised of some of the "redder" and "reddest" galaxies.

(A color version of this figure is available in the online journal.)

bin, though it is consistent with a weak but continuous trend at lower luminosities. Power-law fits yield significantly steeper power-law slopes for the correlation functions of the two faintest samples, together with a mild increase in the correlation lengths (see Figure 17). We caution that the $-18 < M_r < -17$ sample is very small, containing only about 5000 blue galaxies and 1000 red galaxies, and might be sensitive to cosmic variance; we have not used it in earlier sections but include it here to show the extension of the luminosity trends to the faintest galaxies we can effectively study.

The strong clustering of intrinsically faint red galaxies has been previously observed (Norberg et al. 2002; Hogg et al. 2003; Z05; Swanson et al. 2008; Cresswell & Percival 2009). We build on these studies, confirming this intriguing clustering signal and presenting its most significant measurement obtained with the largest redshift sample available. The red galaxy samples analyzed here include ∼25,000 galaxies below L_*, about 6000 of them in the two faintest bins, more than triple the size of the samples studied in Z05. The strong clustering is an indication that most of the faint red galaxies are satellites in fairly massive halos (Berlind et al. 2005; Z05; Wang et al. 2009). We present HOD models of a few of these samples in Section 4.5 below but defer a detailed examination of this population to future work.

4.4. Autocorrelation of Finer Color Samples

The large size of the DR7 main galaxy sample allows us to measure $w_p(r_p)$ for narrow bins of color in addition to the broad "blue" and "red" classifications used in Sections 4.1–4.3 and in most earlier work. Figure 18 shows the cuts we adopt to divide galaxies into "bluest," "bluer," "redder," and "reddest" populations. We also define an intermediate population of "green" galaxies, located near the minimum of the observed color bimodality along the red/blue dividing line, associated with the so-called green valley galaxies (e.g., Wyder et al. 2007;
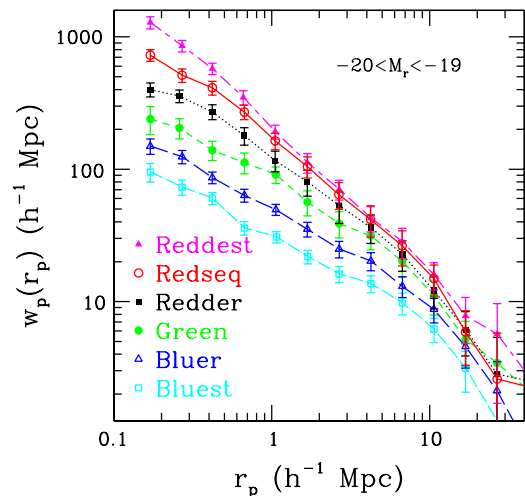

Figure 19. Projected correlation functions for various color subsamples of the $-20 < M_r < -19$ volume-limited sample. Color cuts are as defined in the text and shown in Figure 18.

(A color version of this figure is available in the online journal.)

Loh et al. 2010). We include all galaxies within $\Delta(g - r) = 0.05$ of the tilted dividing line of Equation (13) (analogous to the "green" galaxy population studied by Coil et al. 2008). In addition, we add a sample of galaxies along the cusp of the red sequence galaxies, denoted as "redseq," defined as all galaxies within $\Delta(g - r) = 0.03$ of the redder/reddest dividing line. Note that the last two classes are not distinct populations: the "green" sample contains a subset of the redder and bluer samples, while the "redseq" sample contains a subset of the redder and reddest samples. Details of the individual samples are given in Table 4.

Figure 19 shows the projected correlation functions of all these color samples, for the representative luminosity bin $-20 < M_r < -19$. We find a *continuous* trend with color, in both amplitude and slope: the redder the color of the sample, the higher and steeper the correlation function. We find the same trends in the other luminosity bins, although the dependence on color is weaker at higher luminosities, as already seen for the red/blue division in Figure 17.

Differences in clustering strengths should be reflective of the different environments of the galaxies. The steady trend of $w_p(r_p)$ with color at fixed luminosity is consistent with the findings of Hogg et al. (2003), who investigated the density of galaxy environments as a function of luminosity and color. The trend across our three red samples indicates that redder galaxies within the red sequence populate denser regions, again consistent with Hogg et al. (2003). Hogg et al. (2004) examined the color–magnitude diagram as a function of environment and did not find a significant shift of the red sequence location with density, but examining their results in detail does reveal mild changes in the locus for bulge-dominated galaxies. The trends observed in Hogg et al. (2003, 2004) are subtle, but they appear consistent with our results.

Coil et al. (2008) have carried out an analysis similar to ours at $z \sim 1$, using projected correlation functions of fine color bins in the DEEP2 galaxy survey. They find qualitatively similar results for blue galaxies and for the difference between blue and red galaxy clustering, but they find no significant change in the amplitude or slope of $w_p(r_p)$ among their red samples (see their Figure 12). The difference from our results could be a consequence of details of sample definition, or possibly a consequence of color-dependent incompleteness in DEEP2

(e.g., Gerke et al. 2007), though Coil et al. (2008) account for this in their analysis. The difference could also be an evolutionary effect reflecting the buildup of galaxies on the red sequence. One plausible explanation is that variations in star formation history and dust content contaminate and scatter galaxies within the red sequence, and from the "blue cloud" into the red sequence, when the universe is younger (e.g., Brammer et al. 2009), while evolution to $z = 0$ allows galaxy populations to separate more cleanly, yielding a tighter correlation between color, stellar population age, and environment.

The clustering of the green galaxies falls between that of the blue and red galaxy samples and clearly follows the continuous trend with color in both amplitude and slope. We do not find the apparent break in the green galaxies' projected correlation function seen in DEEP2 (Coil et al. 2008), where the clustering amplitude is similar to that of blue galaxies on small scales and to that of the red galaxies on large scales. Loh et al. (2010) investigate the clustering properties of "green valley" galaxies using UV imaging from *Galaxy Evolution Explorer* matched to SDSS spectroscopy, and find that the clustering of green galaxies is intermediate between that of the blue and red galaxies, in qualitative agreement with our results. However, they find that the green galaxies have a large-scale clustering amplitude similar to that of the blue galaxies (in contrast with Coil et al. 2008). When fitting an overall power law to the projected correlation function, they find the green galaxies' clustering amplitude to be between that of the blue and red samples, with a similar slope to that of the red galaxies, while we find the green galaxy population to be intermediate in both amplitude and slope. These differences may have to do with the different sample definition and selection in each of these and warrant further investigation.

4.5. Modeling the Color Dependence

To model the color dependence of $w_p(r_p)$ presented in Section 4.4, we adopt a simplified HOD model based on the parameterized form of the mean occupation function specified in Equation (7) for luminosity-threshold samples. For the $-20 < M_r < -19$ luminosity bin, we set the central galaxy occupation function to the difference of the $M_r < -19$ and $M_r < -20$ modeling results shown in Section 3.3. For simplicity, we also fix the slope of the satellite occupation function, α, to 1. We also assume that the occupation number of satellites at fixed halo mass follows a Poisson distribution and is independent of the central galaxy occupation number. The modeling is thus a one-parameter family, in which only M_1' is varied to fit $w_p(r_p)$, changing the relative normalization of the central and satellite occupation functions with color. The overall normalization is determined by matching the observed number density of galaxies in the color bin. In this simple model, the relative fraction of blue and red satellites has no dependence on halo mass. Different modeling approaches and more detailed parameterizations are possible, of course (e.g., Scranton 2002; Cooray 2005; Z05; Ross & Brunner 2009; Simon et al. 2009; Skibba & Sheth 2009), but this form is sufficient to explain the main trends of the color dependence. We note that our model guarantees that the sum of central galaxy occupation functions of independent color samples equals that of the full $-20 < M_r < -19$ bin sample. By construction, the sum of the satellite mean occupation functions, each of which follows a power law with soft cutoff, differs in shape slightly from the bin-sample satellite occupation, which is the difference of two power-law curves with soft cutoffs. We

Table 5
HOD and Derived Parameters for $-20 < M_r < -19$ Fine-color Subsamples

Sample	$\log M_1'$	f_{norm}	f_{sat}	$\log M_{med}$	$\frac{\chi^2}{dof}$
Reddest	12.11 ± 0.06	0.10	0.75 ± 0.03	12.61 ± 0.07	1.3
Redseq	12.39 ± 0.05	0.11	0.62 ± 0.03	12.15 ± 0.09	1.2
Redder	12.67 ± 0.04	0.18	0.46 ± 0.02	11.80 ± 0.02	1.0
Green	12.87 ± 0.05	0.14	0.34 ± 0.02	11.70 ± 0.01	0.9
Bluer	13.11 ± 0.03	0.33	0.24 ± 0.01	11.65 ± 0.01	0.5
Bluest	13.36 ± 0.05	0.47	0.15 ± 0.01	11.62 ± 0.01	2.0

Notes. The shape of the mean occupation function for central galaxies is assumed to be the difference of those of $M_r < -19$ and $M_r < -20$ samples. The mean occupation function for satellites follows a modified power law. The relative normalization of the mean occupation functions for central and satellite galaxies is determined by M_1'. The overall normalization f_{norm} is obtained from matching the observed number density (see the text). Halo mass is in units of $h^{-1} M_\odot$. The satellite fraction, f_{sat}, and the median mass of host halos, M_{med}, are derived parameters. For all samples, the number of degrees of freedom (dof) is 12 (13 measured w_p values minus one fitted parameter).

have verified, however, that the sum in our fits is close to the satellite mean occupation function of the overall bin sample, especially in the range where the occupation number is close to unity and the contribution to the small-scale clustering signal is dominant.

Figure 20 presents the results of this modeling. Points with error bars in the upper left panel are the $w_p(r_p)$ measurements for fine color bins repeated from Figure 19, with 0.25 dex offsets added between bins for visual clarity. The curves show the model predictions corresponding to the best-fit HODs, exhibited in the upper-right panel. Going from bluer galaxies to redder galaxies, the number of central galaxies steadily decreases and the number of satellite galaxies steadily increases. Although the central-to-satellite ratio is the only tunable parameter in our simplified HOD model, this is sufficient to explain the main trends observed in Figure 19: going from bluer to redder galaxies, the large-scale amplitude of $w_p(r_p)$ increases, the correlation function steepens, and the inflection at the one-to-two-halo transition becomes stronger. Table 5 lists the best-fit HOD parameters and χ^2 values. We find χ^2/dof of 0.5–1.3 for most of the color samples, the exception being the bluest sample, which has $\chi^2/dof \sim 2$. The fits can be improved by adding flexibility to the HOD model; for example, the fit for the bluest galaxies can be improved by allowing the slope of the satellite occupation function and the halo concentration to change.

The lower panels of Figure 20 display the trends of satellite fraction more clearly. In the lower right panel, we scale each occupation function by a constant factor so that the central galaxy components have the same normalization. The amplitude of the satellite occupation function increases steadily going from the bluest galaxies to the reddest galaxies. The lower-left panel plots the satellite fraction f_{sat} of each color bin against the median halo mass of galaxies in that bin. The satellite fraction rises from $\sim15\%$ for the bluest bin to $\sim75\%$ for the reddest bin, and the median halo mass increases as the fraction of galaxies that are satellites in massive halos grows. Green valley galaxies have occupation functions intermediate between the red and blue galaxies, consistent with the idea that they are a transitional population (e.g., Coil et al. 2008; Martin et al. 2007).

As discussed in Section 3.3, the trend of clustering strength with luminosity is explained principally by a rise in the central galaxy halo mass, and the satellite fraction drops with increasing luminosity because the halo mass function steepens at higher
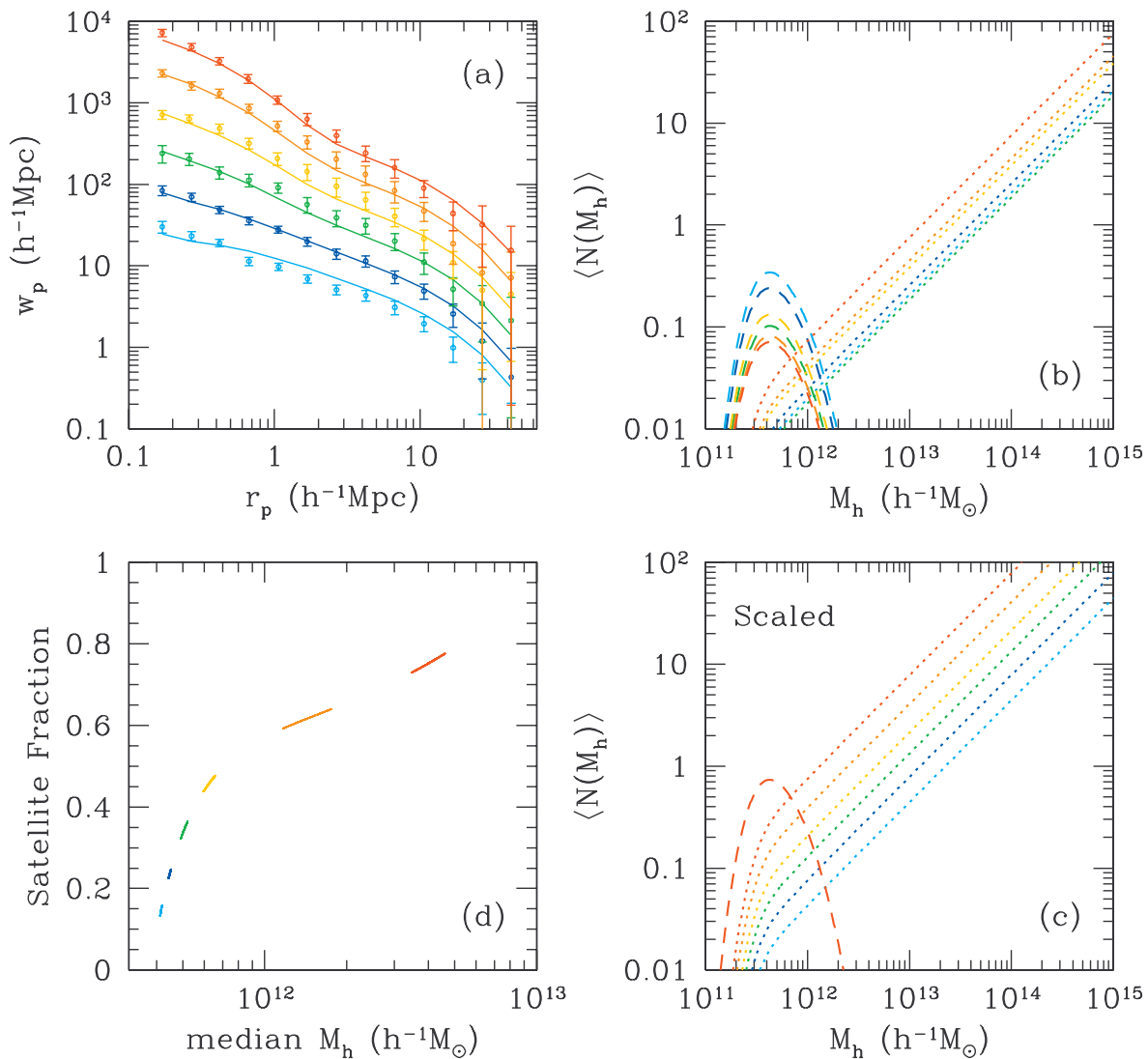
Figure 20. HOD models of the correlation function in fine color bins of the $-20 < M_r < -19$ sample. See the text for description of the HOD modeling. The top left panel shows the measured $w_p(r_p)$ and the best-fit HOD models. Offsets of 0.25 dex are added for visual clarity, with the bluest galaxies at the bottom. The top right panel presents the corresponding mean occupation functions, $\langle N(M_h) \rangle$, color-coded in the same way, with dashed and dotted lines showing contributions of central and satellite galaxies, respectively. The bottom right panel shows the same halo occupation functions normalized so that their central galaxy occupation functions coincide. The bottom left panel shows the satellite fraction vs. median halo mass for these color subsamples. Each colored "streak" shows results for models acceptable at the $\Delta\chi^2 < 1$ level; since the models have only one adjustable parameter, the uncertainty in this parameter produces a one-dimensional locus in this two-dimensional plane.
(A color version of this figure is available in the online journal.)

masses. In contrast, the trend with color at fixed luminosity can be explained with a constant halo mass for central galaxies and a steady increase of satellite fraction with redder color. The increase in typical host halo mass leads to an increase in the large-scale bias factor and thus a higher clustering amplitude at large scales. However, increasing $f_{\rm sat}$ drives the one-halo term up more rapidly than the bias factor, so the correlation function steepens for redder galaxies as well. The success of our simple HOD model does not rule out a shift in central galaxy halo mass for redder galaxies, but explaining the strong observed color trend solely through the central galaxy occupation would require placing moderate luminosity red galaxies at the centers of very massive halos, and it might well be impossible to match the clustering and number density constraints simultaneously.

Returning to the joint dependence on color and luminosity (Section 4.3), Figure 21 presents HOD model fits to the blue and red galaxy populations for three of the luminosity bins shown in Figure 16. We use the same modeling approach adopted

above for the fine color bins: we difference the central galaxy occupation functions of two luminosity-threshold samples to get the central galaxy occupation function of the luminosity bin, fix the satellite slope to $\alpha = 1$, and vary only the relative central and satellite normalizations within each population to fit the red and blue $w_p(r_p)$ measurements. With the other HOD parameters fixed previously by fitting the correlation functions of the full luminosity-threshold samples, this modeling has just one adjustable parameter within each luminosity bin. The model explains the rather complex color–luminosity trends from Figure 16 fairly well. In particular, it is able to reproduce the small-scale clustering of red galaxies increasing toward low luminosities, both in absolute terms and relative to the large-scale clustering, while the shape of $w_p(r_p)$ for the blue galaxies stays roughly constant. The fraction of red galaxies that are satellites increases sharply with decreasing luminosity, from 33% to 60% to 90% in the three luminosity bins, while the fraction of blue satellites (13%, 19%, 19%) is smaller and
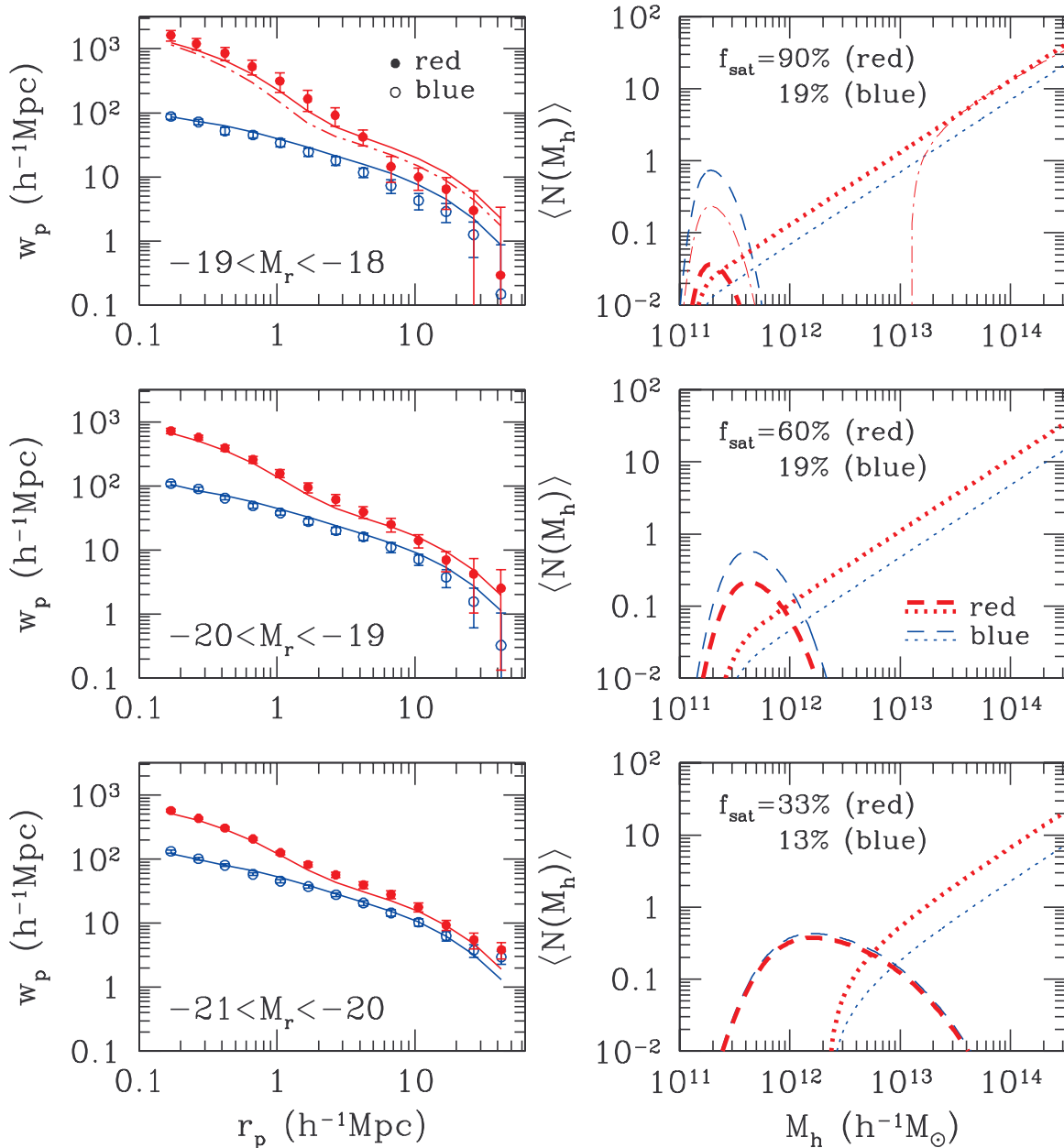
Figure 21. HOD model fits to the projected correlation functions of red and blue galaxy populations in three luminosity bins, as labeled. Points with error bars are taken from Figure 16. Solid curves in the left-hand panels show $w_p(r_p)$ for the best-fitting models. In the right-hand panels, dashed and dotted curves show the mean occupation functions for central and satellite galaxies in the red (thick line) and blue (thin line) populations. In the upper panels, dot-dashed lines indicate an alternative fit (in which more parameters are varied) for the faint red population. See the text for details of the modeling procedure.

(A color version of this figure is available in the online journal.)

only weakly dependent on luminosity. The precise values of the satellite fractions depend on the HOD parameterization used to fit $w_p(r_p)$, but the general trend is robust: most blue galaxies at these luminosities are central, and the satellite fraction for red galaxies is higher and increases toward faint luminosities.

The largest quantitative failure of this model is its overprediction of the large-scale $w_p(r_p)$ for the faintest red galaxies (and, to a smaller extent, for the faintest blue galaxies). It could be that our jackknife method underestimates the errors for this small-volume sample, and we have already noted (Figure 13) that our HOD model overpredicts the total (red+blue) galaxy correlation function in this luminosity bin. However, this discrepancy

could indicate a limitation of our restricted HOD parameterization. To investigate this possibility, we have considered models for the faint red galaxy population in which we vary the satellite slope α, the concentration parameter of red galaxies in halos, and, most notably, the satellite cutoff parameter M_0 in Equation (7).

The dot-dashed curves in the upper panels of Figure 21 show an example in which red satellites arise only in halos above $10^{13} h^{-1} M_\odot$, reducing the satellite fraction from 90% in our original fit to 34%, thereby lowering the large-scale bias factor. The physical motivation for such a model is that gas accretion (and subsequent star formation) by a satellite system might be shut off only if it enters a halo whose mass is much

larger than the "birth" halo in which it was a central galaxy (Simha et al. 2009; see also Font et al. 2008; Kang & van den Bosch 2008; Skibba 2009). The lower satellite fraction of this model is more consistent with the results of Wang et al. (2009), who argue, based on group catalogs, that 30%–60% of faint red galaxies (significantly fainter than those modeled here) are central rather than satellite galaxies. The fit to the smallest scale data points is improved by increasing the galaxy concentration parameter (van den Bosch et al. 2008a) to twice the dark matter value, steepening the profile of the one-halo term. Visually, the $w_p(r_p)$ prediction of this model is not much better than that of the original model, but the χ^2/dof drops from 3.3 to 1.4 (since the mid-range points where the deviation is largest are the most covariant), a large statistical improvement. Despite its flexibility, this model underpredicts $w_p(r_p)$ in the one-halo regime and overpredicts it in the two-halo regime, emphasizing how difficult it is to simultaneously reproduce the strong small-scale clustering and low large-scale bias factor of this galaxy sample. This tension could be a sign of environment-dependent effects on the HOD, but the expected form of "assembly bias" for low-mass halos, putting the redder central galaxies into older, more clustered halos, would exacerbate the discrepancies with the data further.

Overall, our inferences from HOD modeling accord well with the theoretical predictions of Berlind et al. (2005), who compared the results of cosmological smoothed particle hydrodynamic simulations to Hogg et al.'s (2003) measurements of galaxy environments as a function of luminosity and color. In particular, Berlind et al. (2005) find that the environment of satellite galaxies in the simulations is strongly correlated with stellar population age (hence color), and that for low and intermediate luminosities the environmental dependence of the overall galaxy population tracks that of satellite galaxies. Berlind et al. (2005) also find that the great majority of faint red galaxies in the simulation are satellites, though the simulation they use to study this population is small. The success of our simple HOD models in reproducing the observed color dependence of $w_p(r_p)$ contrasts with the recent conclusions of Ross & Brunner (2009), who find that some segregation of early- and late-type galaxies into separate halos is required to reproduce their measured angular clustering of an SDSS photometric galaxy sample, which extends to smaller separations.

5. CONCLUSIONS AND PROSPECTS

The SDSS galaxy redshift survey allows high-precision clustering measurements for a broadly selected galaxy sample with extensive, high-quality photometric information. We have examined the luminosity and color dependence of the galaxy correlation function in the DR7 main galaxy sample, which includes approximately 700,000 galaxies over 8000 deg^2, with a median redshift of ~ 0.1. This is the largest sample used to date for such studies, by a factor of several. Furthermore, the DR7 main galaxy sample is likely to remain the definitive low-redshift galaxy survey for many years; other ongoing and planned surveys, including the BOSS survey of LRGs in SDSS-III (Eisenstein et al. 2011), will probe larger volumes and higher redshifts, but they will not target a wide range of galaxy types in the present-day universe. Our analysis focuses on the projected autocorrelation functions calculated for volume-limited samples defined by luminosity and color cuts, with measurements tabulated in Appendix C. We use HOD modeling

to interpret these measurements in terms of the relation between galaxies and dark matter halos, assuming a ΛCDM cosmological model with $\Omega_m = 1 - \Omega_\Lambda = 0.25$, $\Omega_b = 0.045$, $h = 0.7$, $n_s = 0.95$, and $\sigma_8 = 0.8$.

The amplitude of $w_p(r_p)$ increases with increasing galaxy luminosity, slowly for $L < L_*$ and rapidly for $L > L_*$, where L_* corresponds to $M_r = -20.44$ (Blanton et al. 2003c; we quote absolute magnitudes for $h = 1$ throughout the paper). For $L \leqslant L_*$, $w_p(r_p)$ is reasonably described by a power law at $r_p < 10\,h^{-1}$ Mpc, while brighter samples show clear and increasingly strong inflections at $r_p \approx 1$–$3\,h^{-1}$ Mpc. We find similar trends for samples defined by luminosity bins and by luminosity thresholds. The large-scale bias factor of luminosity-threshold samples is well described by the fitting formula $b_g(>L) = 1.06 + 0.21(L/L_*)^{1.12}$. For luminosity-bin samples, we find $b_g(L) = 0.97 + 0.17(L/L_*)^{1.04}$, similar to the luminosity dependence found by Norberg et al. (2001) for b_J-selected galaxies in the 2dFGRS.

At fixed luminosity, the redshift-space correlation function of red galaxies exhibits stronger "finger-of-God" distortions than that of blue galaxies, while the blue galaxies exhibit stronger large-scale, coherent flow distortions. The projected correlation function of red galaxies is steeper and higher in amplitude. The cross-correlation of red and blue galaxies is equal to the geometric mean of the autocorrelation functions on large scales, but it falls slightly below the geometric mean for $r_p \lesssim 1\,h^{-1}$ Mpc. Adopting fine color bins, we find a continuous trend of clustering with color: the bluest galaxies have a shallow, low-amplitude correlation function, the clustering of "green valley" galaxies is intermediate between that of blue and red galaxies, and the reddest galaxies have a (slightly) steeper correlation function than galaxies that trace the ridge of the red sequence. We present detailed results for the $-20 < M_r < -19$ luminosity bin, but we find similar trends in other bins where our statistics are good enough to measure them.

The luminosity dependence of clustering for the red and blue populations is strikingly different. For blue galaxies, the amplitude of $w_p(r_p)$ increases slowly but steadily with luminosity over the range $M_r = -18$ to $M_r = -22$, with nearly constant shape. For red galaxies, there are only weak luminosity trends over the range $-22 < M_r < -19$. The $-23 < M_r < -22$ galaxies have a much higher correlation amplitude and a strong break in $w_p(r_p)$ at $r_p \approx 2\,h^{-1}$ Mpc. Most remarkably, the small-scale ($r_p < 2\,h^{-1}$ Mpc) correlation function of the $-19 < M_r < -18$ red galaxies is equal to that of the $-23 < M_r < -22$ red galaxies, a factor of 2–3 higher than that of intermediate luminosity red galaxies. Red galaxies with $-18 < M_r < -17$ show even stronger small-scale clustering, though our survey volume for such low-luminosity systems is small.

Our HOD modeling shows that these varied trends in the amplitude and shape of $w_p(r_p)$ can, for the most part, be well explained by the combination of ΛCDM cosmology and physically plausible recipes for the relation between galaxies and dark matter halos. The luminosity dependence of $w_p(r_p)$ arises from an overall shift in the mass scale of the mean occupation function $\langle N(M_h) \rangle$. The halo mass $M_{\min}$ for hosting central galaxies of luminosity L rises with luminosity. Correspondingly, the central galaxy luminosity increases with halo mass as $L/L_* = A(M_{\min}/M_t)^{\alpha_M} \exp(-M_t/M_{\min} + 1)$, where $A = 0.32$, $M_t = 3.08 \times 10^{11} h^{-1} M_\odot$, $\alpha_M = 0.264$, and $M_{\min}$ is the halo mass at which the median luminosity of central galaxies is L. The

mass M_1 at which halos host an average of one satellite above luminosity L follows a similar trend: we find $M_1 \approx 17M_{\min}$ over most of our luminosity range, with a smaller factor at the highest luminosities. We find substantial scatter ($\approx$0.3 dex) between halo mass and central galaxy luminosity for $L > L_*$, while fits for lower luminosities are consistent with little or no scatter.

The color dependence of $w_p(r_p)$ at fixed luminosity can be explained well by a change in the relative fractions of central and satellite galaxies. In our best-fit models of the $-20 < M_r < -19$ bin, for example, the satellite fraction rises steadily from 15% for the bluest galaxies to 75% for the reddest galaxies. Increasing the satellite fraction increases the large-scale bias factor by placing more galaxies in high-mass halos, and it produces a steeper correlation function with a stronger inflection by boosting the one-halo term relative to the two-halo term. A modest offset in the halo mass scale for *central* red and blue galaxies is physically plausible, but our models are able to fit the main observed trends without such offsets, and it is unlikely that the central galaxy mass scale can be the primary driver of the observed color trends in $w_p(r_p)$.

Differences in satellite fractions largely explain the different luminosity dependence of $w_p(r_p)$ for red and blue galaxies. However, within our standard parameterization we are unable to find a statistically acceptable fit to the clustering of the red $-19 < M_r < -18$ galaxies. After adjusting the model to allow red satellites only in relatively high-mass halos ($M_h > 10^{13}h^{-1} M_\odot$, a factor of 100 above $M_{\min}$), we do find a statistically acceptable fit, but even this model underpredicts the one-halo term of $w_p(r_p)$ while overpredicting the two-halo term. The difficulty in reproducing $w_p(r_p)$ for faint red galaxies could signify a breakdown of our assumption that the HOD is independent of large-scale environment, but the obvious forms of environment dependence (redder central galaxies in older halos) go in the wrong direction. Clearly the clustering of the faint red galaxy population merits further study. While we do not know of any planned redshift surveys that will provide better statistics for such low-luminosity galaxies, cross-correlation of photometric samples with redshift samples of more luminous galaxies may allow higher precision clustering measurements from a larger effective volume.

Our measured luminosity and color trends agree with those found in earlier studies, most notably the Norberg et al. (2001, 2002) studies of the 2dFGRS and the Z05 study of SDSS DR2, but the SDSS DR7 sample allows measurements of higher precision, greater detail, and wider dynamic range. Our conclusions about the luminosity and color dependence of galaxy halo occupations are generally consistent with those found in earlier studies (e.g., van den Bosch et al. 2003b; Collister & Lahav 2005; Yang et al. 2005a; Z05), although the greater precision and dynamic range of our clustering measurements allows us to examine this dependence in substantially greater detail. Even with SDSS DR7, the tests in Section 3.2 reveal significant finite-volume effects for samples with limiting absolute magnitude $M_r \approx -20$, which extend just far enough to enclose the SGW, and for samples with limiting magnitude $M_r \geqslant -18$, which have small total volume. These effects have a significant influence on the (r_0, γ) values of power-law fits to these samples (and their color-defined subsamples). They have little impact on the best-fit values of HOD parameters, though they do affect the χ^2 values of HOD fits. The finite-volume uncertainties limit the strength of our conclusions about the faint red galaxy population.

Our modeling in this paper derives HOD parameters for well-specified classes of galaxies defined by thresholds or bins in luminosity and divisions in color. The related formalism of CLFs (Yang et al. 2003) seeks to provide a continuous description of the dependence of the galaxy luminosity function on halo mass. In a subsequent paper (Z. Zheng et al. 2011, in preparation), we will present a generalization of this approach to luminosity–color distributions and apply it to our $w_p(r_p)$ data, resulting in a comprehensive model that synthesizes the information from all of the measurements presented here.

Our HOD parameterization is flexible enough to describe the predictions of galaxy formation models accurately (Zheng et al. 2005), and with an assumed cosmological model the $w_p(r_p)$ measurements are themselves sufficient to provide tight constraints on HOD parameters. Studies of other real-space clustering measures, such as the multiplicity function of groups, the three-point correlation function, the topology of isodensity surfaces, and the void probability function can test the HOD models presented here, perhaps revealing breakdowns of this parameterization that would point to new aspects of galaxy formation physics. Most interesting would be to find evidence for environmental variations of the HOD, as this would tie observable galaxy properties to features of halo formation history that correlate with large-scale environment at fixed halo mass. Conversely, limits on environmental variations (e.g., Blanton & Berlind 2007; Tinker et al. 2008) limit the degree to which galaxy properties can be driven by quantities such as halo formation time or concentration.

Uncertainties in cosmological parameters within the range allowed by other data have little impact on our conclusions. The largest effect is that changes to Ω_m or σ_8 would shift the mass scale of the HOD (Zheng & Weinberg 2007). The combination of $w_p(r_p)$ constraints with dynamical measures that are sensitive to the halo mass scale allows novel constraints on these cosmological parameters. Efforts in this direction are underway, using cluster mass-to-light ratios, galaxy–galaxy lensing, and redshift-space distortions. We expect these analyses, together with the cluster abundance analysis of Rozo et al. (2010), to yield tight independent constraints on σ_8 and Ω_m with several systematic cross-checks. These constraints, based on the inferred amplitude of dark matter clustering, are complementary to those derived from the large-scale *shape* of the galaxy power spectrum (Reid et al. 2010), which can themselves be sharpened by using HOD modeling to account for the effects of scale-dependent galaxy bias (Yoo et al. 2009). The combination of these constraints with those derived from CMB data, Type Ia supernovae, baryon acoustic oscillations, and other cosmological observables will allow stringent consistency tests of the ΛCDM cosmological model, at the few percent level. Surveys of the next decade will extend many of these techniques to higher redshifts, but the SDSS maps of structure in the present-day universe still have much to teach us about galaxy formation and the physics of the cosmos.

APPENDIX A

THE CROSS-CORRELATION FUNCTION OF GALAXIES

A.1. The Relation between the Cross-correlation and Autocorrelation Functions of Galaxy Samples

Zu et al. (2008) consider the general case of the relation between the two-point autocorrelation functions of a galaxy sample and the auto- and cross-correlation functions of its subsamples (see their appendix). Here, we focus on the specific case of the correlation functions of red, blue, and all galaxies. The point we make here is that only three of the four correlation functions (blue–blue, red–red, all–all autocorrelation functions, and red–blue cross-correlation functions) are independent. That is, if we measured blue–blue, red–red, and all–all autocorrelation functions, there would be no new information from the red–blue cross-correlation functions.

To demonstrate that this is the case, we recall that the two-point correlation function represents a galaxy pair count. The total number of pairs of all galaxies in the parent sample is simply the sum of the numbers of red galaxy pairs, blue galaxy pairs, and red–blue galaxy pairs. That is

$$\frac{1}{2}n_{\rm all}^2(1+\xi_{\rm all}) = \frac{1}{2}n_{\rm blue}^2(1+\xi_{\rm blue}) + \frac{1}{2}n_{\rm red}^2(1+\xi_{\rm red}) + n_{\rm blue}n_{\rm red}(1+\xi_{\rm cross}), \quad (A1)$$

where $n_{\rm all}$, $n_{\rm red}$, and $n_{\rm blue}$ are the mean number density of the parent sample and the red/blue subsamples, $\xi_{\rm all}$, $\xi_{\rm blue}$, and $\xi_{\rm red}$ are the two-point autocorrelation functions, and $\xi_{\rm cross}$ is the red–blue two-point cross-correlation function. The factor of $1/2$ in front of the autocorrelation terms is to avoid the double count of autopairs. Since $n_{\rm all} = n_{\rm red} + n_{\rm blue}$, the above identity reduces to

$$n_{\rm all}^2\xi_{\rm all} = n_{\rm blue}^2\xi_{\rm blue} + n_{\rm red}^2\xi_{\rm red} + 2n_{\rm blue}n_{\rm red}\xi_{\rm cross}. \quad (A2)$$

The same relation holds for projected correlation functions w_p. Thus, the red–blue cross-correlation function can be derived from the three autocorrelation functions.

As a test of this relation, we predicted the red–blue cross-correlation function based on the measured all–all, red–red, and blue–blue autocorrelation functions for the $-20 < M_r < -19$ volume-limited galaxy sample. The prediction agrees essentially perfectly with the measured cross-correlation function shown in Figure 15, with deviations much smaller than the 1σ error bars.

There is thus, in theory, no new information provided by the cross-correlation function, when one has measured the three individual autocorrelation functions. In practice, the relation in Equation (A2) and that for projected two-point correlation functions can be used for a consistency check. Furthermore, for understanding the mixture among different galaxy populations, the cross-correlation function is more readily interpreted than the consistency relation itself. For example, segregation of "red" and "blue" halos would produce a distinctive suppression of the one-halo term of the cross-correlation function, while its effect on the autocorrelation functions (boosting the red and blue autocorrelations relative to the all autocorrelation) might be difficult to disentangle from changes in satellite occupation slopes, concentration parameters, and so forth.

A.2. The Relation between the Cross-correlation Function and the Geometric Mean of the Autocorrelation Functions

The two-point cross-correlation function of two populations (e.g., red and blue galaxies we study here) is often compared to the geometric mean of the two-point autocorrelation functions to infer the information about the mixing of the two populations. On large scales, where the two-halo term dominates the correlation functions, the cross-correlation function is guaranteed to be the geometric mean of the autocorrelation functions.[17] On small scales, where the one-halo term dominates, it is not obvious what we can infer if there are deviations of the cross-correlation function from the geometric mean. We show here that the situation becomes even less clear for projected correlation functions.

As an example, consider the two-point autocorrelation functions of red and blue galaxies, $\xi_{\rm red}$ and $\xi_{\rm blue}$, and their cross-correlation function $\xi_{\rm cross}$. Under the assumption that these correlation functions are positive, we have

$$\left(\int\sqrt{\xi_{\rm red}(r_p,\pi)\xi_{\rm blue}(r_p,\pi)}d\pi\right)^2 \leqslant \int\xi_{\rm red}(r_p,\pi)d\pi \times \int\xi_{\rm blue}(r_p,\pi)d\pi \quad (A3)$$

from the Cauchy–Schwartz inequality. Even if we had $\xi_{\rm cross} = \sqrt{\xi_{\rm red}\xi_{\rm blue}}$ on all scales, the above inequality would mean that the projected correlation functions satisfy

$$w_{p,\rm cross} \leqslant \sqrt{w_{p,\rm red}w_{p,\rm blue}}. \quad (A4)$$

The equality only holds for the case where both galaxy populations trace the same dark matter distribution and $\xi_{\rm red}$ and $\xi_{\rm blue}$ are parallel to each other, which is true on large scales but not on small scales.

---

[17] This statement relies on the fact that the host halo populations are tracing the same dark matter distribution. One can construct a physically absurd but mathematically acceptable model with zero cross-correlation by superposing the halo populations of two independent N-body simulations in a single cube, populating one with red galaxies and the other with blue.

APPENDIX B

ROBUSTNESS OF MEASUREMENTS

Measuring projected correlation functions from galaxy redshift data involves a set of standard procedures. We test here the sensitivity of our measurements to some key details of these procedures (described in Section 2). Figure 22 presents projected correlation functions for several variants of our standard technique, calculated for the $M_r < -21$ sample, which yields the smallest statistical errors among our samples. The overall visual impression of the plotted projected correlation functions (top panels) demonstrates the robustness of the measurements, but we examine it in more detail by looking at the fractional deviations from our standard case (bottom panels).

The measurements presented in the paper all use the Landy & Szalay (1993) estimator, the standard for such studies, and we show here (left-hand side) results when using also the estimators of Hamilton (1993, long-dashed red line) and Davis & Peebles (1983, short-dashed blue line). We find that the alternative estimators provide similar measurements to the Landy–Szalay one, with some differences on small scales for the Hamilton estimator and a significant deviation of the Davis–Peebles measurement on large scales. Our results are in accord with long-standing claims that the Davis–Peebles estimator is more sensitive to uncertainties in the galaxy mean density, with the differences becoming apparent on large scales (Hamilton 1993; Strauss & Willick 1995; Pons-Borderia et al. 1999), and that the Landy–Szalay estimator has improved shot-noise behavior (Landy & Szalay 1993; Szapudi & Szalay 1998). A detailed examination of different clustering estimators is given by Pons-Borderia et al. (1999).

The angular selection function is carefully calculated in each sector on the sky, with an average completeness of 0.97. The detailed angular completeness is mimicked in the random samples, and is then used to weight both real and random galaxies. The main analyses of the paper imposed a cut on the angular completeness of $f_{\rm comp} > 0.5$, to avoid shot noise from undersampled regions. A more conservative cut of $f_{\rm comp} > 0.9$ (which eliminates ~1400 additional galaxies; dot-dashed green line in the left-hand side) results in negligible changes to the

Table 6
Variants of the Standard Measurement for the $M_r < -21$ Sample

Sample	r_0	γ	$\frac{\chi^2}{\rm dof}$
Standard	5.98 ± 0.12	1.96 ± 0.02	6.1
Davis–Peebles	6.06 ± 0.11	1.94 ± 0.01	5.9
Hamilton	6.02 ± 0.10	1.94 ± 0.01	5.4
$f_{\rm comp}$	6.03 ± 0.11	1.95 ± 0.02	5.8
No ang. comp.	5.92 ± 0.12	1.97 ± 0.02	6.1
$\pi_{\rm max} = 80$	6.06 ± 0.13	1.95 ± 0.02	6.0
Random	6.01 ± 0.12	1.95 ± 0.02	6.1
$\Omega_{\rm m} = 0.25$	5.97 ± 0.10	1.97 ± 0.01	6.4
$z_{\rm min} = 0.05$	6.01 ± 0.10	1.95 ± 0.01	6.5

Note. r_0 and γ are obtained from fitting a power law to $w_p(r_p)$ for $r_p < 20\,h^{-1}$ Mpc, using the full error covariance matrices.

measurements. If we drop the weighting of both real and random galaxies by the angular completeness, it also makes no difference to the results. However, neglecting to address the angular incompleteness altogether (i.e., by not including it in the random catalog and not weighting either data or randoms by it; dotted magenta line) results in a couple of percent difference.

We test additional variants of our standard procedures in the right-hand side of Figure 22. The dashed blue curve shows the effect of integrating $w_p(r_p)$ up to $\pi_{\rm max} = 80\,h^{-1}$ Mpc instead of $60\,h^{-1}$ Mpc. Replacing the random catalog with another realization of equal size makes negligible difference except at the smallest separations; the slight changes in the innermost bins show the importance of using a sufficiently large random catalog. Changing the assumed Ω_m from 0.3 to 0.25 when calculating comoving separations produces a small (~2%) systematic shift of the measurements. Finally, relaxing the bright flux limit of 14.5, needed for defining the luminosity-threshold samples, might introduce occasional problems with galaxy deblending or saturation nearby ($z < 0.05$), but increasing the minimum redshift from 0.02 to 0.05 results in negligible differences.

Table 6 presents power-law fits to the projected correlation functions for each variant. In all of these cases, we find an overall change in the best-fitting power-law parameters of at

Table 7
Projected Correlation Function Measurements of Magnitude Bin Samples

r_p	-23 to -22	-22 to -21	-21 to -20	-20 to -19	-19 to -18	-18 to -17
0.17	2307 (510)	536.1 (25.4)	297.9 (9.9)	269.0 (18.3)	268.4 (46.7)	211.6 (64.7)
0.27	1200 (208)	359.0 (12.4)	231.5 (7.8)	208.7 (16.3)	212.1 (37.0)	203.9 (67.3)
0.42	713.4 (100.0)	238.6 (6.5)	166.4 (6.6)	152.2 (13.1)	153.7 (31.0)	158.1 (58.7)
0.67	527.2 (62.0)	148.7 (4.8)	117.2 (5.4)	108.8 (11.2)	109.8 (22.1)	114.4 (46.8)
1.1	274.1 (25.6)	99.1 (3.2)	79.3 (4.3)	73.1 (7.9)	75.1 (18.0)	79.4 (34.1)
1.7	155.6 (15.4)	65.6 (2.2)	55.8 (3.6)	48.5 (6.8)	47.1 (12.0)	53.0 (20.8)
2.7	109.7 (10.7)	47.2 (2.0)	40.4 (3.3)	33.8 (5.2)	31.4 (7.6)	36.7 (13.9)
4.2	92.0 (5.9)	34.0 (1.8)	29.3 (3.1)	24.2 (4.0)	18.0 (4.0)	21.7 (9.9)
6.7	56.1 (3.8)	23.6 (1.5)	20.9 (2.7)	16.2 (3.3)	9.43 (2.50)	12.9 (6.2)
10.6	33.2 (3.1)	14.9 (1.3)	13.9 (2.0)	9.94 (2.03)	5.95 (1.68)	2.43 (3.10)
16.9	19.4 (2.3)	8.30 (0.92)	7.87 (1.32)	5.00 (1.53)	3.73 (1.31)	0.23 (3.04)
26.8	10.3 (1.7)	4.08 (0.72)	4.59 (1.09)	2.47 (1.68)	1.82 (1.11)	-0.93 (1.71)
42.3	5.21 (1.26)	2.68 (0.54)	3.40 (0.85)	1.11 (1.28)	0.23 (1.15)	-4.89 (1.85)

Notes. The first column provides the pair-weighted-projected separation of the bin. Subsequent columns provide the projected correlation function values, $w_p(r_p)$, for the volume-limited samples corresponding to the specified absolute magnitude M_r bins. The diagonal terms of the error covariance matrices are given in parentheses. For reasonable power-law interpolations, the pair-weighted-projected separations vary by at most 1% from the r_p for which $w_p(r_p)$ equals the pair-weighted average in the bin (see Section 2.2).
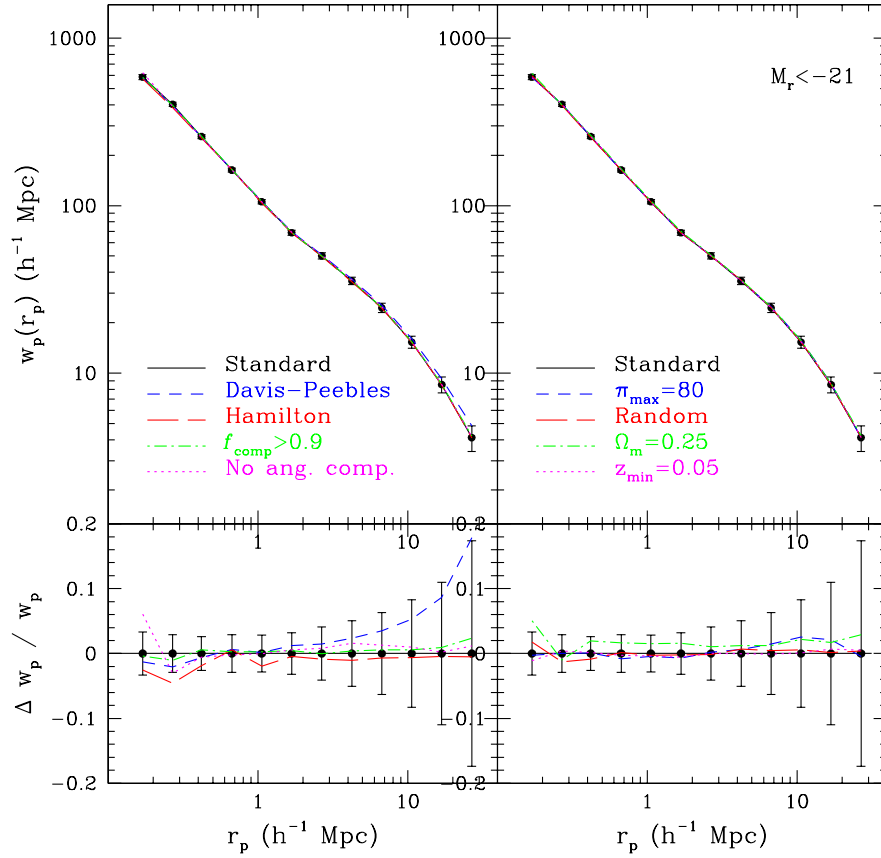
Figure 22. Robustness of the w_p measurements to different uncertainties. Top panels show projected correlation functions for different variants of our standard procedures (see the text) calculated for the $M_r < -21$ sample. Points with error bars represent our standard measurements for this sample. Bottom panels show the fractional deviations of these variants compared to our standard case. For clarity, error bars are shown only for the latter and are comparable for all other cases.

(A color version of this figure is available in the online journal.)

Table 8
Projected Correlation Function Measurements of Magnitude-threshold Samples

r_p	−22.0	−21.5	−21.0	−20.5	−20.0	−19.5	−19.0	−18.5	−18.0
0.17	2615 (491)	1028 (68)	586.2 (19.5)	455.7 (11.3)	366.1 (9.3)	307.0 (9.2)	322.5 (17.0)	313.3 (25.9)	294.3 (34.7)
0.27	1189 (202)	731.7 (34.0)	402.9 (11.7)	296.9 (6.9)	264.3 (7.6)	228.5 (8.3)	231.1 (15.3)	230.2 (24.9)	221.5 (32.1)
0.42	728.0 (96.3)	392.6 (17.1)	258.7 (6.7)	197.0 (5.1)	184.0 (6.6)	159.3 (7.2)	162.4 (12.8)	165.4 (21.1)	161.4 (27.6)
0.67	491.4 (55.3)	228.6 (10.9)	163.2 (4.7)	134.1 (4.1)	128.6 (5.5)	110.4 (5.6)	114.6 (10.3)	118.3 (17.5)	114.7 (22.0)
1.1	272.8 (23.2)	144.6 (6.4)	105.5 (3.0)	89.4 (3.3)	84.7 (4.3)	72.9 (4.2)	75.5 (7.7)	79.7 (13.2)	75.5 (16.5)
1.7	154.4 (14.5)	94.3 (3.7)	68.9 (2.2)	61.1 (2.6)	59.4 (3.6)	49.8 (3.4)	50.6 (6.0)	53.8 (10.5)	48.6 (11.5)
2.7	111.5 (10.4)	70.5 (2.7)	50.2 (2.1)	44.0 (2.3)	42.9 (3.3)	34.6 (2.9)	35.0 (4.7)	37.4 (7.8)	32.4 (7.7)
4.2	94.5 (5.6)	48.6 (2.3)	35.5 (1.8)	31.2 (2.0)	30.9 (3.1)	24.6 (2.5)	24.2 (3.6)	25.9 (5.8)	19.7 (4.4)
6.7	56.8 (3.8)	33.1 (1.8)	24.5 (1.6)	21.3 (1.8)	21.9 (2.7)	16.7 (2.4)	15.3 (2.9)	17.4 (4.5)	10.8 (2.8)
10.6	35.1 (3.2)	20.9 (1.5)	15.3 (1.3)	13.7 (1.5)	14.6 (2.1)	10.7 (1.9)	9.20 (1.78)	10.6 (2.6)	6.35 (1.93)
16.9	22.0 (2.2)	11.6 (1.2)	8.54 (0.94)	7.65 (1.07)	8.24 (1.32)	5.73 (1.28)	4.11 (1.29)	5.31 (1.42)	3.62 (1.34)
26.8	11.4 (1.6)	6.04 (0.95)	4.11 (0.71)	4.09 (0.88)	4.88 (1.06)	2.82 (1.13)	1.81 (1.39)	3.56 (1.76)	2.14 (1.23)
42.3	5.89 (1.21)	3.28 (0.64)	2.73 (0.54)	3.21 (0.70)	3.58 (0.85)	1.39 (0.91)	0.72 (1.24)	0.96 (1.02)	0.56 (1.26)

Notes. The first column provides the pair-weighted-projected separation of the bin. Subsequent columns provide the projected correlation function values, $w_p(r_p)$, for the volume-limited samples corresponding to the specified absolute magnitude M_r^{max} thresholds. The diagonal terms of the error covariance matrices are given in parentheses.

most 1%, smaller than or comparable to the statistical error bars, highlighting the robustness of our results. While adopting the Davis & Peebles (1983) estimator or entirely dropping angular completeness corrections makes a (marginally) noticeable change in parameter values, these choices would clearly not be optimal; the smaller changes associated with the Hamilton (1993) estimator or with raising the completeness threshold are better indicators of the associated systematic uncertainty.

APPENDIX C

CORRELATION FUNCTION MEASUREMENTS

The following tables present the projected correlation function values that are used in this work, together with the diagonal error bars on the measurements. Tables 7 and 8 present the measurements from the volume-limited luminosity samples described in Section 3. The tables include the projected correlation functions measured for the samples

Table 9
Projected Correlation Function Measurements of Blue Galaxy Samples Corresponding to Magnitude Bins

r_p	−23 to −22	−22 to −21	−21 to −20	−20 to −19	−19 to −18	−18 to −17
0.17		273.8 (40.0)	131.7 (8.0)	108.4 (8.5)	87.6 (8.5)	59.2 (10.8)
0.27		160.2 (19.6)	101.1 (5.4)	89.7 (6.9)	72.1 (6.6)	78.2 (11.7)
0.42		132.5 (11.6)	80.3 (3.9)	64.8 (4.4)	52.1 (6.9)	60.9 (10.1)
0.67	111.6 (350.0)	77.7 (7.0)	58.1 (3.0)	48.8 (4.1)	44.9 (4.7)	46.2 (9.6)
1.1	164.5 (129.8)	66.4 (4.4)	45.3 (2.3)	37.9 (2.8)	34.1 (4.8)	40.3 (8.1)
1.7	55.6 (62.6)	47.0 (2.5)	37.2 (2.0)	27.9 (2.9)	24.6 (3.6)	31.5 (8.5)
2.7	20.9 (36.9)	28.7 (1.9)	27.9 (1.8)	20.1 (2.5)	18.0 (2.9)	25.2 (8.5)
4.2	98.9 (32.8)	23.8 (1.6)	20.7 (1.7)	16.1 (2.2)	11.8 (2.0)	17.9 (7.5)
6.7	56.9 (16.8)	15.6 (1.1)	14.5 (1.6)	11.1 (1.9)	7.26 (1.74)	10.6 (4.7)
10.6	32.7 (13.8)	10.6 (1.0)	10.4 (1.4)	7.17 (1.40)	4.27 (1.20)	1.95 (2.50)
16.9	25.6 (8.4)	6.08 (0.79)	6.33 (1.09)	3.75 (1.15)	2.87 (0.93)	−1.01 (2.12)
26.8	15.7 (7.1)	3.41 (0.61)	3.77 (0.84)	1.57 (0.96)	1.26 (0.70)	−0.68 (1.27)
42.3	13.6 (4.0)	2.07 (0.51)	2.95 (0.68)	0.33 (0.71)	0.15 (0.72)	−3.64 (1.15)

Notes. The first column provides the pair-weighted-projected separation of the bin. The subsequent columns provide the projected correlation function values, $w_p(r_p)$, for the blue galaxy samples corresponding to the specified absolute magnitude M_r bins. The diagonal terms of the error covariance matrices are given in parentheses.

Table 10
Projected Correlation Function Measurements of Red Galaxy Samples Corresponding to Magnitude Bins

r_p	−23 to −22	−22 to −21	−21 to −20	−20 to −19	−19 to −18	−18 to −17
0.17	3158 (1061)	821.7 (45.5)	570.9 (24.4)	724.0 (63.0)	1623 (311)	3182 (1439)
0.27	1300 (268)	542.0 (24.1)	433.1 (17.5)	570.7 (51.3)	1197 (252)	2839 (1437)
0.42	875.7 (135.5)	339.6 (12.3)	305.1 (14.7)	390.7 (39.3)	852.6 (203.1)	2034 (1218)
0.67	633.7 (82.3)	201.7 (7.8)	206.5 (11.4)	257.5 (31.9)	525.5.9 (138.8)	1329 (909)
1.1	350.4 (35.0)	132.4 (5.1)	125.8 (8.6)	157.1 (21.2)	313.6 (106.9)	749.7 (592.2)
1.7	164.3 (18.4)	83.4 (3.5)	82.0 (6.8)	95.0 (17.3)	165.2 (61.3)	385.6 (296.9)
2.7	127.3 (13.1)	60.3 (2.9)	56.8 (5.5)	61.3 (12.0)	91.6 (29.4)	166.3 (106.1)
4.2	107.0 (7.5)	42.2 (2.6)	39.6 (4.8)	39.3 (8.2)	42.1 (11.5)	33.4 (22.9)
6.	61.3 (4.2)	29.2 (2.2)	28.0 (4.1)	25.1 (6.1)	14.5 (6.3)	15.8 (18.5)
10.6	35.6 (3.5)	18.2 (1.7)	17.8 (2.9)	14.1 (3.3)	9.93 (3.82)	−4.73 (7.73)
16.9	20.7 (2.5)	9.74 (1.21)	9.30 (1.68)	6.97 (2.42)	6.43 (3.32)	14.5 (15.0)
26.8	10.2 (1.8)	4.68 (0.92)	5.47 (1.48)	4.23 (3.20)	2.99 (3.01)	−5.02 (7.43)
42.4	4.69 (1.18)	3.22 (0.68)	3.85 (1.08)	2.53 (2.40)	0.29 (3.04)	−15.6 (9.6)

Notes. The first column provides the pair-weighted-projected separation of the bin. The subsequent columns provide the projected correlation function values, $w_p(r_p)$, for the red galaxy samples corresponding to the specified absolute magnitude M_r bins. The diagonal terms of the error covariance matrices are given in parentheses.

defined by magnitude bin and thresholds, respectively. Tables 9 and 10 present the measurements for the blue and red sub-samples, respectively, analyzed in Section 4. The full error covariance matrices, obtained from the jackknife resampling, are available upon request.

REFERENCES

Abazajian, K., et al. 2005, ApJ, 625, 613
Abazajian, K., et al. 2009, ApJS, 182, 543
Abbas, U., & Sheth, R. K. 2006, MNRAS, 372, 1749
Abbas, U., & Sheth, R. K. 2007, MNRAS, 378, 641
Abbas, U., et al. 2010, MNRAS, 406, 1306
Adelberger, K. L., Steidel, C. C., Pettini, M., Shapley, A. E., Reddy, N. A., & Erb, D. K. 2005, ApJ, 619, 697
Alimi, J.-M., Valls-Gabaud, D., & Blanchard, A. 1988, A&A, 206, L11
Baldry, I. K., Glazebrook, K., Brinkman, J., Ivezić, Ž., Lupton, R. H., Nichol, R. C., & Szalay, A. S. 2004, ApJ, 600, 681
Bamford, S. P., et al. 2009, MNRAS, 393, 1324
Bardeen, J. M., Bond, J. R., Kaiser, N., & Szalay, A. S. 1986, ApJ, 304, 15
Benoist, C., Maurogordato, S., da Costa, L. N., Cappi, A., & Schaeffer, R. 1996, ApJ, 472, 452
Benson, A. J., Cole, S., Frenk, C. S., Baugh, C. M., & Lacey, C. G. 2000, MNRAS, 311, 793
Berlind, A. A., Blanton, M. R., Hogg, D. W., Weinberg, D. H., Davé, R., Eisenstein, D. J., & Katz, N. 2005, ApJ, 629, 625
Berlind, A. A., & Weinberg, D. H. 2002, ApJ, 575, 587
Berlind, A. A., et al. 2003, ApJ, 593, 1
Blake, C., Collister, A., & Lahav, O. 2008, MNRAS, 385, 1257
Blanton, M. R., & Berlind, A. A. 2007, ApJ, 664, 791
Blanton, M. R., Eisenstein, D., Hogg, D. W., Schlegel, D. J., & Brinkmann, J. 2005a, ApJ, 629, 143
Blanton, M. R., Eisenstein, D., Hogg, D. W., & Zehavi, I. 2006, ApJ, 645, 977
Blanton, M. R., Lupton, R. H., Maley, F. M., Young, N., Zehavi, I., & Loveday, J. 2003a, AJ, 125, 2276
Blanton, M. R., & Moustakas, J. 2009, ARA&A, 47, 159
Blanton, M. R., et al. 2003b, AJ, 125, 2348
Blanton, M. R., et al. 2003c, ApJ, 592, 819
Blanton, M. R., et al. 2005b, AJ, 129, 2562
Blumenthal, G. R., Faber, S. M., Primack, J. R., & Rees, M. J. 1984, Nature, 311, 517
Bolton, A. S., Treu, T., Koopmans, L. V. E., Gavazzi, R., Moustakas, L. A., Burles, S., Schlegel, D. J., & Wayth, R. 2008, ApJ, 684, 248
Bower, R. G., Benson, A. J., Malbon, R., Helly, J. C., Frenk, C. S., Baugh, C. M., Cole, S., & Lacey, C. G. 2006, MNRAS, 370, 645
Boylan-Kolchin, M., Springel, V., White, S. D. M., & Jenkins, A. 2010, MNRAS, 406, 896
Brammer, G. B., et al. 2009, ApJ, 706, L173
Brown, M. J. I., Dey, A., Jannuzi, B. T., Lauer, T. R., Tiede, G. P., & Mikkles, V. 2003, ApJ, 597, 225
Brown, M. J. I., Webster, R. L., & Boyle, B. J. 2000, MNRAS, 317, 782

Brown, M. J. I., et al. 2008, ApJ, 682, 937
Budavari, T., et al. 2003, ApJ, 595, 59
Bullock, J. S., Kolatt, T. S., Sigad, Y., Somerville, R. S., Klypin, A. A., Primack, J. R., & Dekel, A. 2001, MNRAS, 321, 559
Bullock, J. S., Wechsler, R. H., & Somerville, R. S. 2002, MNRAS, 329, 246
Cacciato, M., van den Bosch, F. C., More, S., Li, R., Mo, H. J., & Yang, X. 2009, MNRAS, 394, 929
Choi, Y.-Y., Park, C., Kim, J., Gott, J. R., III, Weinberg, D. H., Vogeley, M. S., & Kim, S. S. 2010, ApJS, 190, 181
Choi, Y.-Y., Park, C., & Vogeley, M. S. 2007, ApJ, 658, 884
Coil, A. L., Newman, J. A., Cooper, M. C., Davis, M., Faber, S. M., Koo, D. C., & Willmer, C. N. A. 2006, ApJ, 644, 671
Coil, A. L., et al. 2008, ApJ, 672, 153
Cole, S., Aragon-Salamanca, A., Frenk, C. S., Navarro, J. F., & Zepf, S. E. 1994, MNRAS, 271, 781
Coles, P. 1993, MNRAS, 262, 1065
Colless, M., et al. 2001, MNRAS, 328, 1039
Collister, A. A., & Lahav, O. 2005, MNRAS, 361, 415
Conroy, C., Wechsler, R. H., & Kravtsov, A. V. 2006, ApJ, 647, 201
Cooray, A. 2005, MNRAS, 363, 337
Cooray, A. 2006, MNRAS, 365, 842
Cooray, A., & Sheth, R. 2002, Phys. Rep., 372, 1
Cresswell, J. G., & Percival, W. J. 2009, MNRAS, 392, 682
Croton, D. J., Gao, L., & White, S. D. M. 2007, MNRAS, 374, 1303
Croton, D. J., et al. 2006, MNRAS, 365, 11
Daddi, E., et al. 2003, ApJ, 588, 50
Dalal, N., White, M., Richard, B. J., & Shirokov, A. 2008, ApJ, 687, 12
Davis, M., & Geller, M. J. 1976, ApJ, 208, 13
Davis, M., Huchra, J., Latham, D. W., & Tonry, J. 1982, ApJ, 253, 423
Davis, M., Meiksin, A., Strauss, M. A., da Costa, L. N., & Yahil, A. 1988, ApJ, 333, L9
Davis, M., & Peebles, P. J. E. 1983, ApJ, 267, 465
Dunkley, J., et al. 2009, ApJS, 180, 306
Eisenstein, D. J., et al. 2001, AJ, 122, 2267
Eisenstein, D. J., et al. 2005, ApJ, 633, 560
Eisenstein, D. J., et al. 2011, AJ, submitted (arXiv:1101.1519)
Fischer, P., et al. 2000, AJ, 120, 1198
Fisher, K. B., Davis, M., Strauss, M. A., Yahil, A., & Huchra, J. P. 1994, MNRAS, 266, 50
Font, A. S., et al. 2008, MNRAS, 389, 1619
Fry, J. N., & Gaztañaga, E. 1993, ApJ, 413, 447
Fukugita, M., Ichikawa, T., Gunn, J. E., Doi, M., Shimasaku, K., & Schneider, D. P. 1996, AJ, 111, 1748
Gao, L., Springel, V., & White, S. D. M. 2005, MNRAS, 363, L66
Geller, M. J., & Huchra, J. P. 1989, Science, 246, 897
Gerhard, O., Kronawitter, A., Saglia, R. P., & Bender, R. 2001, AJ, 121, 1936
Gerke, B., et al. 2007, MNRAS, 376, 1425
Giovanelli, R., Haynes, M. P., & Chincarini, G. L. 1986, ApJ, 300, 77
Gott, J. R., III, Juric, M., Schlegel, D. J., Hoyle, F., Vogeley, M. S., Tegmark, M., Bahcall, N. A., & Brinkmann, J. 2005, ApJ, 624, 463
Gott, J. R., III, & Turner, E. L. 1979, ApJ, 232, L79
Gregory, S. A., & Thompson, L. A. 1978, ApJ, 222, 784
Gunn, J. E., et al. 1998, AJ, 116, 3040
Gunn, J. E., et al. 2006, AJ, 131, 2332
Guo, Q., White, S., Li, C., & Boylan-Kolchin, M. 2010, MNRAS, 404, 1111
Guzzo, L., Strauss, M. A., Fisher, K. B., Giovanelli, R., & Haynes, M. P. 1997, ApJ, 489, 37
Hamana, T., Yamada, T., Ouchi, M., Iwata, I., & Kodama, T. 2006, MNRAS, 369, 1929
Hamilton, A. J. S. 1988, ApJ, 331, L59
Hamilton, A. J. S. 1993, ApJ, 417, 19
Hamilton, A. J. S. 1998, in The Evolving Universe, ed. D. Hamilton (Astrophysics and Space Science Library, Vol. 231; Dordrecht: Kluwer), 185
Hansen, S. M., Sheldon, E. S., Wechsler, R. H., & Koester, B. P. 2009, ApJ, 699, 1333
Harker, G., Cole, S., Helly, J., Frenk, C., & Jenkins, A. 2006, MNRAS, 367, 1039
Hinshaw, G., et al. 2009, ApJS, 180, 225
Hogg, D. W., Schlegel, D. J., Finkbeiner, D. P., & Gunn, J. E. 2001, AJ, 122, 2129
Hogg, D. W., et al. 2003, ApJ, 585, L5
Hogg, D. W., et al. 2004, ApJ, 601, L29
Hubble, E. P. 1936, The Realm of the Nebulae (Oxford: Oxford Univ. Press)
Ivezić, Ž., et al. 2004, Astron. Nachr., 325, 583
Jing, Y. P. 1998, ApJ, 503, L9
Jing, Y. P., & Börner, G. 1998, ApJ, 503, 37
Jing, Y. P., Börner, G., & Suto, Y. 2002, ApJ, 564, 15

Jing, Y. P., Mo, H. J., & Börner, G. 1998, ApJ, 494, 1
Jing, Y. P., Suto, Y., & Mo, H. J. 2007, ApJ, 657, 664
Kaiser, N. 1984, ApJ, 294, L9
Kaiser, N. 1987, MNRAS, 227, 1
Kang, X., Jing, Y. P., Mo, H. J., & Börner, G. 2005, ApJ, 631, 21
Kang, X., & van den Bosch, F. C. 2008, ApJ, 676, L101
Kauffmann, G., Colberg, J. M., Diaferio, A., & White, S. D. M. 1999, MNRAS, 303, 188
Kauffmann, G., Nusser, A., & Steinmetz, M. 1997, MNRAS, 286, 795
Kauffmann, G., White, S. D. M., & Guiderdoni, B. 1993, MNRAS, 264, 201
Kazin, E. A., et al. 2010, ApJ, 710, 1444
Kessler, R., et al. 2009, ApJS, 185, 32
Kim, H. S., Baugh, C. M., Cole, S., Frenk, C. S., & Benson, A. J. 2009, MNRAS, 400, 1527
Kim, J., Park, C., & Choi, Y. 2008, ApJ, 683, 123
Kirshner, R. P., Oemler, A., Jr., Schechter, P. L., & Shectman, S. A. 1981, ApJ, 248, L57
Komatsu, E., et al. 2009, ApJS, 180, 330
Kowalski, M., et al. 2008, ApJ, 686, 749
Kravtsov, A. V., Berlind, A. A., Wechsler, R. H., Klypin, A. A., Gottloeber, S., Allgood, B., & Primack, J. R. 2004, ApJ, 609, 35
Landy, S. D., & Szalay, A. S. 1993, ApJ, 412, 64
Lee, K., Giavalisco, M., Conroy, C., Wechsler, R. H., Ferguson, H., Somerville, R., Dickinson, M. E., & Urry, C. M. 2008, ApJ, 695, 368
Lee, K., Giavalisco, M., Gnedin, O. Y., Somerville, R., Ferguson, H., Dickinson, M., & Ouchi, M. 2006, ApJ, 642, 63
Li, C., Kauffmann, G., Jing, Y. P., White, S. D. M., Boerner, G., & Cheng, F. Z. 2006, MNRAS, 368, 21
Li, C., & White, S. D. M. 2009, MNRAS, 398, 2177
Li, C., & White, S. D. M. 2010, MNRAS, 407, 515
Loh, Y.-S., et al. 2010, MNRAS, 407, 55
Loveday, J., Maddox, S. J., Efstathiou, G., & Peterson, B. A. 1995, ApJ, 442, 457
Lupton, R. H., Gunn, J. E., Ivezić, Ž., Knapp, G. R., Kent, S., & Yasuda, N. 2001, in ASP Conf. Ser. 238, Astronomical Data Analysis Software and Systems X, ed. F. R. Harnden, Jr., F. A. Primini, & H. E. Payne (San Francisco, CA: ASP), 269
Lupton, R. H., Gunn, J. E., & Szalay, A. S. 1999, AJ, 118, 1406
Ma, C., & Fry, J. N. 2000, ApJ, 543, 503
Madgwick, D. S., et al. 2003, MNRAS, 344, 847
Magliocchetti, M., & Porciani, C. 2003, MNRAS, 346, 186
Mandelbaum, R., Seljak, U., Kauffmann, G., Hirata, C. M., & Brinkmann, J. 2006, MNRAS, 368, 715
Mann, R. G., Peacock, J. A., & Heavens, A. F. 1998, MNRAS, 293, 209
Martin, D. C., et al. 2007, ApJS, 173, 342
Masjedi, M., et al. 2006, ApJ, 644, 54
McBride, C. K., Connolly, A. J., Gardner, J. P., Scranton, R., Newman, J. A., Scoccimarro, R., Zehavi, I., & Schneider, D. P. 2011, ApJ, 726, 13
Meneux, B., et al. 2008, A&A, 478, 299
Meneux, B., et al. 2009, A&A, 505, 463
Mo, H. J., & White, S. D. M. 1996, MNRAS, 282, 1096
More, S., van den Bosch, F. C., Cacciato, M., Mo, H. J., Yang, X., & Li, R. 2009, MNRAS, 392, 801
Moster, B. P., Somerville, R. S., Maulbetsch, C., van den Bosch, F. C., Macciò, A. V., Naab, T., & Oser, L. 2010, ApJ, 710, 903
Moustakas, L. A., & Somerville, R. S. 2002, ApJ, 577, 1
Narayanan, V. K., Berlind, A. A., & Weinberg, D. H. 2000, ApJ, 528, 1
Navarro, J. F., Frenk, C. S., & White, S. D. M. 1996, ApJ, 462, 563
Norberg, P., Baugh, C. M., Gaztanaga, E., & Croton, D. J. 2009, MNRAS, 396, 19
Norberg, P., Gaztanaga, E., Baugh, C. M., & Croton, D. J. 2011, MNRAS, submitted (arXiv:1106.5701)
Norberg, P., et al. 2001, MNRAS, 328, 64
Norberg, P., et al. 2002, MNRAS, 332, 827
Ouchi, M., et al. 2005, ApJ, 635, L117
Padmanabhan, N., et al. 2008, ApJ, 674, 1217
Peacock, J. A., & Smith, R. E. 2000, MNRAS, 318, 1144
Pearce, F. R., Jenkins, A., Frenk, C. S., White, S. D. M., Thomas, P. A., Couchman, H. M. P., Peacock, J. A., & Efstathiou, G. 2001, MNRAS, 326, 649
Peebles, P. J. E. 1974, A&A, 32, 197
Peebles, P. J. E. 1980, The Large-Scale Structure of the Universe (Princeton, NJ: Princeton Univ. Press)
Peebles, P. J. E. 1982, ApJ, 263, L1
Percival, W. J., et al. 2010, MNRAS, 401, 2148
Persic, M., Salucci, P., & Stel, F. 1996, MNRAS, 281, 27
Phleps, S., Peacock, J. A., Meisenheimer, K., & Wolf, C. 2006, A&A, 457, 145

Pier, J. R., Munn, J. A., Hindsley, R. B., Hennessy, G. S., Kent, S. M., Lupton, R. H., & Ivezić, Ž. 2003, AJ, 125, 1559
Pons-Borderia, M., Martinez, V., Stoyan, D., Stoyan, H., & Saar, A. 1999, ApJ, 523, 480
Prada, F., et al. 2003, ApJ, 598, 260
Quadri, R. F., Williams, R. J., Lee, K., Franx, M., van Dokkum, P., & Brammer, G. B. 2008, ApJ, 685, L1
Reid, B. A., et al. 2010, MNRAS, 404, 60
Richards, G. T., et al. 2002, AJ, 123, 2945
Ross, A. J., & Brunner, R. J. 2009, MNRAS, 399, 878
Ross, A. J., & Percival, W. J., & Brunner, R. J. 2010, MNRAS, 407, 420
Rozo, E., et al. 2010, ApJ, 708, 645
Rubin, V. C., Thonnard, N., & Ford, W. K., Jr. 1978, ApJ, 225, L107
Sargent, W. L. W., & Turner, E. L. 1977, ApJ, 212, L3
Schechter, P. 1976, ApJ, 203, 297
Scherrer, R. J., & Weinberg, D. H. 1998, ApJ, 504, 607
Scoccimarro, R., & Sheth, R. K. 2002, MNRAS, 329, 629
Scoccimarro, R., Sheth, R. K., Hui, L., & Jain, B. 2001, ApJ, 546, 20
Scott, D., Srednicki, M., & White, M. 1994, ApJ, 421, L5
Scranton, R. 2002, MNRAS, 332, 697
Seljak, U. 2000, MNRAS, 318, 203
Shectman, S. A., Landy, S. D., Oemler, A., Tucker, D. L., Lin, H., Kirshner, R. P., & Schechter, P. L. 1996, ApJ, 470, 172
Sheth, R. K., Mo, H. J., & Tormen, G. 2001, MNRAS, 323, 1
Sheth, R. K., & Tormen, G. 2004, MNRAS, 350, 1385
Simha, V., Weinberg, D. H., Davé, R., Gnedin, O. Y., Katz, N., & Kereš, D. 2009, MNRAS, 399, 650
Simon, P., Hetterscheidt, M., Wolf, C., Meisenheimer, K., Hildebrandt, H., Schneider, P., Schirmer, M., & Erben, T. 2009, MNRAS, 398, 807
Skibba, R. A. 2009, MNRAS, 392, 1467
Skibba, R. A., & Sheth, R. K. 2009, MNRAS, 392, 1080
Skibba, R., Sheth, R. K., Connolly, A. J., & Scranton, R. 2006, MNRAS, 369, 68
Skibba, R. A., et al. 2009, MNRAS, 399, 966
Smith, J. A., et al. 2002, AJ, 123, 2121
Smith, R. E., et al. 2003, MNRAS, 341, 1311
Stoughton, C., et al. 2002, AJ, 123, 485
Strateva, I., et al. 2001, AJ, 122, 1861
Strauss, M. A., & Willick, J. A. 1995, Phys. Rep., 261, 271
Strauss, M. A., et al. 2002, AJ, 124, 1810
Swanson, M. E. C., Tegmark, M., Blanton, M., & Zehavi, I. 2008, MNRAS, 385, 1635
Szapudi, I., & Szalay, A. S. 1998, ApJ, 494, L41
Tegmark, M., et al. 2004, ApJ, 606, 702
Tinker, J. L., Conroy, C., Norberg, P., Patiri, S. G., Weinberg, D. H., & Warren, M. S. 2008, ApJ, 686, 53
Tinker, J. L., Robertson, B. E., Kravtsov, A. V., Klypin, A., Warren, M. S., Yepes, G., & Gottlober, S. 2010, ApJ, 724, 878
Tinker, J. L., Weinberg, D. H., Zheng, Z., & Zehavi, I. 2005, ApJ, 631, 41
Totsuji, H., & Kihara, T. 1969, PASJ, 21, 221
Tucker, D., et al. 2006, Astron. Nachr., 327, 821
Vale, A., & Ostriker, J. P. 2006, MNRAS, 371, 1173
Valls-Gabaud, D., Alimi, J.-M., & Blanchard, A. 1989, Nature, 341, 215
van den Bosch, F. C., Aquino, D., Yang, X., Mo, H. J., Pasquali, A., McIntosh, D. H., Weinmann, S. M., & Kang, X. 2008a, MNRAS, 387, 79
van den Bosch, F. C., Mo, H. J., & Yang, X. H. 2003a, MNRAS, 345, 923
van den Bosch, F. C., Pasquali, A., Yang, X., Mo, H. J., Weinmann, S., McIntosh, D. H., & Aquino, D. 2008b, MNRAS, submitted (arXiv:0805.0002)
van den Bosch, F. C., Yang, X. H., & Mo, H. J. 2003b, MNRAS, 340, 771

van den Bosch, F. C., et al. 2007, MNRAS, 376, 841
Verheijen, M. A. W. 2001, ApJ, 563, 694
Wake, D. A., et al. 2008, MNRAS, 387, 1045
Wang, Y., Yang, X., Mo, H. J., & van den Bosch, F. C. 2007, ApJ, 664, 608
Wang, Y., Yang, X., Mo, H. J., van den Bosch, F. C., Katz, N., Pasquali, A., McIntosh, D. H., & Weinmann, S. M. 2009, ApJ, 697, 247
Watson, D. F., Berlind, A. A., McBride, C. K., & Masjedi, M. 2010, ApJ, 709, 115
Watson, D. F., Berlind, A. A., & Zentner, A. R. 2011, ApJ, submitted (arXiv:1101.5155)
Wechsler, R. H. 2004, in Carnegie Observatories Astrophysics Series, Vol. 3: Clusters of Galaxies: Probes of Cosmological Structure and Galaxy Evolution, ed. J. S. Mulchaey, A. Dressler, & A. Oemler (Pasadena, CA: Carnegie Observatories)
Wechsler, R. H., Zentner, A. R., Bullock, J. S., Kravtsov, A. V., & Allgood, B. 2006, ApJ, 647, 201
Weinberg, D. H., Davé, R., Katz, N., & Hernquist, L. 2004, ApJ, 601, 1
Weinmann, S. M., van den Bosch, F. C., Yang, X., & Mo, H. J. 2006, MNRAS, 366, 2
Wetzel, A. R., Cohn, J. D., White, M., Holz, D. E., & Warren, M. S. 2007, ApJ, 656, 139
White, M., Zheng, Z., Brown, M. J. I., Dey, A., & Jannuzi, B. T. 2007, ApJ, 655, L69
White, S. D. M., & Frenk, C. S. 1991, ApJ, 379, 52
Willmer, C. N. A., da Costa, L. N., & Pellegrini, P. S. 1998, AJ, 115, 869
Wyder, T. K., et al. 2007, ApJS, 173, 293
Yan, R., Madgwick, D. S., & White, M. 2003, ApJ, 598, 848
Yang, X. H., Mo, H. J., Jing, Y. P., & van den Bosch, F. C. 2005a, MNRAS, 358, 217
Yang, X. H., Mo, H. J., & van den Bosch, F. C. 2003, MNRAS, 339, 1057
Yang, X. H., Mo, H. J., & van den Bosch, F. C. 2008, ApJ, 676, 248
Yang, X. H., Mo, H. J., van den Bosch, F. C., & Jing, Y. P. 2005b, MNRAS, 356, 1293
Yang, X. H., Mo, H. J., van den Bosch, F. C., Pasquali, A., Li, C., & Barden, M. 2007, ApJ, 671, 153
Yoo, J., Tinker, J. L., Weinberg, D. H., Zheng, Z., Katz, N., & Davé, R. 2006, ApJ, 652, 26
Yoo, J., Weinberg, D. H., Tinker, J. L., Zheng, Z., & Warren, M. S. 2009, ApJ, 698, 967
York, D. G., et al. 2000, AJ, 120, 1579
Zaritsky, D., & White, S. D. M. 1994, ApJ, 435, 599
Zehavi, I., et al. 2002, ApJ, 571, 172
Zehavi, I., et al. 2004, ApJ, 608, 16
Zehavi, I., et al. 2005a, ApJ, 621, 22
Zehavi, I., et al. 2005b, ApJ, 630, 1 (Z05)
Zentner, A. R., Berlind, A. A., Bullock, J. S., Kravtsov, A. V., & Wechsler, R. H. 2005, ApJ, 624, 505
Zheng, Z. 2004, ApJ, 610, 61
Zheng, Z., Coil, A. L., & Zehavi, I. 2007, ApJ, 667, 760
Zheng, Z., & Weinberg, D. H. 2007, ApJ, 659, 1
Zheng, Z., Zehavi, I., Eisenstein, D. J., Weinberg, D. H., & Jing, Y. 2009, ApJ, 707, 554
Zheng, Z., et al. 2005, ApJ, 633, 791
Zhu, G., Zheng, Z., Lin, W. P., Jing, Y. P., Kang, X., & Gao, L. 2006, ApJ, 639, L5
Zu, Y., Zheng, Z., Zhu, G., & Jing, Y. P. 2008, ApJ, 686, 41
Zwicky, F. 1933, Helv. Phys. Acta, 6, 110
Zwicky, F. 1937, ApJ, 86, 217